Engineering exciton-polaritons at room temperature with halide perovskite based metasurface

Nguyen Ha My Dang

N° d'ordre NNT : **2022ECDL0002**

THESE de DOCTORAT DE L'UNIVERSITE DE LYON
opérée au sein de l'Ecole centrale de Lyon

Ecole Doctorale ED 160
Electronique, Electrotechnique, Automatique

Spécialité de doctorat :
Electronique, micro et nano-électronique, optique et laser

Soutenue publiquement le 12/09/2022, par :
Nguyen Ha My DANG

Engineering exciton-polaritons at room temperature with halide perovskite based metasurface

---

Devant le jury composé de :

GAUTHIER-LAFAYE, Olivier	Directeur de recherche	LAAS	Rapporteur
GUILLET, Thierry	Professeur des Universités	L2C	Rapporteur
DIEDERICHS, Carole	Maître de Conférences	UPMC	Examinatrice
GERACE, Dario	Professeur	UNIPV	Examinateur
DELEPORTE, Emmanuelle	Professeure	LuMIn	Invitée
SEASSAL, Christian	Directeur de recherche	INL	Directeur de thèse
NGUYEN, Hai Son	Maître de Conférences	INL	Co-encadrant

Acknowledgement

My PhD journey has come to an end. As I look back, I would like to take this moment to express my gratitude to everyone who supported me along the way.

I would like to acknowledge and give my sincere thanks to my supervisors Hai Son Nguyen and Christian Seassal. Their guidance and advice carried me through all the stages of this thesis. Christian is thoughtful, well-organized, and a caring, attentive supervisor who is always available to help, despite his busy schedule. His expertise, constructive feedback, and insightful comments have been invaluable. Hai Son has always been kind, patient, and encouraging. His unlimited ideas contributed remarkably to shaping the direction of my thesis. His passion and curiosity in science have inspired me and driven my motivation to pursue this doctoral research. Working with Christian and Hai Son was truly an amazing experience.

I was fortunate to work at INL, which provided the necessary resources and a conducive environment for my research. I would like to express my gratitude to Radek, Thomas, Pierre, Céline, Aziz, Philippe, José, and all the Nanolyon staff for their support and advice. Their insights and experience have helped me a lot to carry out my experiments throughout my PhD.

I would like to acknowledge our collaborators Emmanuelle Deleporte and Gaëlle Trippé-Allard from the LuMIn laboratory, as well as Dario Gerace and Simone Zanotti from the University of Pavia. Their cooperation and willingness to contribute to my research have been essential to this project.

To my colleagues and friends at INL, thank you for creating such a supportive and stimulating environment. Your camaraderie, discussions, and encouragement have been crucial during challenging times.

Finally, to my family and my partner, thank you for your endless patience, understanding, and encouragement. Your unconditional love and support has carried me through the ups and downs of this thesis journey.

Thank you all for your support and encouragement.

TABLE OF CONTENTS

ABBREVIATIONS

AFM	Atomic Force Microscope
ARPL	Angle-Resolved Photoluminescence
ARR	Angle-Resolved Reflectivity
BEC	Bose-Einstein Condensation
BIC	Bound states In the Continuum
DBR	Distributed Bragg Reflector
DFB	Distributed Feedback Resonator
DMF	Dimethylformamide
E-beam lithography	Electron Beam Lithography
FB	Fabry-Pérot cavity
FF	Filling Factor
GM	Guided Modes
GME	Guided Mode Expansion
GR	Guided Resonances
HOP	Hybrid Organic-Inorganic Perovskite
LIL	Laser Interference Lithography
LP	Lower Polariton
PC	Photonic Crystal
PEPI	Bi-(Phenethyl Ammonium) Tetraiodoplumbate
PL	Photoluminescence
PMMA	Poly(Methyl Methacrylate)
pol-BIC	Polariton Bound states In the Continuum
Q-factor	Quality Factor
RCWA	Rigorous Coupled Wave Analysis

RIE	Reactive Ion Etching
SEM	Scanning Electron Microscope
TMD	Transition Metal Dichalcogenide
UP	Upper Polariton
XRD	X-ray Diffraction

INTRODUCTION

Numerical devices (phones, computers) have become an indispensable part of our daily lives. In the past years, the need of signal processing devices have accelerated sharply along with the explosion of innovations in digital technology such as the internet, artificial intelligence and machine learning, blockchain, cyber security, etc. This leads to the soar in energy consumption and rises impacts on the environment. To address these issues, our civilization now seeks for its next technological revolution with breakthroughs in performance enhancement, size reduction and energy consumption of numerical devices. However, the delivered technology – micro-electronic based on silicon technology – the core of production, is facing challenges to enter this revolution. This is due to the acceleration in complexity of device and the fact that the evolution of semiconductor technology is reaching molecular limits.

In this context, photonic devices, using photons as information carriers instead of electrons, have appeared as a solution to solve the high speed and low consumption dilemma of electronic counterparts. Indeed, the world nowadays is connected via internet network made of optical signals circulating in fiber optic cables under the sea. Nevertheless, the interaction between photons, i.e. photonic nonlinearity, is negligible in comparison with the Coulomb interaction between electrons, leading to the limitation of photonic devices in information processing. As a matter of fact, numerical devices still rely on electronic components (transistors, gates, and switches) to process information. This requires conversion back and forth between optical signal and electronic signal at the optical fiber-router interface, leading to data losses and energy consumption.

Recently, exciton-polaritons have emerged as a promising platform combining the strength of both photonic and electronic systems for future numerical devices. They are hybrid half-matter, half-light quasi-particles resulting from the strong coupling regime between

electronic excitations in semiconductors, i.e. excitons, and confined photons in optical cavities. Thanks to their hybrid nature, these quasiparticles exhibit low losses, high speed propagation across long distance through the photonic half, and at the same time a strong nonlinearity inherited from the excitonic half. Although many polaritonic devices such as polaritonic memories, transistors, gates and diodes have been experimentally demonstrated by different groups, these devices are still at the stage of laboratory research. Indeed, this fascinating platform has two major drawbacks: i) most of its development has been done with GaAs-based semiconductors that requires operation at cryogenic temperature for excitons, as well as costly growth method, ii) the main optical confinement scheme is with thick vertical cavity having many layers, and not compatible with mature CMOS technology developed for micro-electronics.

In this thesis, we tackle the two main drawbacks of conventional polaritonic devices by proposing a new polarionic platform that we call excitonic metasurface. This consists of nanopatterning a semiconductor thin film into sub-wavelength resonant metasurface. On the material side, hybrid perovskite has been chosen thanks to its excellent excitonic features at room temperature and low-cost fabrication. On the photonic side, by exploiting the physics of periodic metasurface, it is possible to tailor novel properties for photonic modes such as on-demand photonic group velocity and losses engineering, thus leading to new functionalities for polaritonic devices once the strong coupling regime of these photons with perovskite excitons is established. The outline of this manuscript is as below:

- Chapter 1 first introduces the general concepts of excitons in semiconductors and the strong coupling regime between excitons with confined photons to form exciton-polariton quasiparticles. In the second part of the chapter, we discuss on the emergence of halide perovskite as room temperature excitonic material for studying the strong coupling physics. We then present the essential concepts of photonic Bloch resonances

in subwavelength lattice such as bandgap engineering and Bound state In the Continuum (BIC). Lastly, we introduce the excitonic metasurface approach to explore exciton-polaritons in patterned perovskite layer.

- In chapter 2, we present different fabrication processes for perovskite thin film deposition and the structuration of perovskite layer into metasurface. In particular, two methods of perovskite structuration are developed: infiltration of perovskite solution into a prepatterned substrate, and direct patterning of a perovskite layer using thermal nanoimprint. To quantify and evaluate the fabricated structures, the results of different characterizations including morphology/crystallization quality (SEM, XRD), optical properties (photoluminescence, absorption), and stability (lifetime performance) are discussed in details.
- Chapter 3 reports on the engineering of polariton band structure at room temperature using perovskite metasurface. Employing the concept of Bloch resonances in photonic crystal slab, we predict and demonstrate experimentally an on-demand tailoring of polariton energy-momentum band structure (i.e. the real part of polariton dispersion); exhibiting distinct features such as slow-light, linear, multivalley shapes which could be very useful for different types of polartionic functionalities.
- In chapter 4, we discuss the engineering of polariton losses (i.e. the imaginary part of polariton dispersion) in perovskite metasurface. The formation of polartion BIC at room temperature, resulting from the strong coupling regime between perovskite excitons and photonic BIC, is experimentally demonstrated. In particular, we show that the polariton BIC exhibits an infinite radiative lifetime, leading to an enhancement of the total quality factor. Moreover, this peculiar polaritonic state inherits fully the topological nature of a photonic BIC and exhibits a polarization vortex pattern in the farfield emission

- In chapter 5, we focus on the study of polariton propagation in a large homogeneous perovskite metasurface which was achieved by using thermal imprinting technique. The polariton propagation is studied in both real-space and momentum space, showing ballistic propagation over 100 μm with no backscattering signals. Remarkably, this ballistic propagation corresponds to polaritons with a high excitonic fraction of 75%.

CHAPTER 1

INTRODUCTION OF EXCITON POLARITONS IN HALIDE PEROVSKITE

1.1 Excitons in semiconductors

An exciton in semiconductor is a quasiparticle made of a pair of an electron (in the conduction band) and a hole (in the valance band) bounded together by the electrostatic Coulomb force. Excitons are fundamental excitations in semiconductors, generated after a photon absorption as an electron transferred from the valance band (HOMO) to the conduction band (LUMO) leaving behind a hole in the HOMO band. They can be described as hydrogen-like states having discrete resonance energies in the semiconductor bandgap. These resonances are characterized by the binding energy (E_b) representing the attractive Coulomb interaction between the electron-hole pair. Excitons are only stable if the binding energy is larger than the thermal perturbation energy k_BT where k_B is the Boltzmann constant and T is the temperature. As consequence, room temperature excitonic material requires E_b >25 meV. Moreover, depending on the delocalization of the bounded electron-hole pairs, there are two excitonic models: free excitons called Wannier-Mott excitons and tightly bound excitons also known as Frenkel excitons.

Wannier-Mott excitons are mainly observed in inorganic semiconductors which possess relatively large dielectric constant resulting in the screening effect of the electric field in order to reduce the Coulomb interaction between electrons and holes. The formation of Wannier-Mott excitons is illustrated in figure 1.1a. This type of excitons exhibit a relatively large Bohr radius (a_B) that encompasses many atoms. For example, the Bohr radius of Wannier-Mott excitons are in the range of a few nanometers: a_B = 10 nm in GaAs, a_B = 7 nm in CdTe, a_B = 3

nm in GaN, a_B = 1 nm in ZnO, respectively. Hence, Wannier-Mott excitons are delocalized states which can transfer freely throughout the crystal. The delocalization of excitons enhances the exciton-exciton interactions, leading to high nonlinear behaviors. However, due to this delocalization, the binding energy of Wannier-Motts excitons is relatively small (on the order of tens of meV) [1]. As a consequence, most of traditional inorganics excitons (GaAs, InAs, CdTe…) are not stable at room temperature, except the smallest ones (GaN, ZnO).

Frenkel excitons are generally observed in organic semiconductors. They possess much smaller Bohr radius which is around the size of the lattice constant (about 0.5 nm). This feature makes Frenkel excitons localized states and tightly bound to specific atoms or molecules (as illustrated in Figure 1.1b). Therefore they exhibit huge binding energy, having the order of magnitude of hundreds of meV [2]. Thus most of organic excitons are very stable at room temperature.

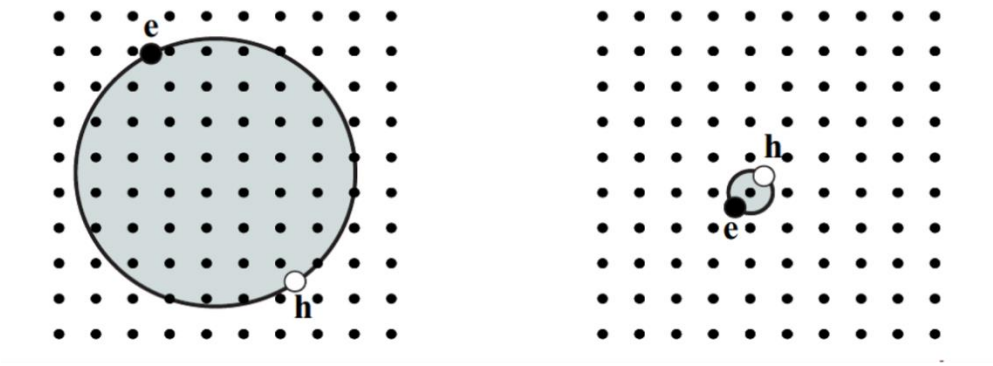

Figure 1.1 Illustration of the Wannier-Mott excitons and Frenkel excitons [1]

1.2 Light-matter interaction mechanisms

Light-matter interaction for excitonic resonances consists of two main mechanisms: i) photon emission following the radiative recombination of an electron-hole pair, ii) photon absorption leading to the creation of an electron-hole pair. Both mechanisms take place

resonantly at the energy of the excitonic transition and is characterized by the probability for the excitonic transition to occur. This probability is called oscillator strength (*f*), representing the radiative coupling between the excitons and its electromagnetic environment. Intuitively, such a dimensionless quantity relates directly to the strength of the exciton-photon interaction and the efficiency of light-matter interaction mechanisms (see eq.1.5 of the next section).

On the other hand, in a semiclassical approach, the excitonic resonance can be described by a Lorentz oscillator model. This approach allows to calculate classically the propagation, transmission, reflection and absorption of lightwaves in an excitonic materials with the use of Maxwell equations, using the following dielectric function:

$$\varepsilon(E) = n^2 + \frac{A_X}{E_X^2 - E^2 - i\gamma_X E} \qquad \text{(eq.1.1)}$$

Here n is the refractive index of the material without excitonic resonance, called background refractive index, E_X is the exciton energy, γ_X being its linewidth and the amplitude A_X is given by the oscillator strength per volume:

$$\frac{f}{V} = \frac{\varepsilon_0 m_0}{\hbar^2} A_X \qquad \text{(eq.1.2)}$$

where ε_0 is the vacuum electric permittivity constant and m_0 the electron mass.

1.3 Exciton polarions

1.3.1 The strong coupling regime

As discussed in the previous section, the electron-hole pair once excited may recombine radiatively and emits a photon of the same energy of the exciton. Without any confinement scheme, this photon escapes out of the semiconductor and radiates to the free space (i.e. the radiative continuum). However, if the emitted photon is confined in the vicinity of the excitonic material, it can be re-absorbed to create a new exciton, then re-emitted, then re-absorbed … until it leaks out of the confinement system or is lost due to a non-radiative process. In such a

scenario, the coupling between excitons and photons is strong enough to overcome the losses and leads to many re-emission/re-absorption cycles. The eigenmodes of the system are no more excitons or photons but hybrid exciton-photon quasiparticles called exciton polaritons.

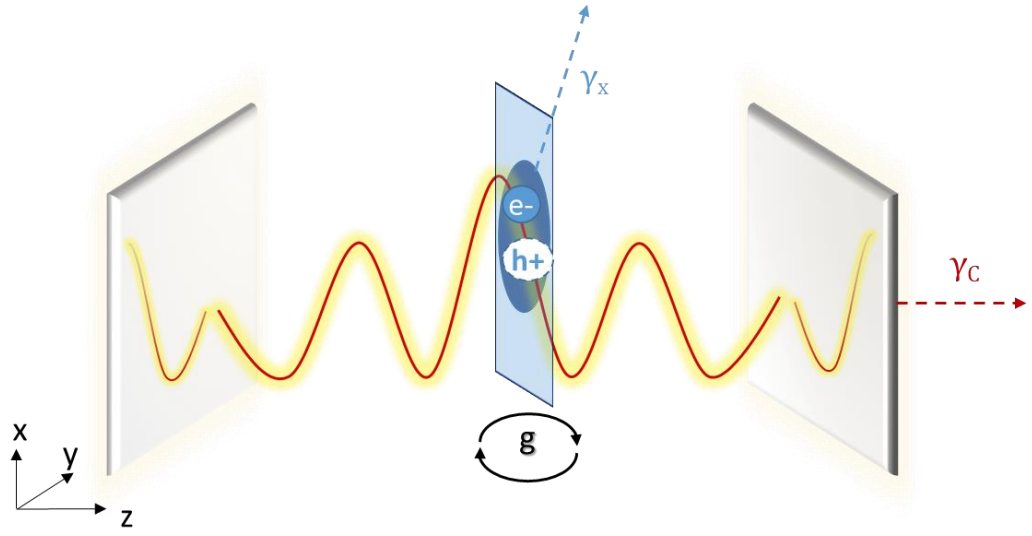

Figure 1.2. Illustration of light matter interaction between photons confined in a cavity and excitons of a semiconductor quantum well. Here g is the light-matter coupling strength, γ_x is the decay rate of exciton and γ_C is the loss rate of photons leaking from the cavity.

These quasi-particles were formed when the coupling strength of the photon-exciton interaction overcomes the dissipation rate in the system (see Figure 1.2). The formation of exciton-polaritons can be described by a two-level system of two coupled oscillators. One oscillator corresponds to the pure photonic state $|C\rangle$ and the other one corresponds to the pure excitonic state $|X\rangle$:

$$|C\rangle = \begin{pmatrix} 1 \\ 0 \end{pmatrix}, \qquad |X\rangle = \begin{pmatrix} 0 \\ 1 \end{pmatrix} \qquad \text{(eq. 1.3)}$$

The Hamiltonian of the hybridized system, taking into account the energy difference between excitons and photons, the coupling between them, and the losses coming from both components, can be written as:

$$H = \begin{pmatrix} E_C + i\gamma_C & g \\ g & E_X + i\gamma_X \end{pmatrix} \quad \text{(eq. 1.4)}$$

where E_C and E_X are photon and exciton energy, respectively. γ_C and γ_X are losses rates due to the leaking of photons from an imperfect confinement, and the decay of excitons, respectively. Most importantly g is the coupling strength between the photon and the exciton. This coupling strength is directly related to the oscillator strength f and the confinement volume V_C of photons, and is given by:

$$g \propto \sqrt{\frac{f}{V_c}} \quad \text{(eq. 1.5)}$$

The corresponding energy eigenvalues of the system are:

$$E_{UP,LP} = \frac{E_C+E_X+i(\gamma_C+\gamma_X)}{2} \pm \sqrt{g^2 + \left[\frac{(E_C-E_X)+i(\gamma_C-\gamma_X)}{2}\right]^2} \quad \text{(eq. 1.6)}$$

From the eigenvalue equation, the condition to operate in strong coupling regime is:

$$g \geq \frac{|\gamma_C-\gamma_X|}{2} \quad \text{(eq. 1.7)}$$

If this condition is not satisfied, the system operates in the weak coupling regime and the eigenstates of the system are simply the pure photonic state and excitonic state.

Remarkably, when the coupling strength g follows the condition $g \geq \frac{|\gamma_C-\gamma_X|}{2}$, the confined photons and excitons interact in the strong coupling regime. The eigenstates of the system are no more the uncoupled states but two hybrid ones, noted as the upper polariton $|UP\rangle$ and the lower polariton $|LP\rangle$. These new eigenstates of the system correspond to the coherent superpositions of excitons and photons.

The energy-momentum or energy-wavevector relationship (i.e. dispersion) of the upper/lower polariton are called upper and lower polariton branches. Importantly, at the wavevector corresponding to the crossing between the uncoupled modes (E_X=E_C), the lower

polaritonic branch and the upper polaritonic branch separate by a splitting energy, defined as the vacuum Rabi splitting $\hbar\Omega$ (see Figure 1.3), given by:

$$\hbar\Omega = \sqrt{4g^2 - (\gamma_C - \gamma_X)^2} \qquad \text{(eq. 1.8)}$$

This anti-crossing effect is the hallmark of the strong coupling regime and is commonly used to distinguish the strong coupling regime from the weak coupling one. However, for some specific experimental conditions, only the lower polariton branch can be measured. In these cases, another criterion may be employed to evidence the strong coupling regime: the lower polariton dispersion in bent when getting closer to the excitonic resonance (see Figure 1.4 [3]).

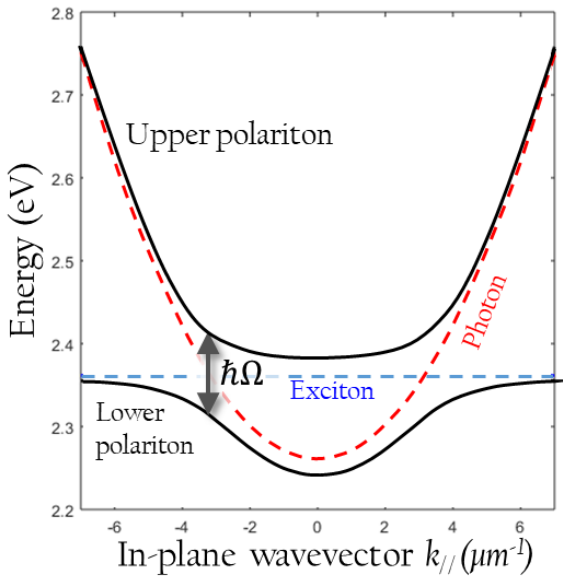

Figure 1.3. A text-book example of exciton-polaritons: strong coupling between excitons of a quantum well embedded at an antinode of a vertical microcavity. The red dashed line presents the dispersion of the photonic mode of the cavity. The blue dashed line shows the dispersion of the excitonic resonance of the quantum well which is almost flat in the range of the optical wavevector. Solid black lines are the dispersion of the upper polariton and lower polariton.

1.3.2 Hybrid nature of exciton-polaritons

The lower and upper polariton are partially photon and partially exciton quasi-particles, and their eigenvectors can be written as:

$$\begin{cases} |\mathrm{UP}\rangle = \alpha_{\mathrm{UP}}|\mathrm{C}\rangle + \beta_{\mathrm{UP}}|\mathrm{X}\rangle \\ |\mathrm{LP}\rangle = \alpha_{\mathrm{LP}}|\mathrm{C}\rangle + \beta_{\mathrm{LP}}|\mathrm{X}\rangle \end{cases} \qquad \text{(eq. 1.9)}$$

where $\alpha_{\mathrm{UP,LP}}$ and $\beta_{\mathrm{UP,LP}}$ are the projections of the polaritonic states on the photonic and

excitonic states, with $|\alpha_{UP,LP}|^2 + |\beta_{UP,LP}|^2 = 1$. To simplify the notations, in the rest of the manuscript, we will omit the UP, LP index when mention a general polaritonic state.

The photonic and excitonic weights of the polaritons, also known as photonic and excitonic fractions or Hopfield coefficients, are respectively given by:

$$\begin{cases} W_C = |\alpha|^2 \\ W_X = |\beta|^2 \end{cases} \quad \text{(eq.1.10)}$$

Due to their hybrid nature, polaritons inherit the properties of both excitons and photons through the excitonic fraction and photonic fraction respectively. For example, the polaritonic effective mass, group velocity and linewidth can be calculated from the effective mass, group velocity and linewidth of the uncoupled photons and excitons [4]:

$$\frac{1}{M_{pol}} = \frac{W_C}{M_C} \quad \text{(eq. 1.11)}$$

$$v_{pol} = W_C . v_C \quad \text{(eq. 1.12)}$$

$$\gamma_{pol} = W_C . \gamma_C + W_X . \gamma_X \quad \text{(eq. 1.13)}$$

Here M_{pol} and M_c present the effective mass of the polariton and of the confined photons, respectively; v_{pol} and v_c present the group velocity of the polariton and of the confined photons respectively. γ_{pol}, γ_C, γ_X stand for the loss rates corresponding to polaritonic, photonic and excitonic states. We note that the exciton effective mass is orders of magnitude higher than the photonic one, and can be considered as infinite here. As a consequence, the group velocity of excitons is much smaller than the photonic one, and can be considered as zero here.

An important physical quantity which is often measured to characterize a polaritonic system is the photoluminescence signal. The photoluminescence intensity (I_{PL}) is directly related to the flux of photons leaking from the polaritonic states, thus is given by:

$$I_{PL} \propto W_C . \gamma_c . N_{pol} \quad \text{(eq. 1.14)}$$

where N_{pol} is the polariton density of the considered state.

From the previous hybridized quantities, we conclude that polaritons inherit a finite effective mass and ballistic propagation from the photonic component, as well as the losses from both excitonic and photonic components. Using (eq.1.12) and (eq.1.13), one may easilty calculate the polaritonic propagation distance. Moreover, polaritons also inherit the giant $\chi^{(3)}$ nonlinearity from the excitonic components, which can be orders of magnitude higher than the photonic Kerr nonlinearity [5]. This nonlinearity is transferred from the exciton fraction to the polariton by a coefficient W_X^2. As consequence, in a practical point of view, one may consider exciton-polaritons as ultra-nonlinear photons to make all-optical devices but with much smaller commutation energy than pure photonic devices.

1.3.3 A short panorama of different exciton-polariton platforms

The two ingredients to make a polaritonic platform are choice of excitonic material and photonic confinement scheme. In the following, we will present a panorama of different exciton-polariton platforms based on the variety of these two ingredients.

On the material side, pioneering work on exciton-polaritons was performed with GaAs and CdTe based quantum wells [6]. Although these materials, especially GaAs, are still the most used excitonic materials for studying polaritonic physics, their operation is limited to cryogenic temperatures due to the modest excitonic binding energy of few meV [7]. In view of making polaritonic devices suited for practical applications, a quest has been set towards room temperature excitons, and therefore the use of materials of high excitonic binding energy such as GaN [8,9], ZnO [10,11], organic semiconductors [12–14] and, more recently, monolayers of transition metal dichalcogenides (TMDs) [15–20] and inorganic perovskites [21–26].

For the photonic confinement scheme, most of the works are based on planar vertical

microcavity [6,12,27–34, 35] which can be considered as the text-book example of exciton-polaritons (see Figure 1.2 and Figure 1.3). The advantage of this approach is its simplicity in both design and needs for fabrication facility which "only" require multilayer modelling and multilayer deposition respectively. As a matter of fact, the first strong coupling investigation of many excitonic materials has been made with the planar microcavity configuration. To study more complex phenomena and polaritonic dispersions, this text-book scheme has many derivations in which the microcavity are patterned into microstructures [36–42], to engineer potential landscape for emulating non-linear Schrödinger equation via polaritonic states. However, there are several drawbacks for the planar microcavity approach and its derivations: i) the stack is very thick and it is very challenging for making electrically injected devices, ii) the multilayers approach is not compatible with the CMOS technology, iii) the engineering of polaritonic properties by micropatterning is only in the supra-wavelength scale, thus tailoring polaritonic properties in the subwavelength scale is almost unexplored.

Another photonic confinement strategy to generate exciton-polaritons is based on photonic crystal slabs in which the excitonic material is either embedded inside the photonic crystal [43,44], exfoliated on top for the case of 2D materials [15,18,45], or infiltrated inside [46–48]. In these schemes, the strong coupling take places between the excitons from the active material, with photonic resonances confined in photonic crystal. These exciton-polaritons are also called photonic crystal polaritons [43,44] to distinguish from the text-book exciton-polaritons with vertical cavity. Compared to the microcavity approach, the design and concept of photonic crystal is much more complex and often requires powerful numerical methods. The fabrication is also in general more complicated due to the necessity of lithography and etching processes to make nanophotonic structures. However, since the stack of a photonic crystal slab is much simpler and considerably thinner than a vertical cavity, it will be much easier to reach the active layer for electrical injection. Moreover, the maturity and wealth of

nanophotonic concepts for photonic crystal make this approach extremely appealing and promising for exploring new polaritonic physics.

1.3.4. Excitonic metasurface

In this thesis, we adopt the photonic crystal approach and the use of halide perovskite material to study polaritonic physics. Therefore, in the rest of this chapter, a detailed overview of halide perovskite for polaritonic applications, and main concepts of the photonic confinement in subwavelength photonic crystal slab will be given.

However, in our work, instead of integrating a small amount of excitonic materials into/onto a passive photonic crystal slab, the excitonic material it-self is directly patterned into subwavelength scale photonic crystal of nanopillar lattice (see Figure 1.4). Thus the active material itself is the host for the photonic confinement. As consequence, our original approach allows investigating an unexplored polaritonic regime generated on the basis of collective behaviors of sub-wavelength active elements. We call the platform of such ensemble of excitonic nano-pillars "excitonic metasurface".

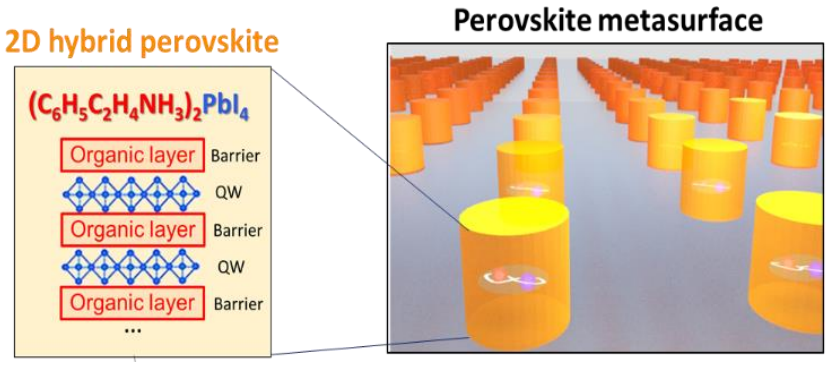

Figure 1.4. Illustration of the perovskite excitonic metasurfaces that are studied in this thesis.

1.4 Lead halide perovskites for polaritonic applications

1.4.1 Lead halide perovskites

Perovskite is a large group of materials which have the similar crystal structure as the one of calcium titanium oxide ($CaTiO_3$). This first perovskite was discovered by the German

mineralogist Gustav Rose in 1839 and was named after the Russian mineralogist Lev Alekseevich von Perovski (1792- 1856).

In the recent years, research on lead halide perovskites have attracted tremendous attentions and shown a rapid rise in terms of number of publication per year. This emergence is due to the exceptional electrical and optical properties of these materials. For example, they possess high absorption coefficient along with efficient charge transport, long diffusion length, and low non-radiative recombination rates compared to other thin-film polycrystalline semiconductors. These remarkable properties make lead halide perovskites the leading candidate for new generations of highly efficient and low-cost photovoltaic (PV) devices [49]. In addition, perovskites have other fascinating properties, such as bandgap tunability in a wide range, high luminescence quantum yield, narrow emission linewidth, and strong exciton binding energy needed for high temperature operation. Perovskites are also highly promising for various photonic applications such as light emitting diodes [50–52] and lasers [53–55].

The most common crystal structure of perovskite is ABX_3 of three dimensional (3D) perovskite compounds. In this compound, A is an organic cation (or metallic cation in all-inorganic perovskites) that fits inside the body center of the cube made of inorganic ($[BX_6]_4-$) octahedrons; B is a divalent metal cation (usually lead Pb) while X is a halide anion that can be iodine (I), bromide (Br) or chloride (Cl).

Perovskites also have lower dimensional (2D, 1D and 0D) arrangements, where the cations (normally the organic chains) are too large to fit into the cubic center. In this scenario, the crystal lattice is unable to form 3D structure, leading to sheets (2D), wires (1D) or individual cubic dots (0D) which exhibit quantum confinement behaviors.

In particular, layered perovskites have Ruddlesden-Popper structure of general formula $R_2A_{n-1}B_nX_{3n+1}$. A is the “small” cation. R is the cation made of large organic groups such as aliphatic or aromatic alkyammonium which act as a spacer separating the inorganic sheets. n is

the number of inorganic sheets that are attached together in each layer (see Figure 1.5). The n=1 case is called 2D layered perovskites or just 2D perovskite, while 0>n>1 cases are called 2D-3D perovskites. After being deposited, the crystallization of layered perovskites leads to self-assembly alternating multilayers of one organic and inorganic monolayers. These multilayers can be considered as multiple quantum well structure in which excitons are confined within the inorganic layer while the organic chains play the role of barriers. The best excitonic confinement is evidently for the case of n=1 (2D layered perovskites).

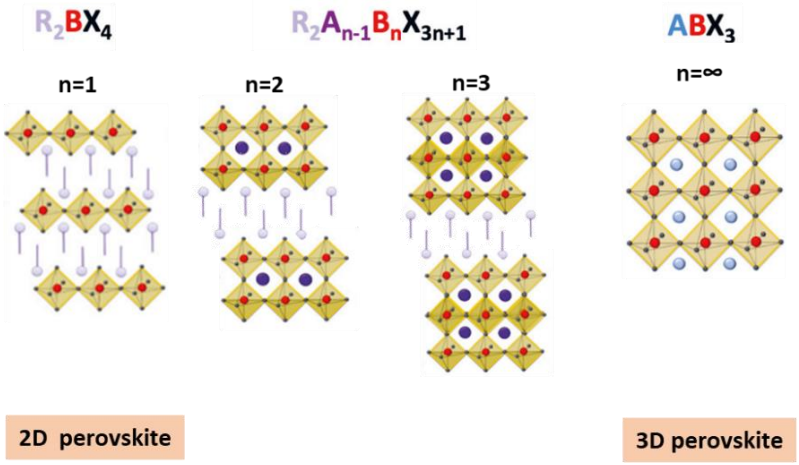

Figure 1.5. Structure of perovskite from 2D to 3D. Images adapted from [56].

1.4.2 Strong coupling with three-dimensional perovskites

3D halide perovskites were only considered for polariton applications in last few years, after these materials caught attention in the PV field. The strategy to strengthen the excitonic properties of the 3D perovskites is to form lower dimensionality crystal in e.g. nanowires (1D) and nanoplatelets (2D) where the confinement brought the electrons and the holes closer. A lot of progress has been achieved on the crystal quality and room temperature strong couplings were observed [22,23,25,26,57–62]. In 2017, Rui et al., report on the first perovskite polariton lasing with the use of 3D all-inorganic $CsPbCl_3$ nanoplatelets incorporated in microcavity (see Figure 1.6a-c). Following that, polariton condenstations were reported with microcavities containing $CsPbBr_3$ nanowire showing polariton propagation of over 60 μm (see Figure 1.6d-

f) and $CsPbBr_3$ micropillar array creating a lattice of polariton condenstates. In most of the works for polariton demonstration, 3D perovskites were formed in low dimensional crystal arrangements (nanowires, nanoplatelets, etc.). However, in 2019, Bouteyre et al. proved that room temperature strong coupling regime can be achieved using a 3D perovskite $MAPbBr_3$ thin film in a microcavity [63].

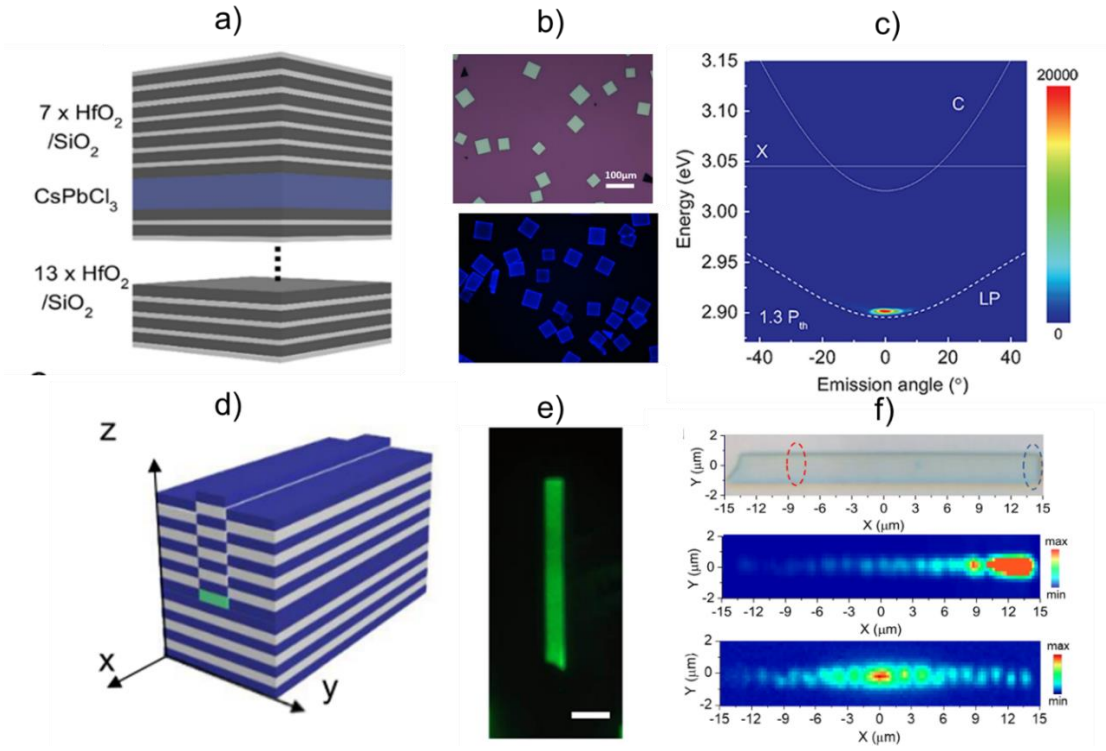

Figure 1.6. Example of 3D halide perovskite - based polariton system. a) CsPbCl3 crystalline nanoplatelet embedded in a planar microcavity. b) Microscope and fluorescence images of $CsPbCl_3$. c) Angle-resolved PL spectrum above threshold (Images extracted from [58]). d) Schematic of the CsPbBr3 microwire microcavity. e) Fluorescence images of $CsPbBr_3$. Scale bar, 5µm. f) From up to down, pumping spot and collection spot on the microwire micro- cavity; measured at room temperature and simulated real-space images of the microwire microcavity above the polariton condensate threshold. (Images extracted from [22]).

For polaritonic applications, the 3D perovskites possess lower binding energy in comparison to the 2D forms as they lack of natural confinement coming from the large organic groups. Therefore, beside few exceptions, most of works on room temperature exciton

polaritons use 3D all-inorganic perovskites. On the other hand, the 3D perovskites have better charge transport than the 2D perovskites which makes them more compatible for electrical injection [64]. However, unlike with hybrid perovskites, it is challenging to obtain large area inorganic halide perovskite films with good morphology and high crystal quality using all solution based deposition [65].

1.4.3 Strong coupling with two-dimensional layered perovskites

While the emergence of 3D perovskites in e.g. $CH_3NH_3PbX_3$, has risen tremendous attention in the PV field, 2D perovskites were most studied due to their excellent excitonic properties, and are considered as the most appealing candidates for room temperature strong coupling demonstration. In particular, bi-(phenethyl ammonium) tetraiodoplumbate, known as PEPI with chemical formula $(C_6H_5C_2H_4NH_3)_2PbI_4$ (see Figure 1.7), is widely regarded as the most studied perovskite for polaritonic applications. Remarkable excitonic features in PEPI are thanks to a double confinement effect. First, the alternating organic/inorganic monolayers features the multi-quantum well structure with the organic layers ($C_6H_5C_2H_4NH_3$) playing the role of potential barriers (1 nm) that are able to confine the electronic excitation within the 0.5 nm of inorganic quantum wells [66,67]. Moreover, the confinement effect is strengthened thanks to the high dielectric contrast between the organic and inorganic layers [68]. The combination of quantum confinement and dielectric confinement results in the high oscillator strength as well as high exciton binding energy, ranging up to hundreds of meV at room temperature [69].

In the linear regime, using the Lorentz oscillator model of (eq.1.1), the excitonic resonance of PEPI is featured in the dielectric function as [70]:

$$\varepsilon_{PEPI}(E) = n_{PEPI}^2 + \frac{A_X}{E_X^2 - E^2 - i\gamma_X E} \qquad \text{(eq.1.15)}$$

where n_{PEPI} =2.4, E_X =2.394 eV, γ_X=30 meV and A_X = 0.85 eV^2. Additionally, PEPI has been

reported to have higher nonlinearity related to the delocalized Wannier excitons in comparison with Frenkel excitons in all-organic materials [71].

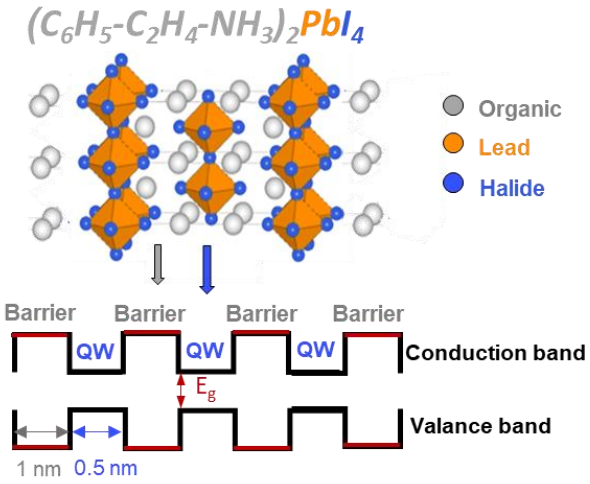

Figure 1.7. Schematic presentation of PEPI perovskite molecular structure.

It is interesting to note that the first perovskite based polaritons were demonstrated even before "perovskite fever" and mostly with PEPI or PEPI-like perovskites. In 1998, Fujita et al. experimentally demonstrated for the first time perovskite polariton by spincoating PEPI solutions on distributed feedback resonators (DFB) [46] (see Figure 1.8.a,b,c) . Shimizu and Ishihara in 2002 also studied the strong coupling in 2D perovskite integrated DFB structures and observed non-linearities of the polariton dispersion curves arising from the excitonic component of the polaritons [72]. While the DFB structure can be regarded as a 1D photonic crystal, strong coupling effects were later observed by infiltrating 2D perovskite in 2D and 3D photonic crystal [47,48] (see Figure 1.8.d,e). Furthermore, a lot of work considered vertical microcavities as photonic design making it the most popular platform for perovskite polariton demonstration due to its straightforward design and the ability to achieve high quality factors [27,73–79]. In attempt to obtain low dimensional polaritons for potential devices, even 0D polaritons based on PEPI were demonstrated [80] (see Figure 1.9). This has been achieved by implementing a sphere-like defect onto the top Bragg mirror of the vertical microcavity to

achieve a 0D photonic confinement. The pioneer works on 2D perovskite polaritons focused on optimizing the photonic cavity while the perovskite films were simply prepared by spincoating. Since 2012, much work has been done to enhance the crystal quality of perovskite deposition [81]. 2D single crystal perovskite with much higher quality were synthesized using AVCC technique (anti-solvent vapor-assisted crystallization) [82]. The strong coupling effect was even observed in bare 2D perovskite crystal (few micrometers in thickness), without the use of an external cavity [67]. In 2019, the polariton-polariton interaction was investigated in

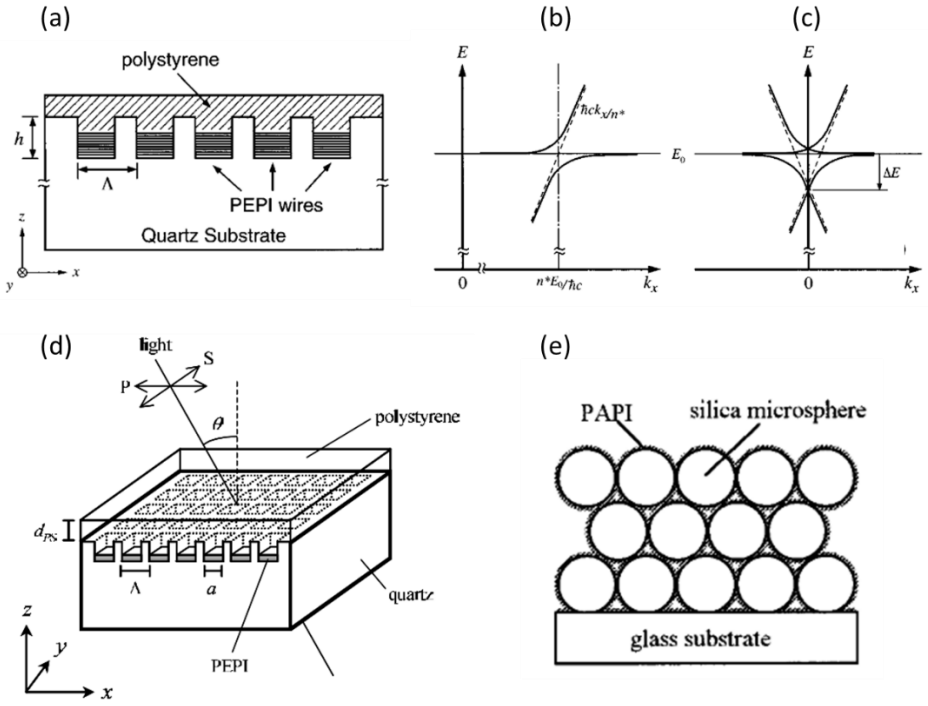

Figure 1.8. Example of early works on strong coupling demonstration using PEPI perovskite (a) Sketch of PEPI integrated with the distributed feedback (DFB) structure studied by Fujita et al. (b) The zoom in of the anti-crossing area and (c) the theoretical polariton dispersion in the DFB microcavity. The solid lines are polariton dispersion curves, and the dashed and thin lines are the uncoupled guided-wave and exciton dispersion curves (extracted from [46]). (d) PEPI filled inside 2D square lattice photonic crystal. Image extracted from [47]. (e) Schematic representation of a structure of silica opal infiltrated with PEPI (called here PAPI) (extracted from [48]).

exfoliated single 2D perovskite crystal embedded in a planar cavity [83].

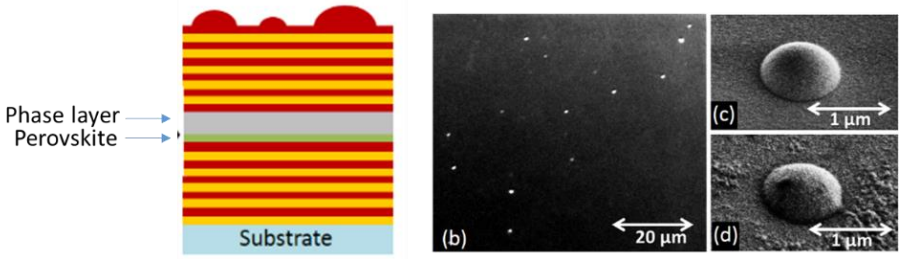

Figure 1.9. (a) Structure of zero-dimensional (0D) perovskite-based polaritons in sphere-like defects. (b) Top view optical microscopy image of the sample. (c) SEM image of a sphere-like defect in the top Bragg mirror. (d) SEM image of a sphere-like defect of the top Bragg mirror on the final sample. Images extracted from [80].

These previous works show that PEPI thin films fabricated just by simple spincoating, even without crystal quality enhancement, are sufficient for demonstrating strong coupling at room temperature. In addition, PEPI perovskite is solution-processed, remains soft right after deposition. It is therefore possible to pattern it into different structures, either by infiltration into periodic lattices or thermal imprinting using patterned templates. Because of its excellent properties and its ease of fabrication, PEPI is chosen as the excitonic material in the work of this thesis.

1.5 Photonic modes in subwavelength periodic lattice

1.5.1 Photonic crystal and photonic crystal slab

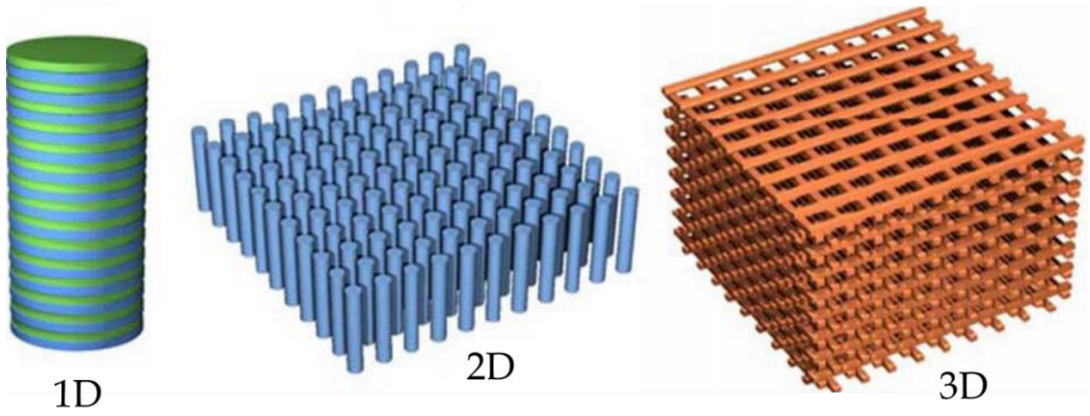

Figure 1.10. Examples of one-, two-, and three-dimensional photonic crystals.

Photonic crystal (PC) is the optical analogue of solid crystals where the atoms and molecules are replaced by media with different dielectric constants, and the periodic potential is taken place by a periodic dielectric function (or, equally, a periodic optical index). In photonic crystals, the dielectric constant is modulated periodically in one or more directions of space at the wavelength scale (see Figure 1.10). As a consequence, photonic modes in these structures are Bloch modes with photonic band structure in a similar fashion as electronic band structure of solid crystals. Moreover, the possibility to design the periodic structures give rise to the abilities of dispersion engineering, leading to unprecedented regime of light propagation (slow light at photonic band edges, total reflection in photonic bandgap).

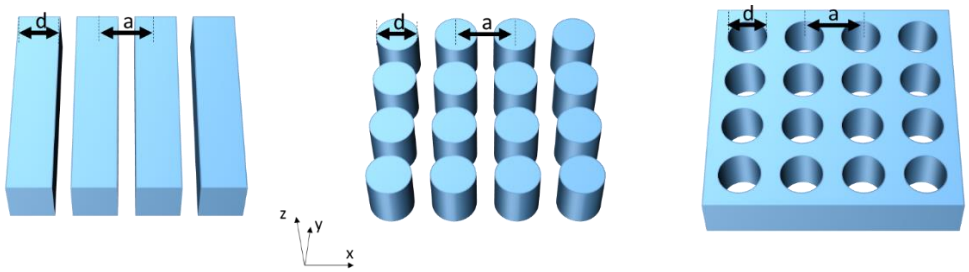

Figure 1.11 Examples of PC membrane structures.1D periodicity: lattice of dielectric material gratings; 2D periodicity: square lattice of dielectric pillars, square lattice of air holes in dielectric membrane.

Photonic crystal membranes or photonic crystal slabs are photonic crystals with 1D or 2D periodicity, but with finite thickness. The period and thickness of photonic crystal slabs are often in the subwavelength-scale (see Figure 1.11). Photonic modes in these structures are Bloch modes propagating in-plane and being vertically confined within the slab. Many features of photonic crystals can be found in photonic crystal slabs, such as photonic band structure (but only for in-plane wave vectors), dispersion engineering with photonic band-gap and band-edges. However, Bloch modes in photonic crystal slabs can eventually leak to the free-space, i.e. to the radiative continuum, and exhibit radiative losses. The leaky Bloch modes in photonic crystal slabs are called guided resonances (GR) or Bloch resonances. They are Bloch modes operating above the light cone of the photonic band structure ($\omega > c|k_{||}|$ where $k_{||}$ is the in-plan wavevector).

When combined with dispersion engineering concepts, the radiative leaky channel of GR "opens" the way to dictate light matter-interaction in various optoelectronic devices (light management and light trapping in thin-fim solar cells [84,85], extraction enhancement and high directionality for light-emitting diodes [86–88], far-field radiation pattern of lasing emission [89,90]. In this thesis, we investigate the use of these GR to tailor polaritonic features in excitonic metasurface based on subwavelength lattice PEPI of nanopillars. In the following sections, I will introduce some key features of GRs and their coupling with excitonic resonances.

1.5.2 Band folding and gap opening of guided modes and guided resonances

At first approximation, a photonic crystal slab can be regarded as a planar waveguide with the same thickness, and made of a medium with an effective refractive index. In this approach, the effects of the periodical corrugation is considered as a perturbation acting on the guided modes (GM) of the planar waveguide. This perturbation consists of diffraction and radiative coupling mechanisms that will be detailed in the following.

Most of essential concepts of GR can be introduced with the case of 1D photonic crystal slabs (1D gratings) thus we will first focus on this case so that these concepts can be thoroughly introduced. The case of GR in 2D photonic crystal slab will be presented in other chapters of this thesis.

By working with a sufficiently-thin slab (i.e. subwavelength thickness), and considering only one polarization (for example TE modes), the unperturbed planar waveguide can be limited in single mode operation. In such a configuration, lightwaves propagating along *x* axis within the waveguide correspond to two GMs, denoted $|+\rangle$ for forward propagation and $|-\rangle$ for backward propagation (see Figure 1.12.a). The dispersion of these modes are naturally bellow the light cone and are protected from any radiative loss (see Figure 1.12.a).

When introducing periodicity modulation of the permittivity into the waveguide, the GMs $|+\rangle$ and $|-\rangle$ get diffracted via Bragg scattering. This diffraction mechanism leads to two main effects which result in several important consequences (see Figure 1.12.b):

- **Band folding:**
  - Folded $|+\rangle$ and $|-\rangle$ can be brought to above the light line and become GRs.
  - Folded $|+\rangle$ and $|-\rangle$ may fulfill phase matching conditions at the crossing points.
- **Coupling between $|+\rangle$ and $|-\rangle$ modes:**
  - The interaction between $|+\rangle$ and $|-\rangle$ make light looping back-forth within the structure which is called Feedback mechanism (similar mechanism used in distributed feedback laser).
  - Gap opening can be achieved if the lattice constant is smaller than wavelength in the interested range (i.e. subwavelength scale).

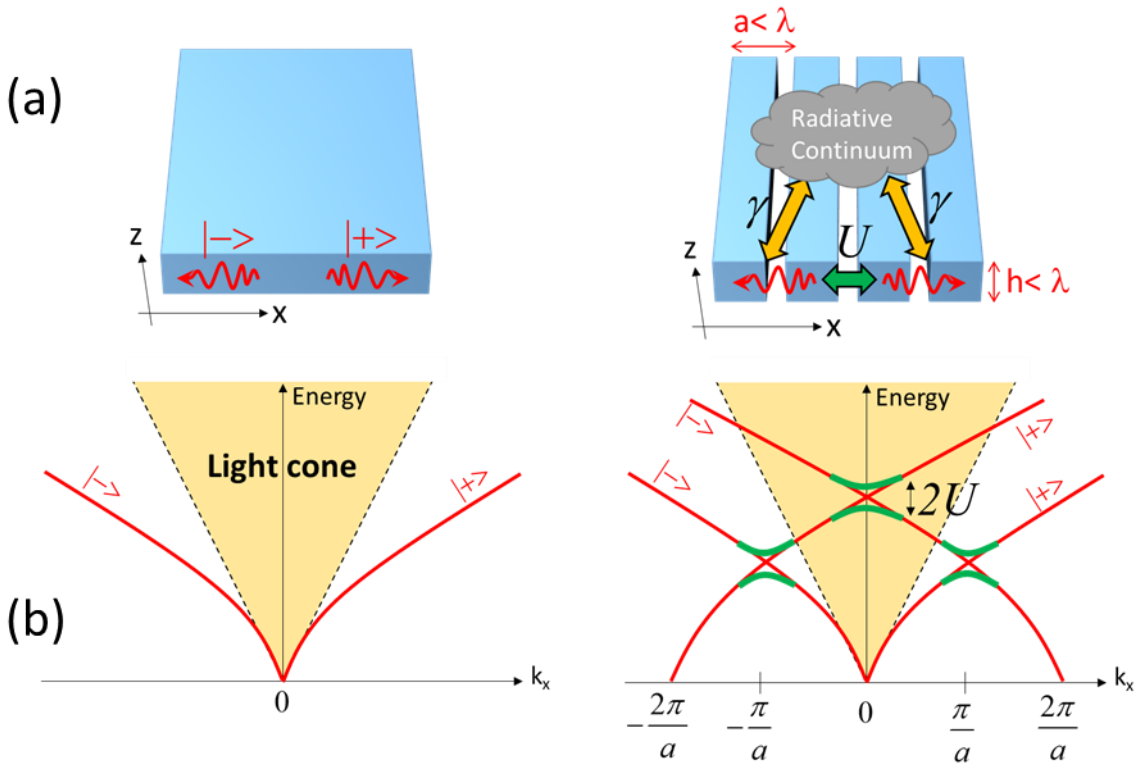

Figure 1.12. (a) GMs propagating along x-axis in a single-mode planar waveguide and the corresponding band dispersion. (b) Coupling mechanisms of GMs in a 1D grating and the corresponding band dispersions.

The detailed explanation of band folding and the mode coupling effect are discussed in the following.

A photonic crystal membrane with 1D periodicity is a modulated waveguide where the dielectric unit cell is repeated over and over in one dimension (i.e., x direction) with the lattice period a. Like in the solid state crystal, in photonic crystals the photonic states can be expressed by Bloch's theorem. The photonic Bloch state with wavevector k_x is identical to the photonic Bloch state with wavevector $k'_x = k_x + K_m$ with $K_m = mb;\ m \in Z$. Here b is the period in the momentum space (k-space) which is defined as $b = 2\pi/a$; and m is known as the diffraction order. The mode frequency in k_x is equal to the mode frequency at $k_x + K_m$ as $\omega(k_x) = \omega(k_x + K_m);\ \forall m \in Z$. Hence, for every wavevector period of $\frac{2\pi}{a}$, the dispersions are repeated

and identified. As a result, the band diagram $\omega_n\ (k_x)$ is completely defined within the primitive region $k_x \in \left[-\frac{b}{2}, \frac{b}{2}\right]$ or $\left[-\frac{\pi}{a}, \frac{\pi}{a}\right]$ which is the first Brillouin zone. As k_x repeats periodically, the modes are translated from one to the nearest neighbor Brillouin zone. Due to the mirror symmetry, this translation is equivalent to a folding of modes (hence, called **band folding**) where the center of the folding is at the edge of the Brillouin zone. The GMs which are brought above the light line because of band folding can couple to the continuum and become GRs.

Forward propagation GM $|+\rangle$ and backward propagation GM $|-\rangle$ are allowed to interact thanks to the phase matching condition at crossing points pinned at high symmetry points of the Brillouin zone. Using $|+\rangle$ and $|-\rangle$ as basis, one may describe this gap opening by a 2x2 Hamiltonian:

$$H_{grating}(k_x) = E_C + \begin{pmatrix} \hbar v k_x & U \\ U & -\hbar v k_x \end{pmatrix} \qquad \text{(eq.1.16)}$$

where E_C is the energy of the crossing point, v is the group velocity of the two GMs and U is the coupling strength between them.

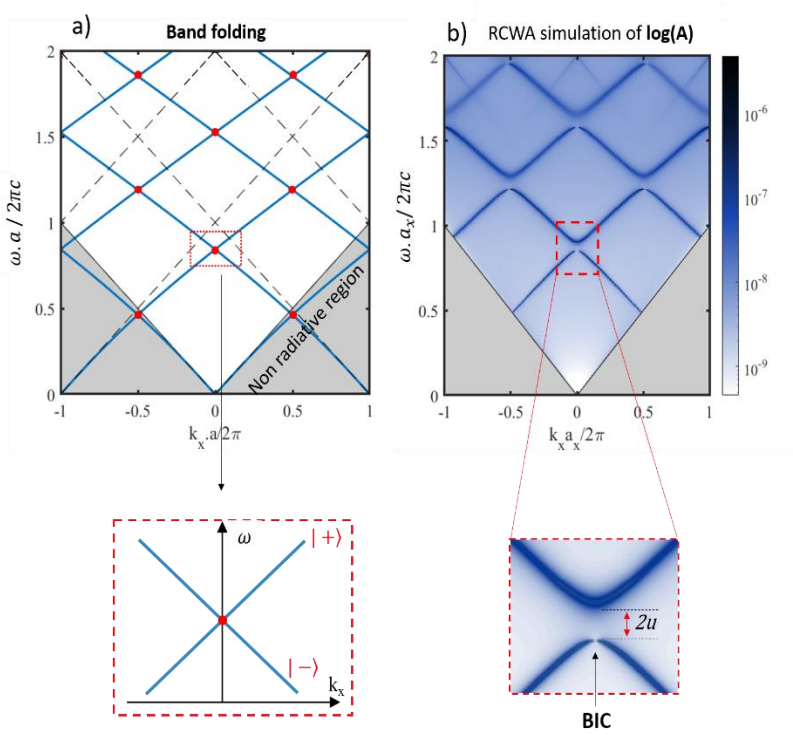

Figure 1.13 a) Photonic dispersions and b) the corresponding RCWA simulation in absorption of a 1D grating photonic crystal membrane (made of transparent material with real refractive index) showing strong coupling between guided resonances. a) Blue lines show the GMs and the GRs as a result of band folding. Red dots marked the crossing. The gray shaded region marked the non-radiative region. b) RCWA simulation in absorption shows photonic gaps and photonic BIC caused by the strong coupling between GRs.

One may verify easily that at k_x=0, the two eigenvalues of the previous Hamiltonian are $E_C \pm U$, leading to a bandgap opening with value of ~ *2U*. Moreover, since the value of *U* is dictated by the periodic modulation of the permittivity constant, the bandgap opening can be engineered by modifying the geometrical parameters of the system (filling factor, thickness, period…). This concept, when combined with the exciton-photon strong coupling regime and extended to more complex photonic lattice, would allow tremendous possibilities for polaritonic dispersion engineering. Proof-of-concepts of such mechanism will be discussed in Chapter 3 and Chapter 5 of this manuscript.

1.5.3 Radiative coupling of guided resonances and formation of bound states in the continuum

Figure 1.13 shows the band folding and the corresponding numerically simulated photonic band structure of GRs in a 1D photonic grating. In the band folding scheme (figure 1.13 left panel), crossing positions of GMs (modes below the light-line) and GRs (modes above the light-line) are marked as red dots. We note that the simulation is based on the Rigorous Coupled Wave Analysis (RCWA) method [91] and can only calculate GRs. From the results of these numerical simulations, we can see that at these crossing positions, the coupling between GRs leads to gap openings, as discussed in the previous section. The linewidth of the observed GRs correspond to the radiative losses of these modes. More interestingly, as can be observed from this figure, at the band-edge of the lower mode in every gaps, the linewidth vanishes suddenly, but then quickly "recovers" as soon as an oblique momentum is introduced.

The GR having zero radiative losses is known as a Bound state in the continuum (BIC) [94]. Such a BIC is formed due to destructive interference when GRs exchange losses via the radiative channel and induce a forbidden mode (i.e. dark mode) in the radiative continuum [93]. For the case of the coupling between two GRs at high symmetry points, one will take all radiative losses (constructive interference) while the other one becomes lossless or BIC (destructive interference). This mechanism can be quantitatively explained by implementing radiative losses and radiative coupling through the losses channel into $H_{grating}$ in (eq.1.16), leading to [94]:

$$H_{grating}(k_x) = E_C + \begin{pmatrix} \hbar v k_x & U \\ U & -\hbar v k_x \end{pmatrix} + i\gamma \begin{pmatrix} 1 & 1 \\ 1 & 1 \end{pmatrix} \qquad \text{(eq.1.17)}$$

where γ is the radiative losses of the uncoupled GRs (see Figure 1.11b). At k_x=0, the complex eigenvalues of the previous Hamiltonian are given by:

$$\begin{aligned} E_{GR1} &= E_C + U + 2i\gamma \\ E_{GR2} &= E_C - U \end{aligned} \qquad \text{(eq.1.18)}$$

The imaginary part in these eigenvalues confirm the losses exchange mechanism when $|GR1\rangle$ takes all losses and $|GR2\rangle$ is a BIC. Moreover, at k_x=0, the two eigenvectors of (eq.1.17) are given by:

$$\begin{aligned} |GR1\rangle &= \frac{|+\rangle + |-\rangle}{\sqrt{2}} \\ |GR2\rangle &= \frac{|+\rangle - |-\rangle}{\sqrt{2}} \end{aligned} \qquad \text{(eq.1.19)}$$

These eigenvectors show that the leaky mode is symmetric while the BIC is antisymmetric. Such conclusions confirm the agreement between the radiative losses and the symmetry of GR. Indeed, since free-space (i.e. the radiative continuum) consist of planewaves, the coupling between the continuum and an antisymmetric mode is forbidden, leading to a symmetry-protected BIC [92].

Not being able to couple with the external medium, photonic BICs are lossless and exhibiting infinite quality factor. Moreover, each photonic BIC in a periodic lattice can be attributed to a topological charge pinned at a polarization singularity in the farfield emission [95]. One may wonder if the lossless behavior and the topological nature of photonic BIC would be transferred to the polaritonic state when a photonic BIC is in the strong coupling regime with an excitonic resonances. This fundamental question will be addressed in the Chapter 4 of this thesis.

CHAPTER 2

FABRICATION OF PEROVSKITE METASURFACE, METHODOLOGY AND RESULTS

Molding halide perovskites into periodic structure has been a major topic for several research groups studying light-matter interaction and developing optoelectronic devices with advanced functionalities [1–15]. For 3D MAPbX perovskites, different techniques have been proposed in order to tailor on demand the structure of halide perovskite such as arranging the crystal growth [106] [98] [105], molding the surface by imprinting [100,104,105] or direct lithography [107], and combining perovskite with patterned substrates [103] [101,108–110].

However, there are not many developments dedicated to patterning of 2D hybrid perovskite. Spin-coating is one of the most popular methods which had been used to fabricate 1D perovskite grating at subwavelength scale [72] [102], 2D square lattice (with lattice parameters larger than the wavelength) [47], 3D glass beads lattice filled perovskite with 256 nm bead size [48]. Besides spin-coating, in 2003, Cheng et al. applied Micromolding in capillaries (MIMIC) – a method for fabricating perovskite grating with a high crystal quality; however, this technique is limited to 1D structure only, and the pattern size is still larger than the wavelength (0.8-50 um). With the aim of direct patterning of 2D layered perovskites, Kamminga *et al.* [105] reported on imprinting a 1D grating perovskite. The structure is successfully created but still with a large period, higher than 5 μm.

This chapter presents our solution-based fabrication process and the results of perovskite metasurfaces. Here, we utilized two methods: (1) infiltration of PEPI inside a pattern and (2) direct imprinting with a 2D structure. We show that it is possible to fabricate 2D lattice structures with overall good control of the size in the subwavelength range.

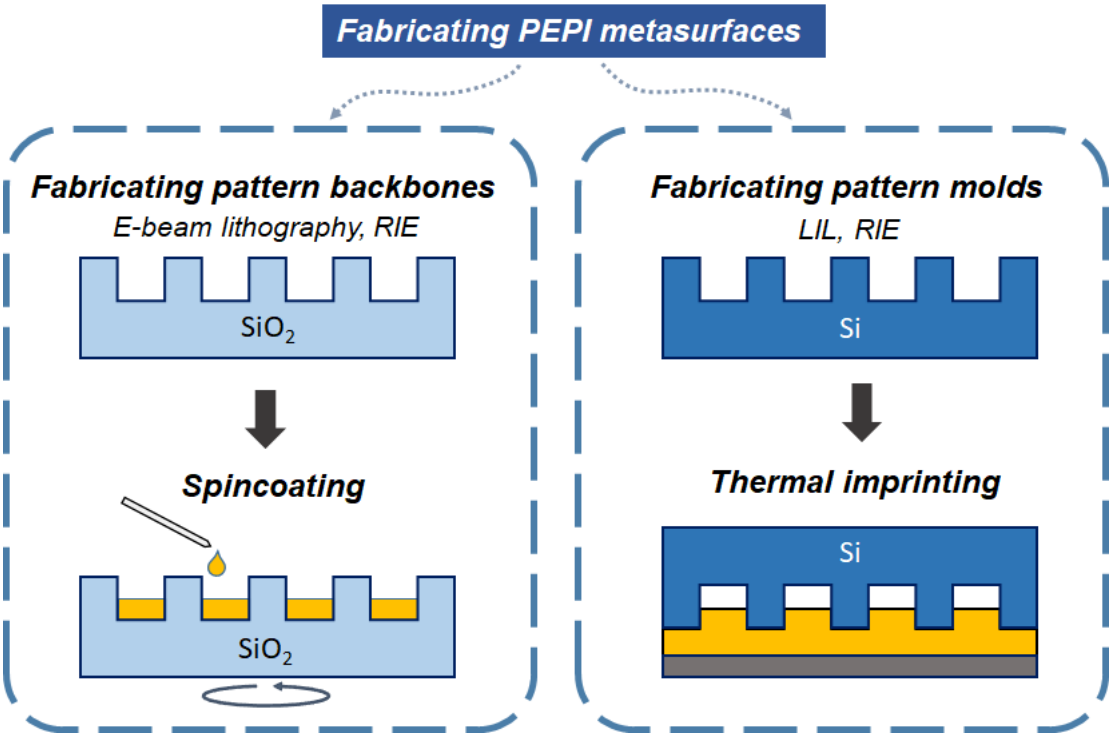

Figure 2.1. Fabrication schemes of PEPI metasurfaces via two methods: infiltration and thermal imprinting.

In this work, the technique we used for PEPI deposition is the standard one-step spin-coating.

With the infiltration method, PEPI is spin-coated and filled inside the patterned backbones made of a low refractive index material (fused silica). PEPI perovskite (with high refractive index $n \approx 2.4$) is infiltrated inside a hole lattice, creating an inverse pillar-lattice metasurface.

With the thermal imprinting method, thin film PEPI is first deposited on a substrate via spin-coating. Next, a mold with periodic nanostructures is laid on top of the deposited perovskite substrate. By applying a high pressure, the pattern is transferred to the perovskite film.

We used nanolithography to define the designed patterns on the silicon molds or the

silica backbones. Then these patterns are engraved into the desired materials by reactive ion etching (RIE). Two different techniques of lithography were used: E-beam lithography and Laser interference lithography. These two mask-less methods allow to directly pattern surfaces and thin layers. They are both compatible with the high resolution needed to fabricate metasurfaces.

Several techniques were used to characterize the deposited PEPI thin films and PEPI metasurfaces. X-ray diffraction (XRD) gives information on the crystal structure of the deposited PEPI thin films. The film morphologies were investigated by Scanning electron microscope (SEM) and atomic force microscopy (AFM). A homemade spectrometer setup was used to study the PEPI optical properties (i.e., photoluminescence (PL) – absorption). Our setup also enables Fourier spectroscopy for angle-resolved reflectivity (ARR) or angle-resolved photoluminescence (ARPL) measurements to study the band diagram of fabricated metasurface (see Appendix A). We used two lights in this thesis: a halogen lamp (DH-2000, Ocean optics) and a laser emitting at 405 nm (PDL 800-D, PicoQuant).

The results of the fabrication are shown in the following.

2.1 Thin film perovskite deposition

We started by studying the deposition of thin film PEPI. As a preliminary step, the deposition of thin PEPI films is studied. Substrates were cleaned and prepared for deposition. Surface treatment plays a vital role in perovskite deposition. Here, the substrates are dipped in solvents (acetone, ethanol, isopropanol – IPA) in an ultrasonic bath for 15 min for each step and then processed in a UV- ozone box for 20 min. It is noted that ozone treatment is necessary to enhance the surface energy of SiO_2 and to improve the homogeneity of perovskite deposition. Notably, the PEPI solution did not adhere to SiO_2 surface without UV treatment after spin-coating.

After surface treatment, substrates are loaded into the glovebox filled with nitrogen for perovskite deposition. PEPI is deposited onto the substrates using a one-step spin-coating PEPI/DMF solution at a rotation speed in the 3000-5000 rpm range, during 30 sec. PEPI solutions are dropped and spin-coated on SiO_2 surface with 25 µl of solution, onto 1.85x1.85 cm substrate. After the deposition, the PEPI thin film is annealed at 95°C for 90 sec.

Last, a thin film of poly(methyl methacrylate) (PMMA) is deposited on top to encapsulate and isolate the PEPI film from oxygen and humidity. PMMA encapsulation had been investigated to improve the photostability of perovskites [111]. PMMA film is prepared by spin-coating resist PMMA A4 950 at 3000 rpm in 30 sec.

PEPI perovskite solutions in DMF with different concentrations (wt 10%; 20%; 50%) were prepared by the research group of Emmanuelle Deleporte and Gaëlle Trippé-Allard at Laboratoire Lumière, Matière et Interfaces (LuMIn) in the frame of our collaboration. Morphologies of the deposited PEPI thin films are evaluated and shown in Figure 2.2. From the SEM images, we can estimate the thickness of PEPI. For PEPI thin film prepared by solution 10%, it is around 50 nm – 80 nm. By spin-coating solution wt 20%, PEPI films with thicknesses ranging from 120 nm to 150 nm can be achieved. Meanwhile, the thickness of PEPI film deposited by spin-coating solution wt 50% is in the range of 650 nm – 700 nm.

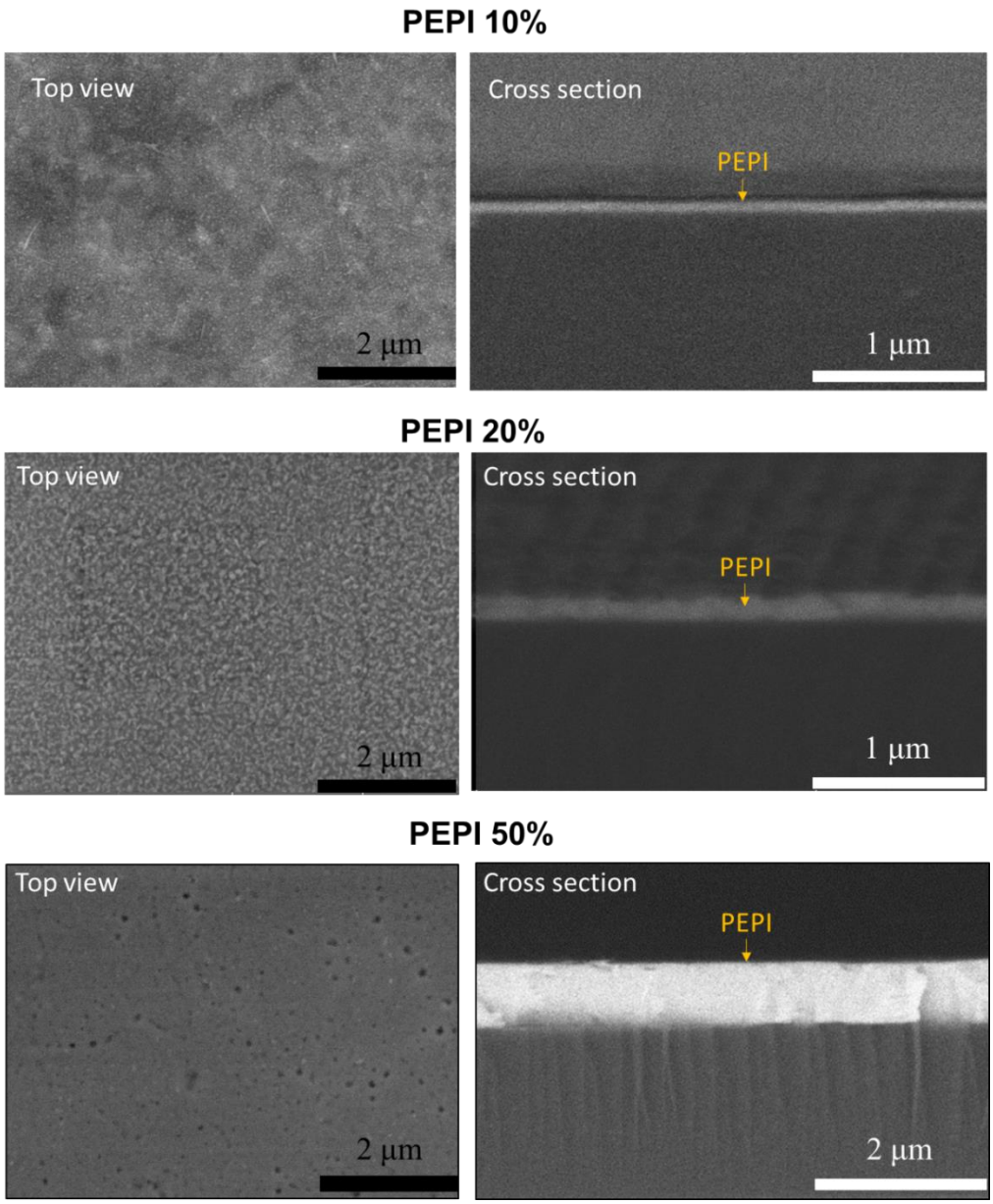

Figure 2.2 Top and view cross section SEM views of samples with PEPI deposited by spin-coating, with 10% 20% 50% wt solutions. By SEM cross-section, we can estimate the thickness of PEPI 10% (50-80 nm), PEPI 20% (120-150 nm), PEPI 50% (650-700 nm).

PEPI 10% wt and 20% wt solutions are our final choice to fabricate PEPI metasurface. Indeed, the 50% wt solution is incompatible with our objective as its resulting film thickness is much larger than the wavelength. In addition, the SEM image (Figure 2.3) shows that by a spin-coating solution of 50% wt, cracks appear on top of the surface after annealing.

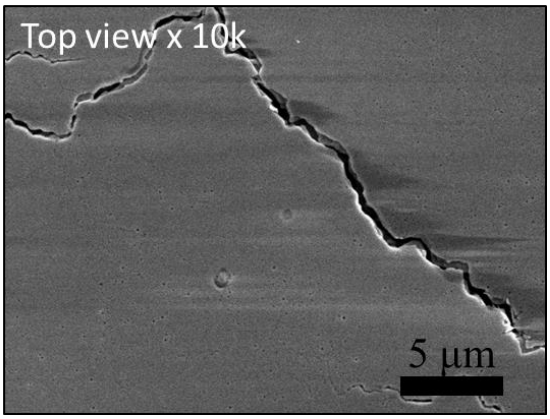

Figure 2.3. SEM images of PEPI film by spin-coating 50% wt solution, showing cracks appearing on the surface.

The crystal quality of PEPI thin film is then characterized by X-ray diffraction (XRD). Figure 2.4 presents the XRD pattern measured on a 50 nm thick PEPI film (encapsulated in PMMA), deposited on a fused silica substrate. XRD measurement shows typical peaks of PEPI crystalline structure, [0 0 2l], with l = 1 – 6. This observation of a number of diffraction orders proves that the thin layer has high crystallinity and the layer stacking has good periodicity. The result is coherent with the previous reports [69,111,112].

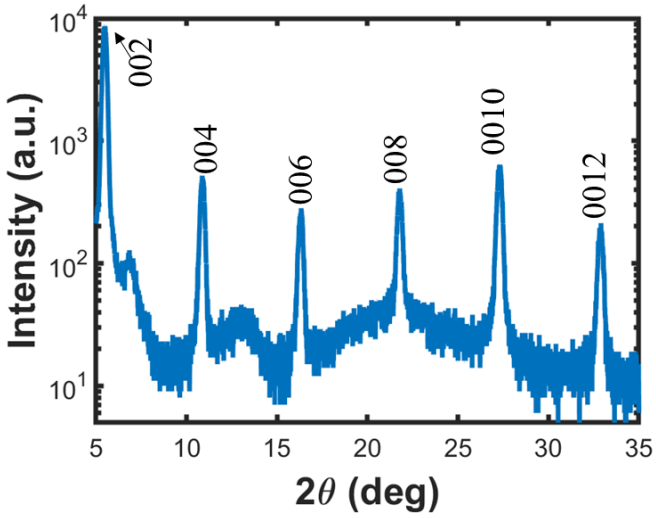

Figure 2.4. XRD pattern of 50 nm film of PEPI (with 200nm of PMMA on top) on fused SiO_2 substrate.

The optical characterization result for our PEPI thin film (prepared by PEPI wt 10%) is shown in Figure 2.5. Under excitation at 3.06 eV, the PL spectrum exhibits a relatively sharp emission peak at 2.36 eV with a full width at half maximum of 0.062 eV. The absorption spectrum displays a strong peak at 2.41 eV, almost superimposed on the PL spectrum. These spectral features show an excitonic behavior at room temperature. The absorption continuum in the UV range corresponds to the absorption above the bandgap of the semiconductors. The strong excitonic peak and continuum observed in the absorption spectrum at room temperature agree with the results reported in the literature [113].

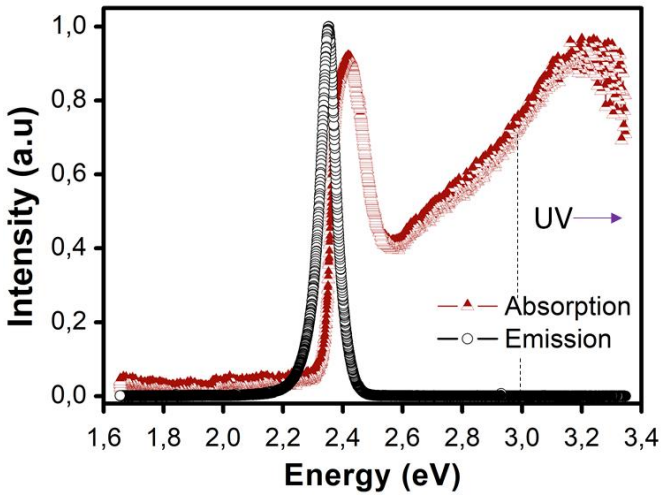

Figure 2.5. The absorption and the PL spectra of 50nm PEPI film

We then studied the photostability of PEPI thin films prepared by spin-coating a PEPI wt 10% solution. PEPI thin films are exposed under continuous wave (CW) laser and pulsed laser ($t_{pulsed} \approx$ 50ps, repetition rate of 80 MHz) in the UV (λ=405 nm). As seen in Figure 2.6, the PL emission intensity of a bare PEPI thin film (colored blue) dropped under continuous laser exposure. Such a photobleaching behavior, already observed in hybrid perovskite materials, has been explained by the photodegradation of organic compounds in perovskites [114]. After being encapsulated by PMMA, PEPI films exhibit PL with a significant improvement of photostability under both CW laser and pulsed laser irradiation.

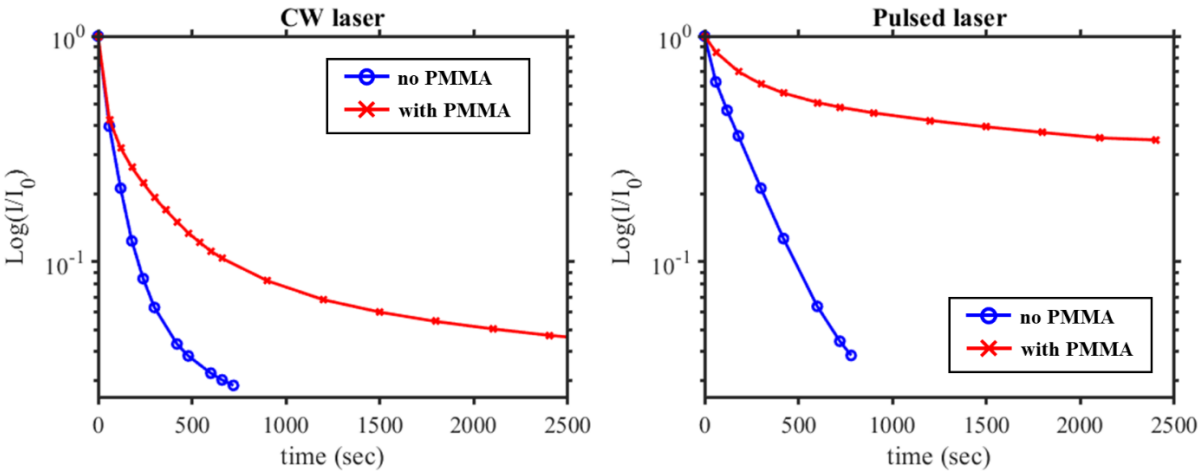

Figure 2.6. PL intensity of PEPI thin film (wt 10%) deposited on SiO_2 substrates with PMMA on top (red crosses) and without PMMA (blue dots). Thin films PEPI were exposed continuously to CW laser (left panel) and pulsed laser (right panel).

Under CW irradiation, PL signal of bare PEPI film quickly decreased, down to around 2% of the initial value, after 10 min (600 sec) of exposure. Meanwhile, PL emitted by PMMA/ PEPI film was only decreased to 10% intensity after the first 10 min of exposure, then slowly declined to 4% after around 40 min (2400 sec). Under pulsed irradiation, PL intensity of bare PEPI film constantly dropped to around 3% after the first 10 min of exposure. On the other hand, PL intensity of PMMA/ PEPI film decreased at a much slower pace, reduced to above 40%, even after 40 min of exposure.

The optical characterization results show that PEPI is quickly degraded under continuous CW exposure, compared to pulsed laser illumination. In all optical characterization performed subsequently, we decided to use only pulsed laser. In both cases, under exposure to CW laser or pulsed laser, we have observed that the photobleaching effect (related to light and heat degradation of PEPI) is much slower with the use of PMMA. In our later work, PMMA is therefore also spin-coated on top of the fabricated PEPI metasurfaces.

2.2 PEPI metasurface fabricated by infiltration

Our first approach is to fabricate PEPI metasurface via the infiltration method. First, low refractive index backbones with nanostructures made of SiO_2 are fabricated. PEPI solution is then spin-coated on top of these pre-patterned backbones.

2.2.1 Backbone fabrication

First, the backbones were fabricated via electron-beam lithography and reactive ion etching (RIE). The negative patterns (i.e. hole lattices) are defined in PMMA A4 950 Microchem resist using an e-beam lithography system (FEI Field effect gun SEM equipped with the Raith Elphy plus pattern generator) followed by the development with an MIBK/IPA solution. Later, the patterns are transferred into the fused silica substrate by Reactive Ion Etching using a mixture of CHF_3, O_2, SF_6 gases under pressure of 10-50 mTorr. The process follows the procedure of photonic crystal fabrication via e-beam lithography, which was developed and optimized in INL [115].

E-beam lithography allows for creating precise patterns with high resolution (down to a few nm). In addition, e-beam lithography is an ideal technique to achieve our objective of studying dispersion engineering. For example, we can fabricate multiple structures with different lattice parameters on one sample (Figure 2.7). This method gives a chance to test various designs and presents high flexibility to investigate dispersion engineering. On the other hand, all our samples are etched by RIE due to its high etching rate and anisotropic etching property, which can produce close-to-vertical sidewalls.

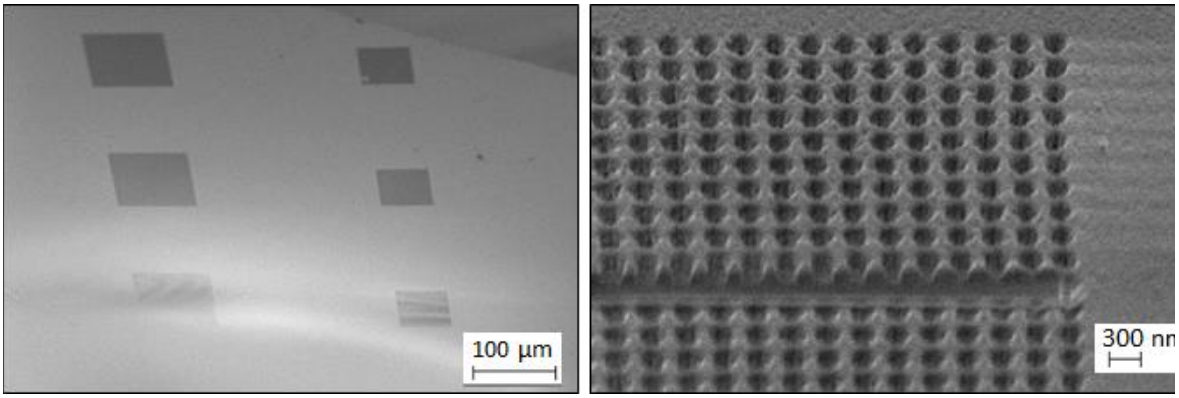

Figure 2.7. Fabricated SiO_2 backbone achieved by e-beam lithography and RIE. [Image obtained by Focused Ion Beam milling combined with SEM (FIB-SEM)]. Size of the lattices is in the range of 50-80 µm in one dimension.

E-beam lithography is incompatible to fabricate large-scale lattices as it is a high cost and time consuming process. Thanks to its flexibility and precision, we first utilized e-beam lithography to study different structures and to select the good lattice parameters. Then, in order to pattern large areas, we have selected an alternative process to e-beam lithography. Laser interference lithography (LIL) is a maskless lithography technique using two coherent beams to expose the photoresist layer. An interference pattern of these coherent beams (exhibiting as periodic fringes of minima/maxima intensity) is created and defined in the photoresist film. Finally, the patterns are revealed after post-lithography processing (post-bake, development). The pattern size of LIL is proportional to the wavelength of the light source. The LIL conditions have been developed and optimized by our research group in INL [116]. Although LIL is clearly overcome by e-beam lithography in terms accuracy, homogeneity and resolution, we have selected this approach for PEPI imprinting since it enables fast patterning at a reduced cost. The substrates of backbones are 2 µm SiO_2 on Si. The patterns were etched by RIE using the similar SiO_2 recipe to e-beam lithography backbones. SEM characterization (Figure 2.8) shows the morphology of LIL fabricated backbones.

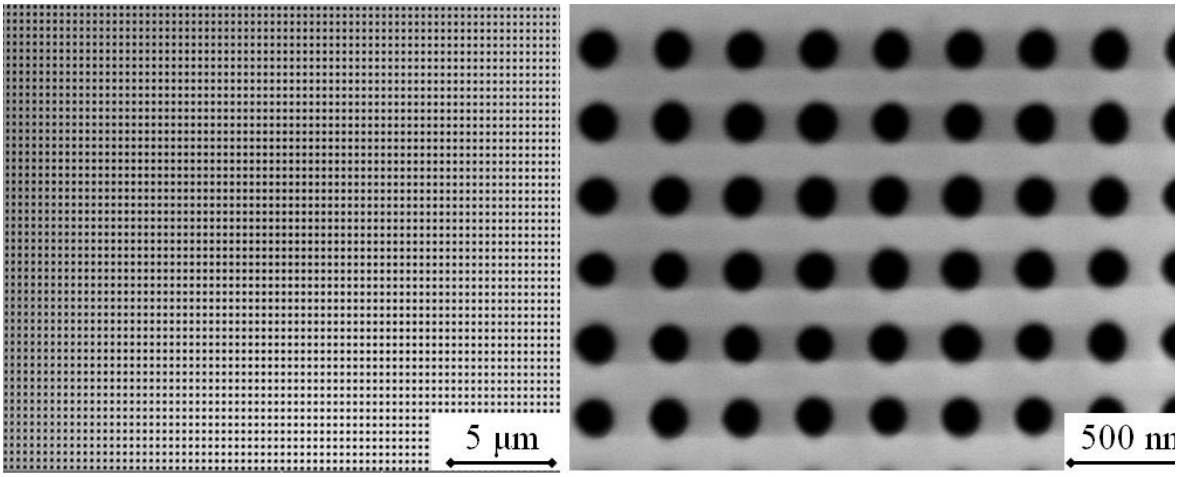

Figure 2.8. Top view SEM fabricated SiO_2/Si backbones achieved by LIL and RIE.

2.2.2 PEPI infiltration

After being patterned, the SiO_2 backbones are cleaned and ozone-treated before PEPI deposition (Figure 2.9). PEPI solutions 10% wt and 20% wt were spin-coated on top of the backbones with the same conditions as for planar thin film deposition. All PEPI deposition is carried out inside a glovebox filled with N_2.

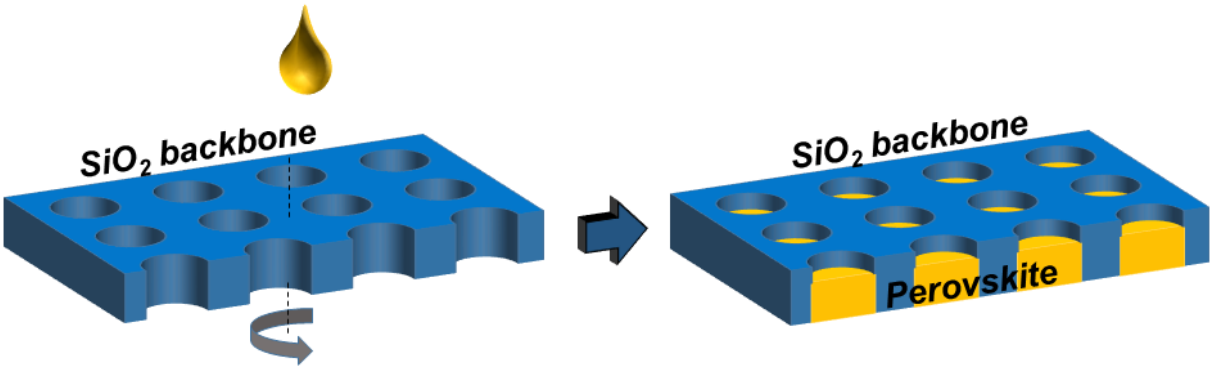

Figure 2.9. Sketch of the perovskite infiltration method.

In order to verify the infiltration of PEPI inside the patterns, we conducted angle-resolved characterization to verify the presence of the photonic modes. This very efficient tool allows us to verify the formation of PEPI patterns without breaking the samples for SEM cross-section.

Figure 2.10 shows the angle-resolved PL for two samples made by spin-coating solution PEPI wt 10% and solution PEPI wt 20% on the same structure. Sample with PEPI wt 10% deposited have been characterized under laser excitation at 3.06 eV. Light emission includes the PL of PEPI exciton and different modes in S- and P-polarization (Figure 2.10a,b). In S-polarization, the PL dispersion displays two groups of linear modes and one slow-light mode (marked with white arrows in Figure 2.10a). On the other hand, in P-polarization we observed one group of linear modes and one slow-light mode (marked with white arrows in Figure 2.10b). The observation of these photonic Bloch modes, related to the periodic character of the structure, indicates that PEPI indeed penetrated inside the patterns (Figure 2.10c).

Meanwhile, we observed that the PEPI exciton emission is dominant in the PL dispersion of the sample with PEPI wt 20% deposited (Figure 2.10d,e). Apart from that, the dispersion shows barely visible multimodes on each polarization coming from vertical confinement in the slab and no other distinct modes of patterned PEPI (marked with white arrows in Figure 2.10d,e). We assume that with PEPI wt 20% solution, the concentration is too high to enable a substantial solution infiltrating inside the pattern. As a result, most of the solution is deposited on top of the structure and forms a slab of PEPI (Figure 2.10f).

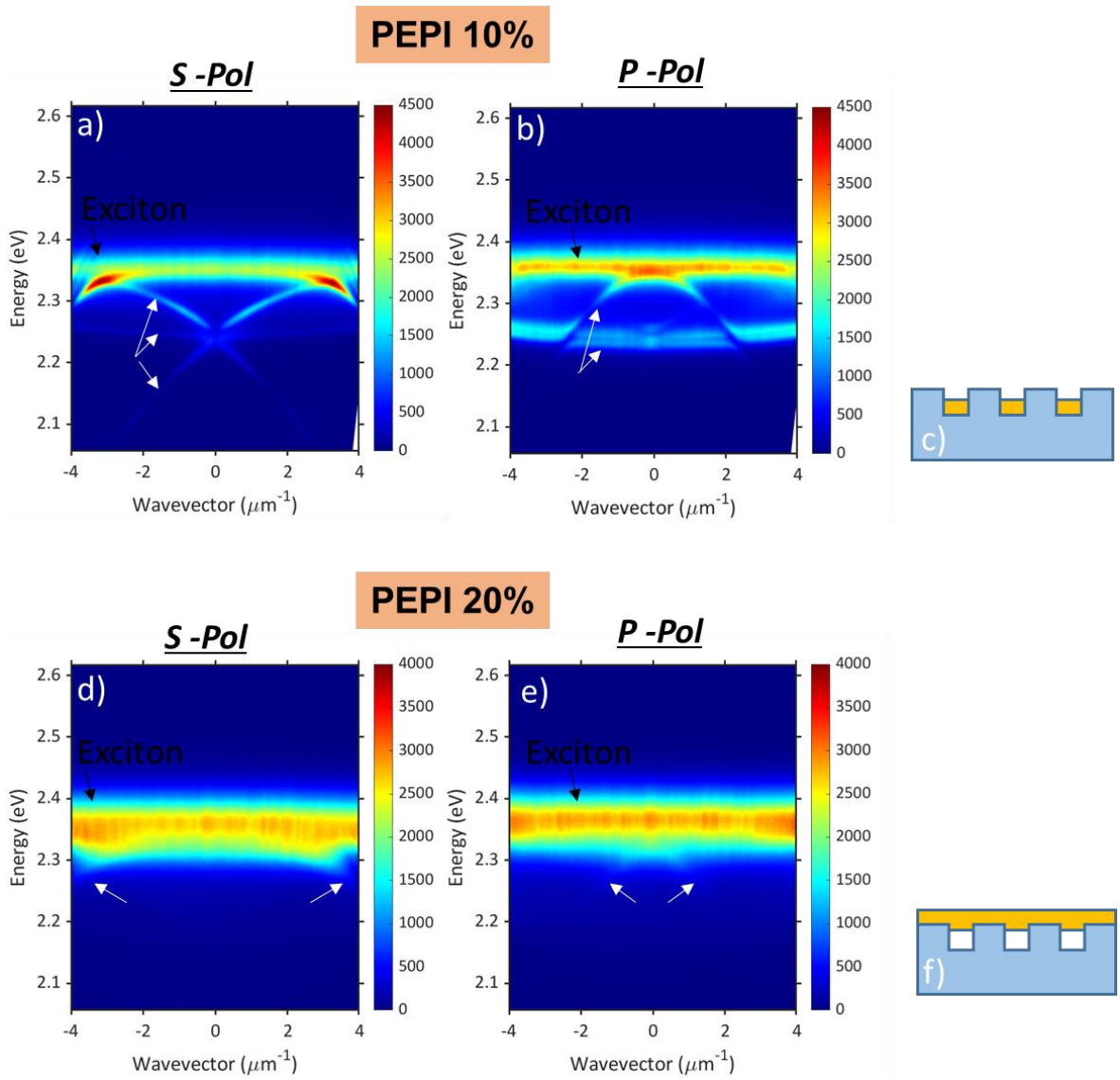

Figure 2.10. Angle resolved PL (along k_x direction) in two polarizations of SiO_2/ Si patterns deposited with PEPI wt 10% (a,b) and PEPI wt 20% (d,e) solutions and the corresponding cross-section structures (c,f). The uncoupled exciton emission are marked with black arrow.

SEM was then used to confirm the hypothesis above and to study the morphology of PEPI (wt 10%) crystallized inside pattern (Figure 2.11). From the SEM cross-section images, we confirm that even though there are still some residues of PEPI on top of the structure, most of PEPI penetrated inside the hole patterns and formed a PEPI metasurface.

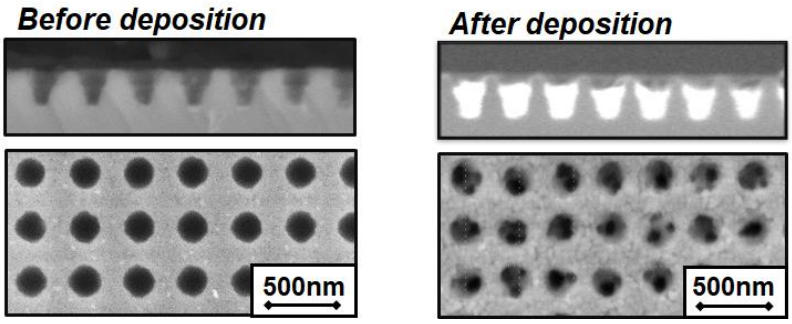

Figure 2.11. SEM top view and cross-section of SiO_2 structure (fabricated by LIL) before and after PEPI deposition.

We can therefore integrate PEPI into different patterns by simply spin-coating PEPI wt 10% solution on top of different lattice backbones. This method is facile and allows to fabricate in parallel multiple PEPI-integrated structures. These structures were further used to study the dispersion engineering of PEPI metasurfaces (Chapter 3).

In order to investigate the crystallographic properties and particular the crystal texture of a PEPI metasurface, we carried an XRD pole figure measurement on such infiltrated patterns and of a PEPI thin film deposited onto a flat substrate for comparison (Figure 2.12). In both samples, the pole figure presents a sharp, narrow distribution of (002) pole intensity. These results indicates that the crystals are highly coherent in orientation and perpendicular to the surface plane, which is consistent with the self-assembly of a multilayered PEPI thin film. We can confirm that PEPI metasurfaces prepared by the infiltration method exhibit good crystal quality with multilayered features.

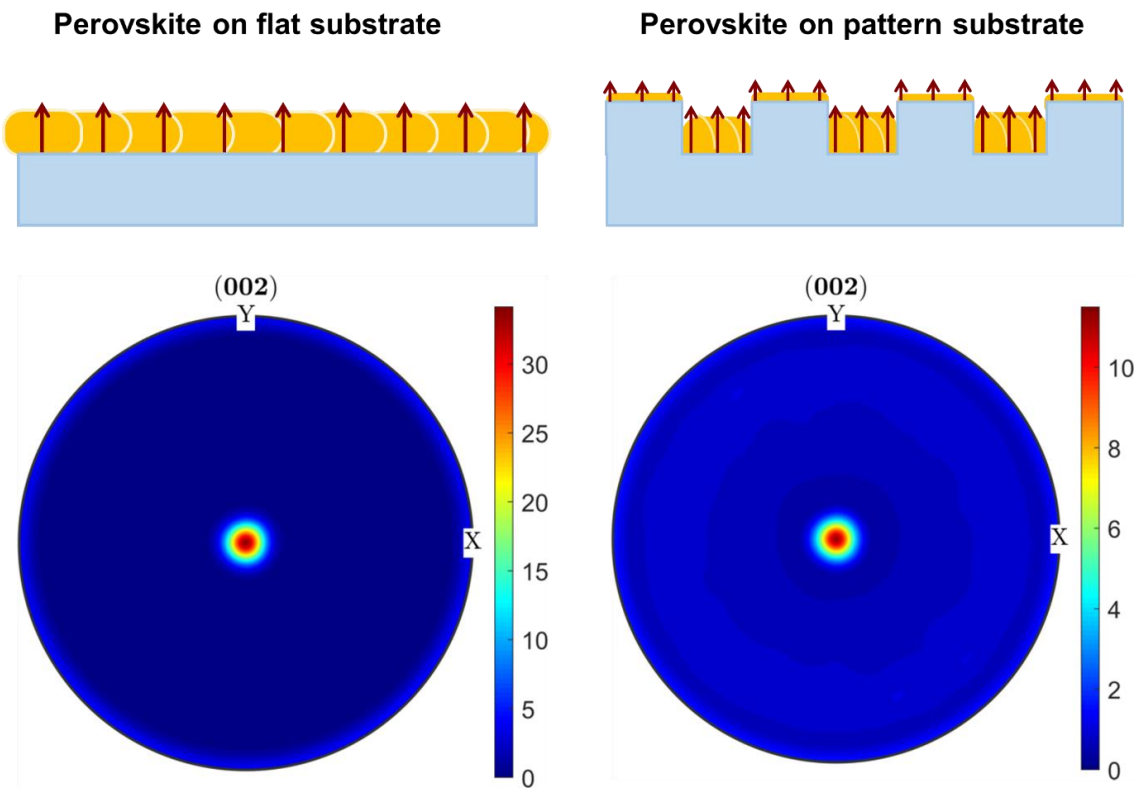

Figure 2.12. Schematic of expected crystal orientation and XRD pole figure of thin film PEPI (wt 10%) deposited on flat substrate and pattern substrate (fabricated by LIL)

Nevertheless, from angle-resolved characterizations we also noticed that the infiltration of PEPI inside the patterns is complex and difficult to control. We conducted numerical simulations employing the Rigorous Coupled Wave Analysis (RCWA) [91] to verify the PEPI thickness integrated inside the hole lattices. PEPI infiltrated inside e-beam lithography patterns had approximately the same thickness with PEPI thin film deposited on flat substrates. On the other hand, PEPI spincoated on top of LIL substrates had uneven thickness, increasing from the center to the edge of the substrates. Figure 2.13 shows the illustration of PEPI infiltration in ebeam lithography substrates and LIL substrates. We assume that the e-beam pattern areas are relatively small compared to the size of the substrates hence the effect of the patterns on PEPI deposition is negligible. On the contrary, LIL substrates have patterns covering almost the whole surface which could have critical impacts on the deposition of PEPI solution.

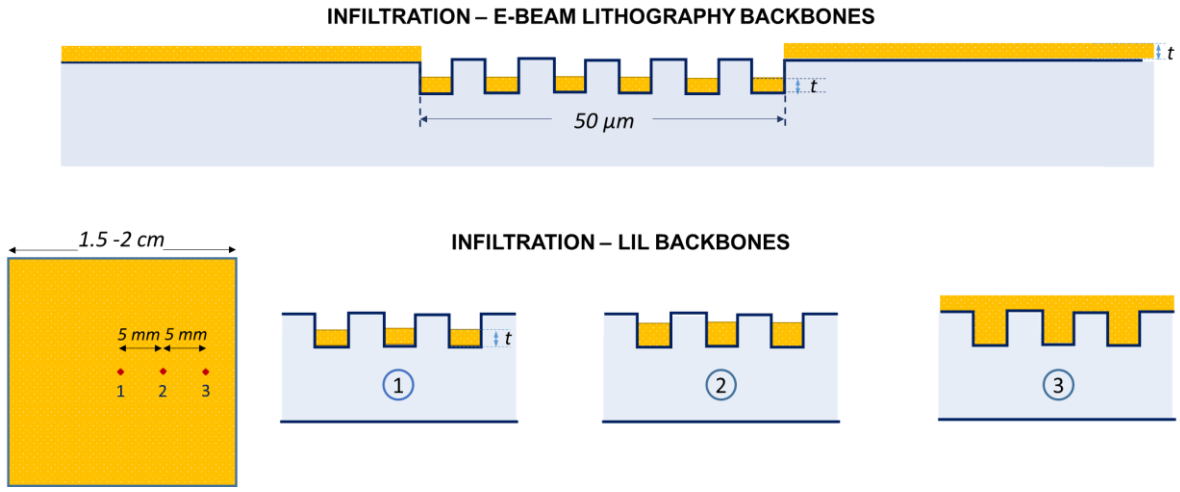

Figure 2.13. Illustration of PEPI infiltration inside patterns fabricated by e-beam lithography and LIL.

Figure 2.14 show the ARPL of PEPI deposited on LIL backbones, measured at two positions (around position 2 and position 3 marked in Figure 2.13). The distance between the two measured positions is 4.63 mm. From the ARPL dispersions, the thickness of PEPI film estimated by RCWA numerical simulations, confirms our prediction of PEPI integrating inside large surface pattern backbones.

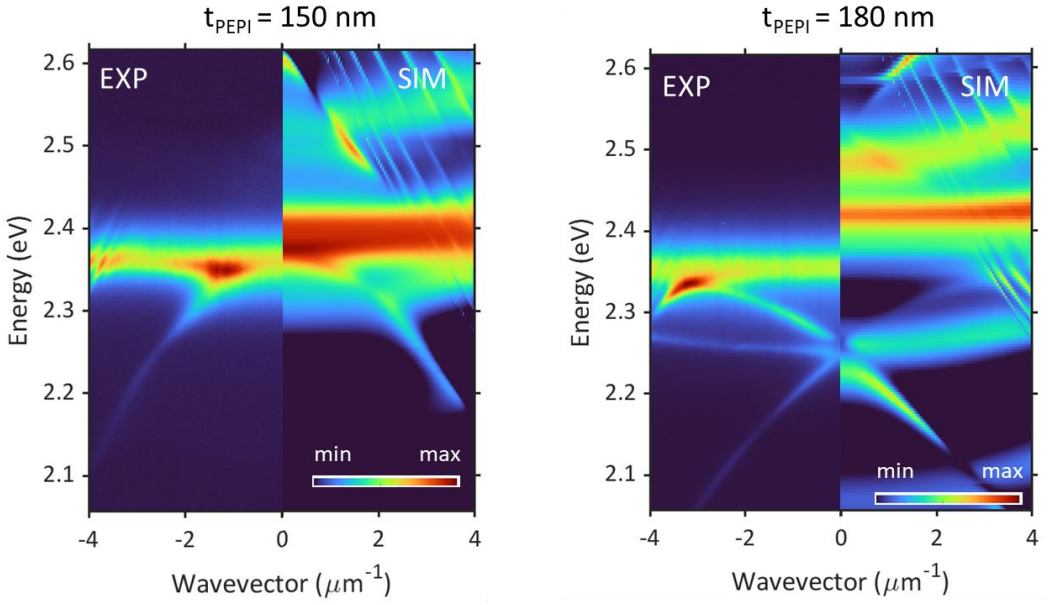

Figure 2.14. Experimental ARPL dispersions and RCWA simulations in absorption of two positions off-center with different characteristics showing estimated PEPI thickness of 150 nm and 180 nm respectively. Sample was prepared by spincoating PEPI wt 10% solution on a large surface hole lattice

(1.5 cm x 1.5 cm), made of 2µm SiO_2/Si backbones by LIL.

2.3 PEPI metasurfaces fabricated by imprinting

2.3.1 Mold preparation

Our Si molds were fabricated using LIL and RIE techniques by Céline Chevalier at Nanolyon/INL, exhibiting homogeneous patterns in the range of mm^2.

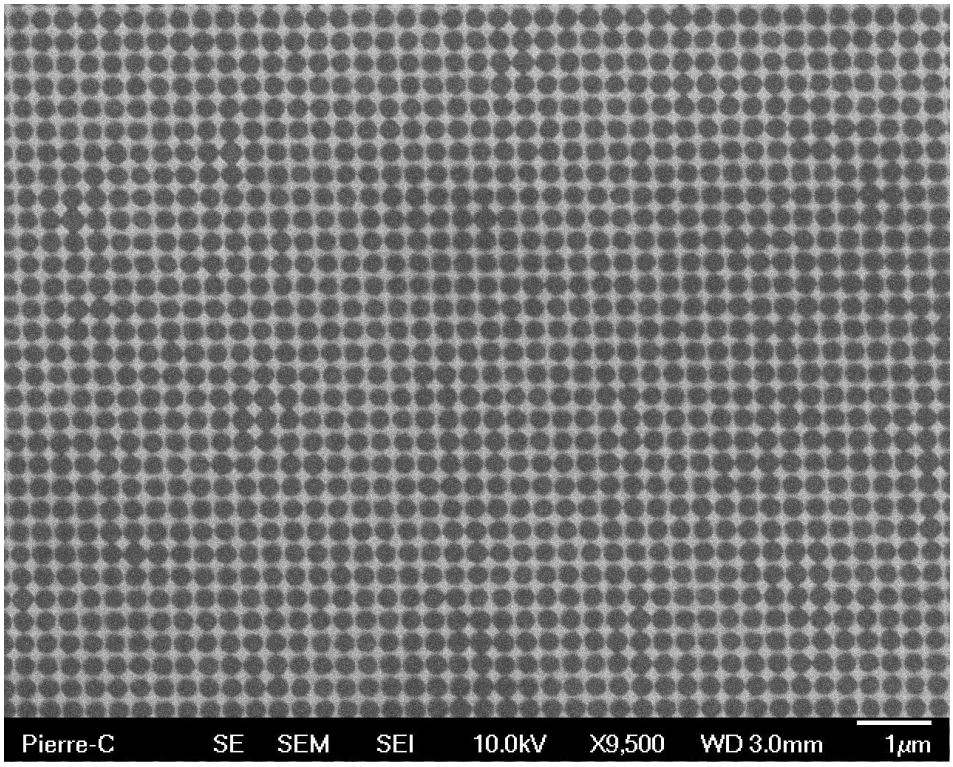

Figure 2.15. Top view SEM fabricated Si molds achieved by LIL and RIE.

Before imprinting, the molds are cleaned by acetone, ethanol, IPA and then the mold surface is functionalized by a silanization process to avoid sticking with perovskite. A solution is prepared by dissolving a few mg of FDDTS (Perfluorododecyltrichlorosilanes – Sigma Aldrich) into 5 ml of n-heptane. The stamps are then left inside this solution for silanization [104,117]. The silanization time for the flat substrate is 10 min, while for the nanostructure stamp, the surface area is larger, requiring longer – at least 30 min. During silanization treatment, the –OH groups bonded to Si particles on the surface of the molds interact with the $–SiCl_3$ groups inside the FDDTS and form a bond Si (surface) – O – Si

(FDDTS) [118]. The mold surface is therefore terminated by silane and its functional organic group, which reduces the surface energy or increase the surface tension [119]. Finally, the mold is cleaned with acetone and baked at 100°C for 20 min. Figure 2.16 shows the significant enhancement of the contact angle between DMF and Si surface with and without silanization.

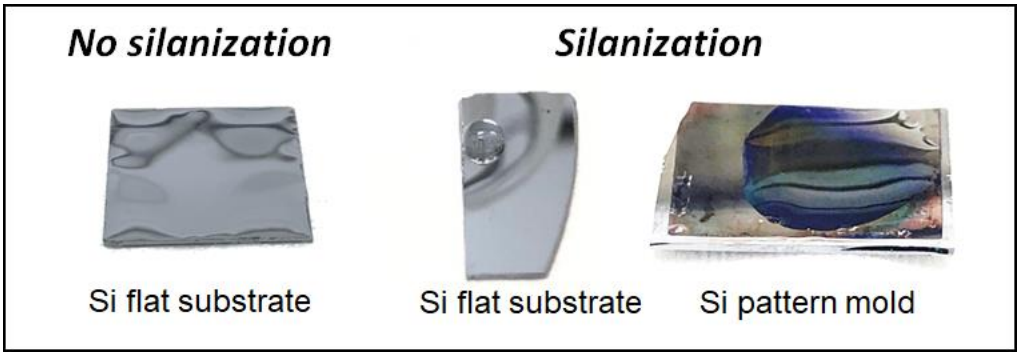

Figure 2.16. DMF solvent dropped on Si substrates: flat substrate without silanization; flat and pattern substrates after silanization.

2.3.2 Fabrication of PEPI metasurface – thermal imprinting

The sketch of the thermal imprinting approach is illustrated in Figure 2.17. Thermal imprinting is a process suited to the structuration of soft materials, in particular perovskites [96,100,104,105]. At first, a thin layer of PEPI is deposited on the substrate by spin-coating PEPI wt 20% DMF solution at 5000 rpm in 30 sec. Then PEPI film is then annealed at 95°C for 90 s to crystallize it before imprinting.

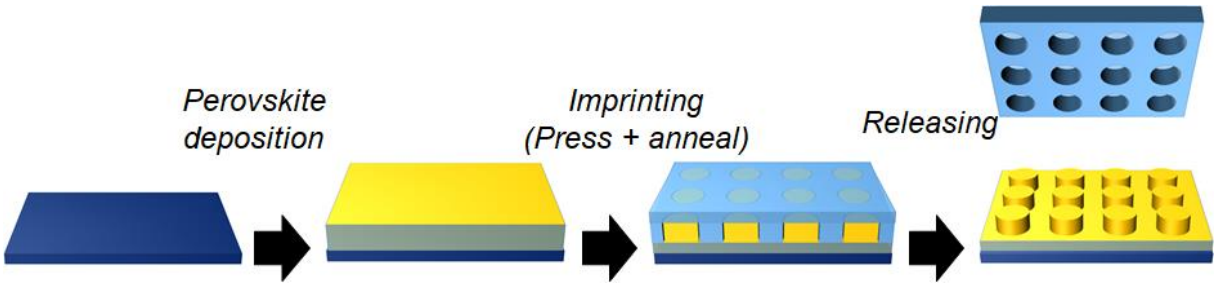

Figure 2.17. Sketch of thermal imprinting technique

At INL, we have used a Rondol press (Figure 2.18) which contains two stainless steel plates integrated with a heating system (up to 300°C for each plate). A water circuit is integrated

to control the temperature. The top plate of the press is fixed and the force is applied by manually lifting the bottom plate toward the top plate. The maximum force achieved by this press is about 100 kN. A sensor is integrated with the press indicating the force value.

Figure 2.18. Photo of the Rondol press available in INL

The imprinting process is operated in ambient atmosphere. This perovskite thin film is next settled between the two plates inside the thermal press. After that, a Si mold with the desired patterns is positioned on top of the PEPI film. The bottom plate is lifted so that the force is gradually increased until it reaches 3 kN (for molds with the size of 1.85 x 1.85 cm^2). Once reaching the pressure, we fix the position of the plate. Then the temperature of the two metal plates in contact with the sample and Si template is set to 100°C. This process takes around 10 min for the temperature to stabilize. The sample and the mold are continually pressed (constant force of 3 kN) and heated (at 100°C) for 15 min. After 15 min, the heat is turned off. We wait for the press to cool down to 35°C, and then release the pressure. The thermal imprint process was adapted from the MAPI perovskite imprint method developed in the frame of Florian Berry's PhD thesis in INL [117].

In order to dampen the mechanical shocks undergone during the nanoimprinting process, we inserted the thermal conductive pad KU-CG 30 (Boyd Corporation) as cushion layers between the press plates and the sample/ mold.

The thermal imprinting method is applicable for different substrates. Here, we deposited and imprinted PEPI perovskite on Quartz substrates and Si substrates covered by a 2 μm SiO_2 layer. The visible diffraction effect observed on the sample surfaces (Figure 2.19) suggested that the imprinting process indeed patterned the thin perovskite layer.

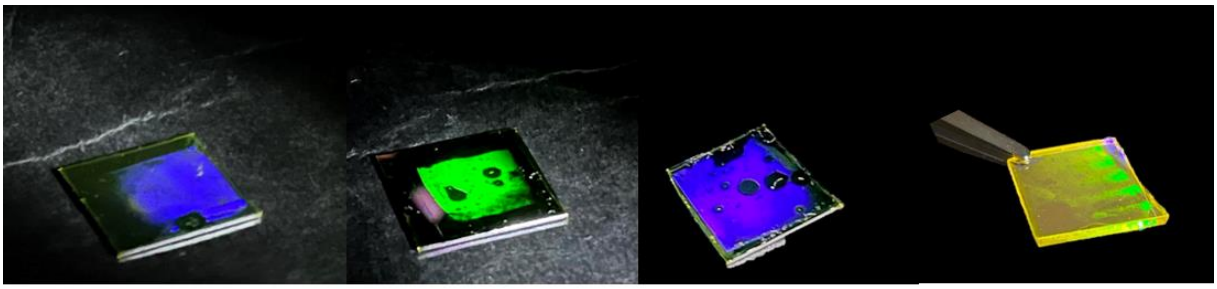

Figure 2.19. Images of PEPI samples (on 2μm SiO_2/Si substrates and quartz substrate) after thermal imprinting using 2D pattern molds (colors variate with the change of period: from left to right samples on SiO_2/Si substrates with period of 300 nm,350 nm, 330 nm; sample on quartz substrate with period 350 nm).

2.3.3 Characterization of imprinted PEPI metasurfaces

SEM characterization is used in order to study the morphology of the imprinted perovskite surface. The SEM image is slightly drift distorted, but it can confirm that the thermal imprinting was successful with patterns transferred into the perovskite layer over hundreds of micrometers (Figure 2.20).

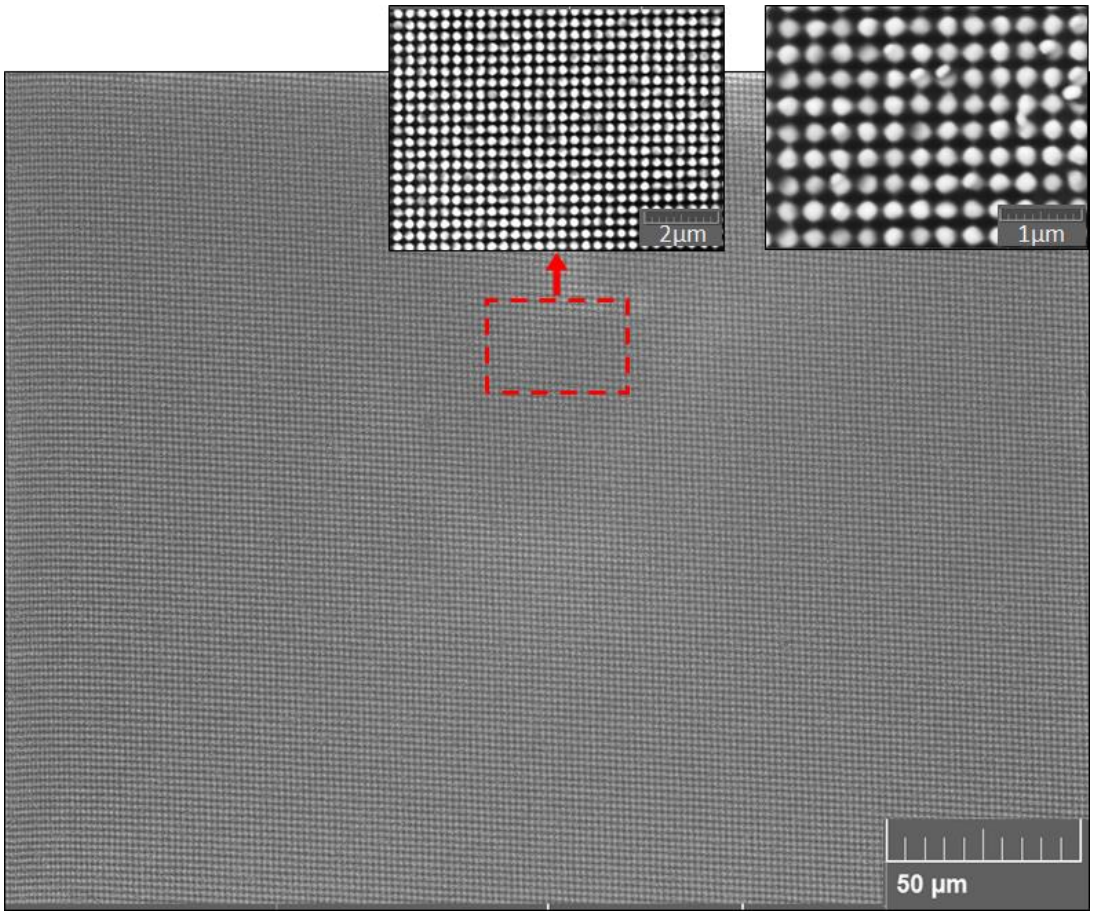

Figure 2.20. SEM image of imprinted PEPI layer. The measured area has dimension of approximately 300 µm x 200 µm.

The SEM images of the Si hole lattice mold and the obtained PEPI pillar lattice metasurface are compared side by side (Figure 2.21). From the SEM characterization, we confirm that the period of fabricated PEPI metasurface is consistent with the period of the original mold.

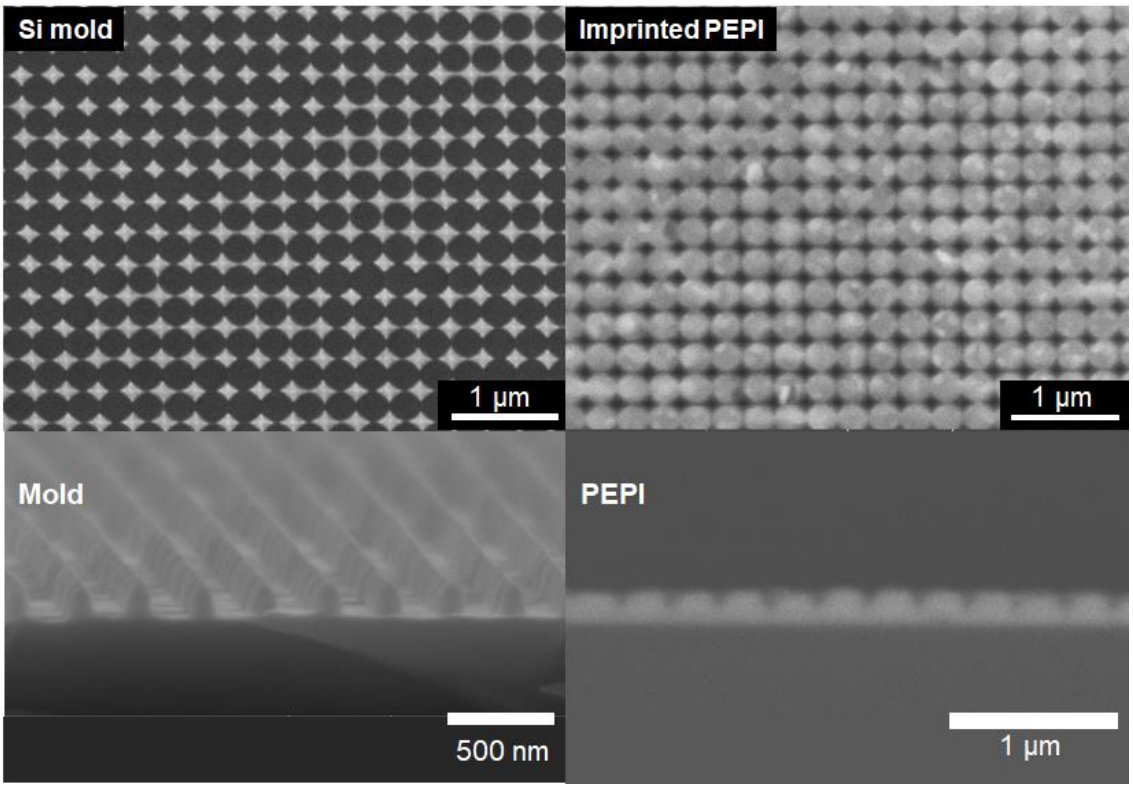

Figure 2.21. SEM images top view (upper panel) and cross-section (lower panel) of 2D Si mold (left) and the imprinted PEPI pattern (right).

We have observed that the pattern size of printed PEPI is smaller than that of the stamp. In particular, we extracted the size distribution histogram from an SEM image of the holes lattice in one mold and the pillar lattice in the corresponding printed sample (Figure 2.22). PEPI pillars' radius is 128 – 148 nm with an average size of 136 nm ± 5 nm. Meanwhile, the holes' radius of the mold is in the range of 136 -155 nm with an average size of 146 nm ± 5 nm. The mean value of the printed pillar radius is therefore 10 nm smaller than the hole radius of the template mold. The size difference indicates that PEPI recrystallized and shrank after the imprinting process.

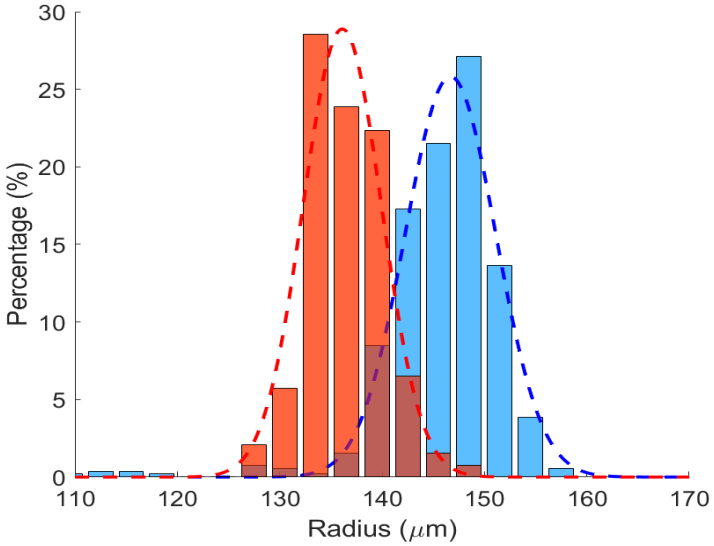

Figure 2.22. Histogram of the radius of holes (Si mold) and of the radius of the pillars (imprinted PEPI) in a 5 µm x 5 µm area.

AFM measurements were conducted to study the profile of imprinted pillar lattices. Figure 2.23 shows the AFM characterization results of the PEPI metasurface prepared by pressing a mold 200 nm in-depth with a force of 3-4 kN. As can be seen from the AFM profile, the PEPI patterns depth is around 80nm, while the total thickness of the PEPI layer is 150 nm. We therefore noticed that with our method, we could not achieve fully patterned PEPI film and could only obtain partially imprinted PEPI film. In an attempt to increase the pattern depth, a more robust force was applied in the imprinting process. However, the substrates were cracked and damaged with a pressing force reaching 5 kN.

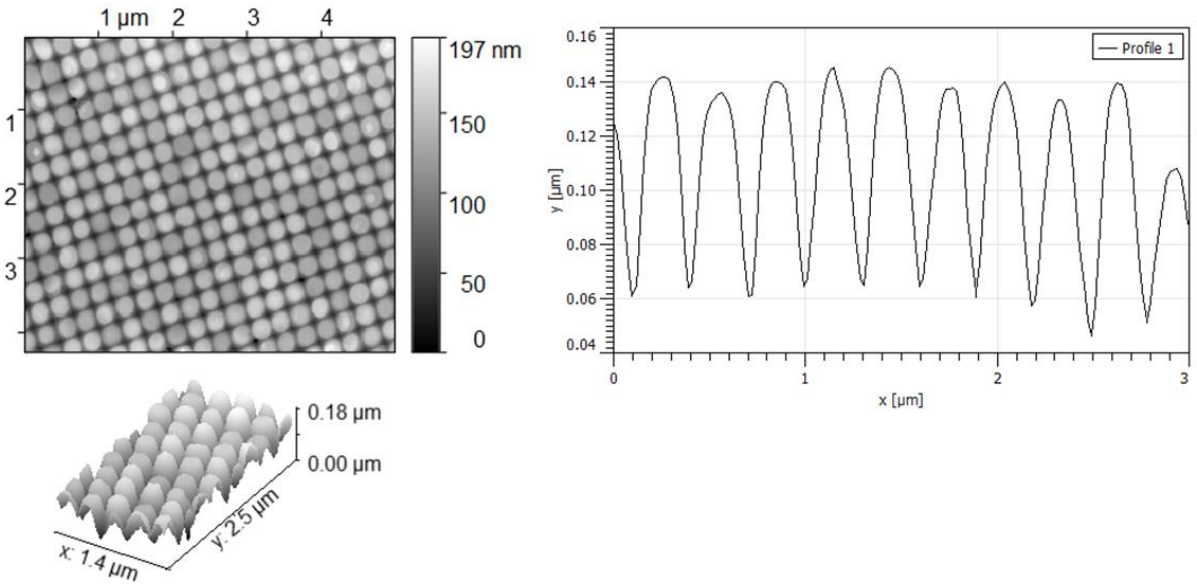

Figure 2.23. AFM 2D, 3D image, and profile of PEPI metasurface prepared by imprinting thin film PEPI with 3-4 kN force.

From the SEM characterization shown before (Figure 2.20), we observed that the PEPI metasurface prepared by the imprinting method is homogeneous over a large scale (hundreds of micrometers). In order to verify the homogeneity of patterned PEPI, we performed ARPL characterization showing optical dispersions measured in different positions of one imprinted sample. The substrate holder is attached to two piezoelectric motors (x-y directions), allowing us to move and measure different spots on the sample precisely.

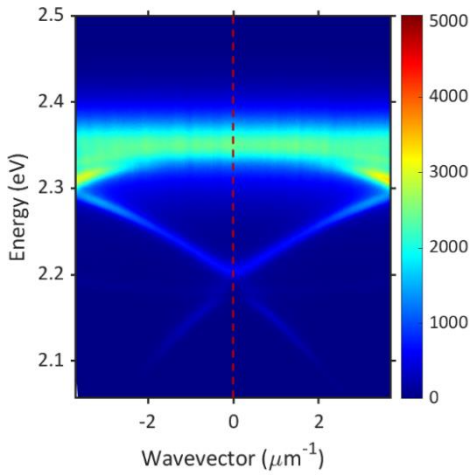

Figure 2.24 ARPL dispersion measured in imprinted PEPI metasurface. The red dash line marks the extracted data used to compare dispersions measured in different positions.

Figure 2.24 shows a typical ARPL dispersion measured in one position of imprinted PEPI film. For simplification, we compared and extracted only the energy peak, linewidth at wavevector k=0 μm^{-1} (marked as the red-dash line in Figure 2.24) of the ARPL dispersions.

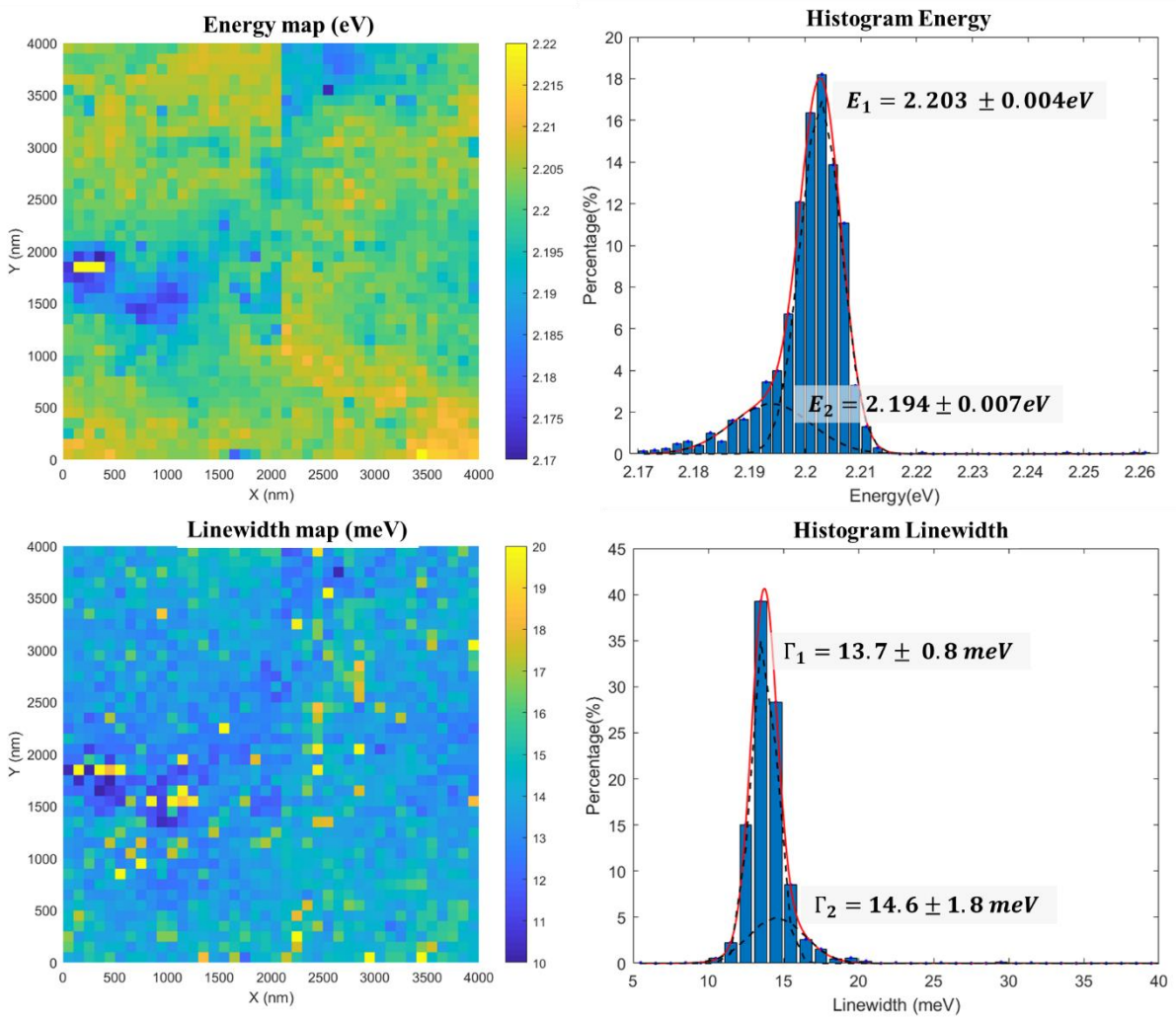

Figure 2.25. Spatial-resolved energy, linewidth map and distribution of energy peaks, linewidths measuring in 4000 x 4000 nm area on imprinted PEPI metasurface

We conducted the ARPL measurements scanning in an area of 4 mm x 4 mm on the PEPI metasurface sample. Each characterized position has the closest distance of 100 μm away from each other in either x or y directions. By collecting the data from all measurements, we constructed the spatial-resolved energy map and the spatial-resolved linewidth map (Figure 2.25). In these maps, each pixel has the position (x,y) related to the spatial position of the

measurement point on the sample and the intensity corresponding to extracted energy peak/ linewidth. The energy peaks give information on the uniformity of the imprinted pillar patterns in terms of lattice parameters such as period, size, and height of the pillars. Meanwhile, the linewidths are related to the quality of the fabricated metasurface.

The distributions show no significant shift in energy peaks and overall close values of linewidths. The energy peaks are mainly distributed in the range of 2.19 - 2.21 eV with a mean value of around 2.2 eV and a relatively small standard deviation (a few meV). Similarly, the measured linewidths of dispersions are in the range of 12-15 meV with a mean value of around 14 meV. It is worth noting that these are not the best values of the linewidths which we have achieved because the employed mold had been repeatedly used for several imprinting cycles. The dispersion linewidths can therefore be improved by enhancing the quality of the templates. Nevertheless, the quality of the imprinted patterns is consistent within a large surface. These results confirmed the homogeneity of imprinted metasurface over a wide area of a few millimeters range.

2.3.4. Reproducibility of imprinting

The reproducibility of thermal imprinting is investigated using SEM characterization. The patterned templates are cleaned after imprinting and reused for the next fabrication. Indeed, we notice that the thermal imprinting method is highly reproducible. The SEM images indicate no crucial difference in lattice parameters between samples prepared under the same conditions (Figure 2.26).

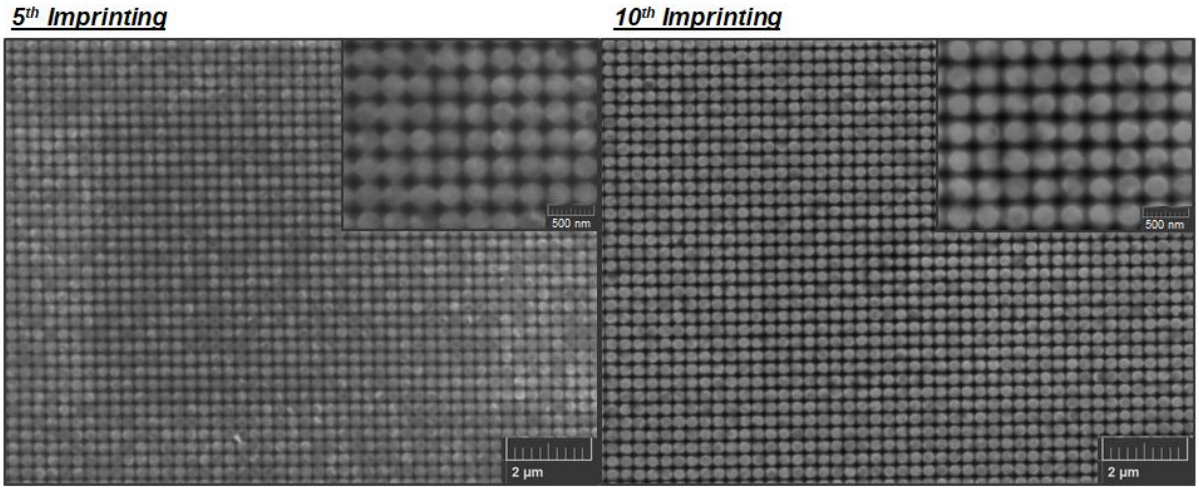

Figure 2.26. SEM images of imprinted PEPI samples prepared with similar fabricating conditions using the same patterned molds.

Nevertheless, we note that the molds still have a limited recycle lifetime depending on the fabrication conditions (i.e., surface treatment, pressing force, etc.). Figure 2.27 exhibits SEM views of a damaged molds after 10 imprinting cycles. As shown in the SEM images, some patterns were dislocated on the mold, which could be induced by an ineffective silanization treatment.

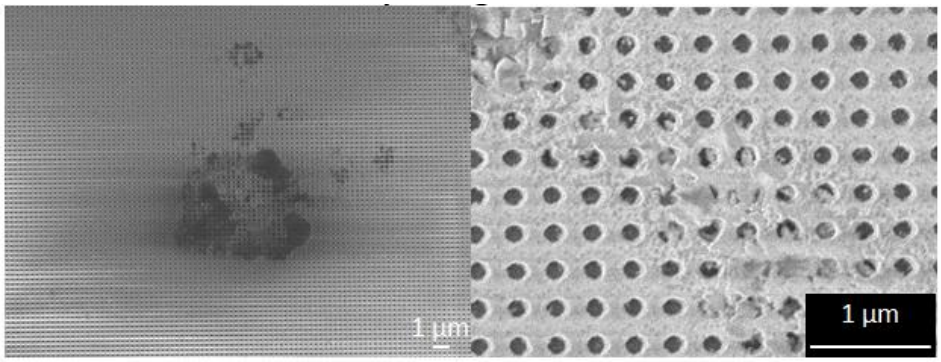

Figure 2.27.SEM images of mold before imprinting and damages after 10 imprinting sequences

2.4. Conclusion of the chapter

This chapter introduces the two methods we have developed in order to deposit PEPI thin films and fabricate 2D lattice PEPI metasurfaces. Our first approach to pattern PEPI was to infiltrate it inside pre-patterned backbones via simple spin-coating. SEM and optical characterization were carried out and confirmed the formation of the PEPI pillar lattice. Though there is still a limitation due to the low infiltration control, affecting the small-scale homogeneity. However, this infiltration method is highly flexible, easy to perform, and suits our objective of investigating different designs. PEPI metasurfaces fabricated by infiltration method were further studied to demonstrate the dispersion engineering of exciton-polaritons. These results will be discussed in the following chapters (3 and 4).

To improve the surface homogeneity, we developed the thermal imprinting process for PEPI metasurface fabrication. The properties of the imprinted metasurface were evaluated by SEM, AFM, and optical characterization. PEPI 2D lattice metasurfaces were fabricated, exhibiting homogeneous surfaces over a few mm range on a large scale. Such high-quality, low-cost, large-area metasurfaces are highly promising for device manufacturing. In this thesis, PEPI imprinted metasurfaces were designed and fabricated, hosting ballistic propagation of exciton-polaritons. The study on exciton-polariton propagation will be presented in Chapter 5.

CHAPTER 3

TAILORING DISPERSION OF EXCITON POLARITON WITH PEROVSKITE METASURFACE

Along with the expanding research on exciton-polaritons, the study of polariton dispersion engineering is essential for both fundamental physics and prototype polariton-based optoelectronic devices. For example, engineering ultra-fast polaritons is a key for realization of polaritonic signal transmission and logistic devices with low energy consumption and outstanding processing speed. Polaritons' flow is controlled, shaped and guided by the modulation of polariton confinement. Trapping polariton can be achieved in a potential landscape created by spatial photonic confinement.

In this chapter, we demonstrate the dispersion engineering of room temperature exciton-polaritons via PEPI excitonic metasurfaces. Here, the fabrication of PEPI metasurface is done by infiltrating PEPI solution inside low refractive index backbone (Chapter 2.2), forming a periodically nanostructured metasurface. We will show the potentialities of this approach to tailor on demand the dispersion of exciton-polaritons. The effect of geometrical parameters of the metasurface is a key to engineer polariton with different dispersions (linear, slow light, multi-valley).

3.1. Simulation of photonic dispersion engineering

We recall the structure of PEPI 2D lattice metasurface in Figure 3.1. In this design, PEPI is integrated completely inside a nano-hole-lattice made of low refractive index backbone SiO_2 and creates an inverse nano-pillar-lattice of high refractive index ($n_{PEPI} = 2.4$). This perovskite metasurface is then encapsulated by a film of PMMA functioning as protection from humidity and oxidation. It is noted that the refractive index of PMMA (1.49) is closely matched with the

SiO_2 one (1.47) in the whole spectral range of interest (400-600 nm). Therefore, from the photonic point of view, the PMMA/ PEPI nano-pillars/ SiO_2 stack is equivalent to PEPI nano-pillars standing in a homogeneous optical medium. As a result, photonic modes of the structures are mainly determined by PEPI lattice parameters: period a, filling factor (*FF*) here defined as aspect ratio of diameter of PEPI pillars over period d/a, and thickness of PEPI $t_{PEPI.}$

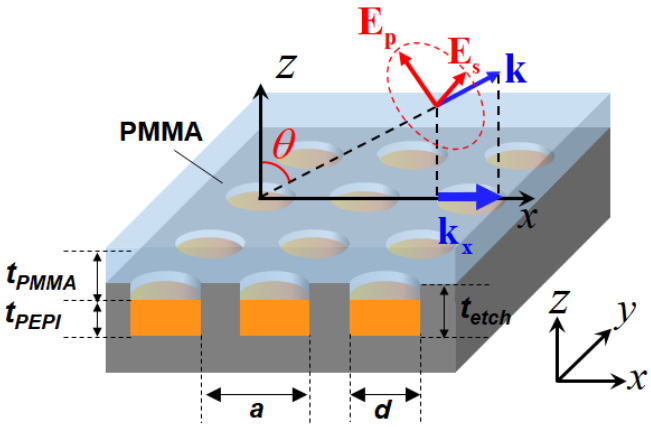

Figure 3.1 Sample structure

Different parameters of a (250 nm - 350 nm), *FF* (0.6-0.9), and t_{PEPI} (50 nm - 80 nm) were studied in order to reveal their effects on the created polariton dispersion. Numerical simulations employing the RCWA were performed to predict the photonic Bloch modes of 2D PEPI metasurfaces response as a function of energy and wave vector. The RCWA simulations of angular-resolved reflectivity and absorption have been done with S_4, a software provided by Fan Group in the Stanford Electrical Engineering Department [91]. To demonstrate only the photonic dispersion without coupling with PEPI exciton, we conduct a simulation of passive structure in which PEPI is alternated by a dielectric medium of refractive index n = 2.4. For each structure, we simulate the angular-resolved reflectivity along ΓX direction of reciprocal space and in two distinct polarizations. The S-polarization corresponds to non-zero E_y electric field component. The P-polarization corresponds to non-zero H_y magnetic field component.

3.1.1 Effect of lattice period

Structures possess periods in the range of 250 nm to 350 nm were studied interpreting the detuning effect of lattice period. Figure 3.2 show the comparison of photonic dispersion in two structures with a =250 nm and a =350 nm. The simulated angle resolved reflectivity results show the same dispersion curves for a given polarization (S or P), but shifted significantly in term of energy. In S-polarization, structure with period a = 250 nm (left panel) exhibits one linear mode while structure with period a = 350 nm (right panel) has on linear mode and one multi-valley mode within the vicinity of PEPI exciton. Hence, the expected polaritons resulting from the strong coupling between these photonic modes and PEPI exciton would have completely different characteristics. In P – polarization, the photonic mode of structure a = 250 nm is distant from the exciton, though it is expected to not couple in strong coupling regime with PEPI excitons. In brief, by tuning the period of the structure, we can select which photonic mode to couple with exciton and therefore, control the emerged polaritonic dispersion.

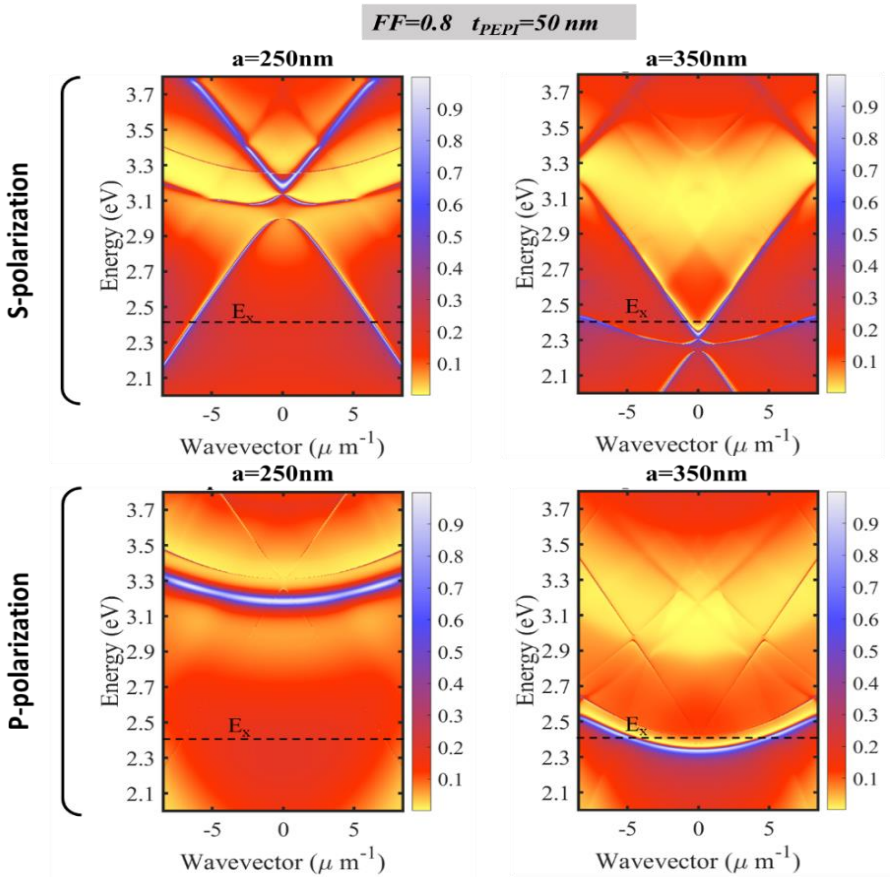

Figure 3.2 Numerical simulation of the passive structure of PEPI 2D lattice metasurfaces for different lattice periods with fixed FF=0.8, t_{PEPI} = 50nm. Black dash lines represent position of exciton energy.

3.1.2. Effect of filling factor

To study the effects of filling factor on photonic dispersion, we perform the numerical simulations scanning values of *FF* from 0.6 to 0.9. As the values of *FF* increased, we observed photonic dispersions with larger negative detuning and slightly larger bandgap (Figure 3.3). There is a switch in dark and bright modes (located in the two highest energy), suggesting the occurrence of band inversion takes place at around *FF*=0.6-0.7. Tuning the *FF* gives a chance to engineer the band gap of Bloch resonances and also offers possibility to obtain extra ordinary features like exceptional points with an enhancement of local density of states or BIC – localized state with no loss in the radiative continuum (further discussed in chapter 4) with exciton polariton. This effect had been theoretically demonstrated by L.Lu et al. in a previous report [94].

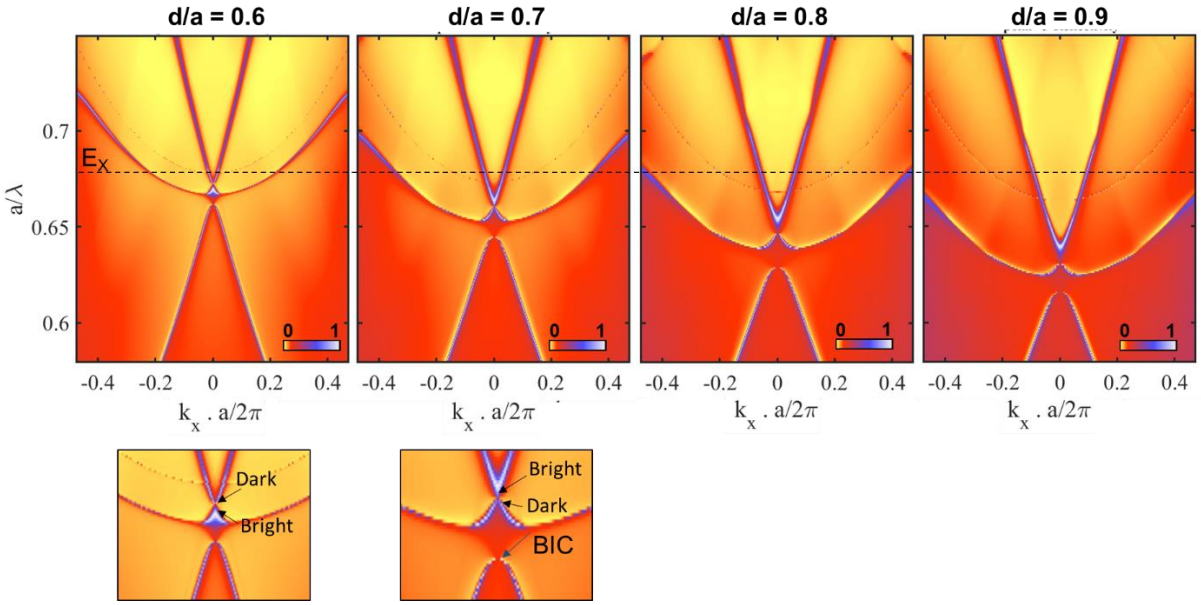

Figure 3.3. Numerical simulation of the active structure of PEPI 2D lattice metasurfaces in S-polarization for different FF values with fixed period a = 350 nm and PEPI thickness t_{PEPI} = 50 nm. Black dash lines represent position of PEPI exciton.

3.1.3. Effect of PEPI thickness

Similarly, ARR of passive structure were simulated using RCWA method in order to study the effects of PEPI thickness on polariton dispersion (see Figure 3.4). We studied structures with similar values of lattice period and aspect ratio (350 nm and 0.8 respectively). Meanwhile, the heights of PEPI pillars are varied from 50 nm to 80 nm (expected variable thickness from the fabrication condition).

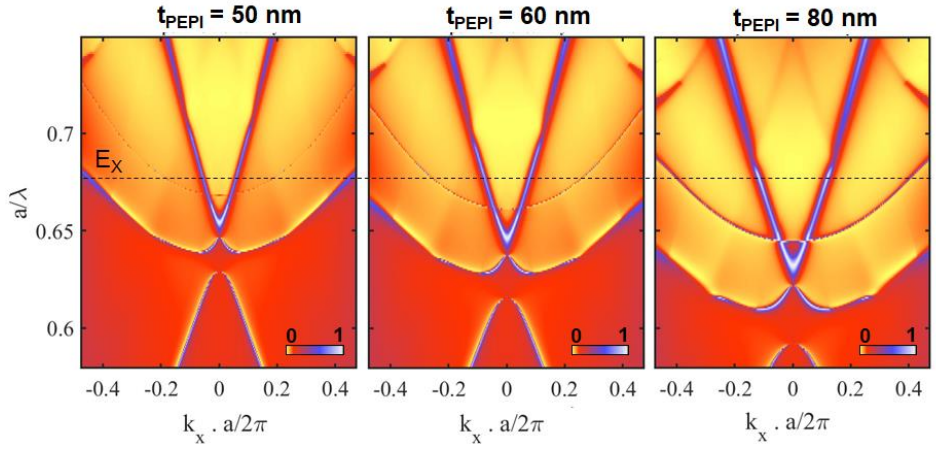

Figure 3.4 Numerical simulation of the passive structure of PEPI 2D lattice metasurfaces for different values of PEPI thickness with fixed period a = 350 nm and d/a = 0.8 (excited by S-polarized light).

From the simulation results, in the scanning range of PEPI thickness, there is no significant change in properties of photonic dispersions. The bandgap and the detuning values increase as the thickness of perovskite increases.

3.1.4. Final sample design

Finally, two designs of PEPI metasurfaces are chosen in our study (see table 3.1): 1/ Structure A: 80 nm-height pillar-lattice with a filling factor of 0.8 and a lattice parameter of 250 nm; 2/ Structure B: 50 nm-height pillar-lattice with a filling factor of 0.9 and a lattice parameter of 350 nm. These designs provide a rich variety of photonic Bloch modes and mode dispersions in the vicinity of PEPI exciton energy. Structure A displays a single S-polarized mode with an

almost linear dispersion. Structure B shows a P-polarized mode with an almost parabolic dispersion, and three S-polarized modes, two of which exhibit parabolic dispersions with opposite and small curvatures corresponding to a mini-gap opening, while the third one appears an exotic mode with a multi-valley dispersion of W-shape with two off-Γ minima.

Structure	a (nm)	FF	t_{PEPI} (nm)	t_{etch} (nm)	t_{PMMA} (nm)
A	250	0.8	80	150	200
B	350	0.9	50	150	200

Table 3.1. Design parameters

3.2 Demonstration of exciton polariton dispersion engineering

The strong coupling regime in these PEPI metasurfaces is characterized by angle-resolved reflectivity (ARR) and angle-resolved PL (ARPL) measurements through a Fourier spectroscopy set up. These angular-resolved experiments are performed along ΓX direction of reciprocal space, using two polarizations: the S-polarization and the P-polarization. Numerical simulations employing RCWA presenting calculated ARR and angle-resolved absorption were performed in order to be in direct comparison with the experimental measurements.

A quantum theory of radiation matter coupling is used to analyze the strong coupling mechanism in periodically textured excitonic metasurfaces. This theory takes into account the in-plane periodicity of photonic modes and excitonic wave functions on an equal footing. The full Hopfield matrix can be obtained from a classical solution of Maxwell equations in such periodically patterned multilayer structure, and solving for the corresponding Schrödinger equation for the exciton envelope function, then coupling them to obtain the coupling matrix elements [43]. Here, we approximate the excitonic response as if it was concentrated in a single quantum well layer at the center of the periodically patterned region, with an effective oscillator

strength taking into account the finite thicknesss of the 2D PEPI film. Polaritonic modes are obtained by numerically diagonalizing the Hopfield matrix. The analytical model was calculated by Dario Gerace from Pavia University in the frame work of a collaboration [43].

3.2.1 Linear dispersion

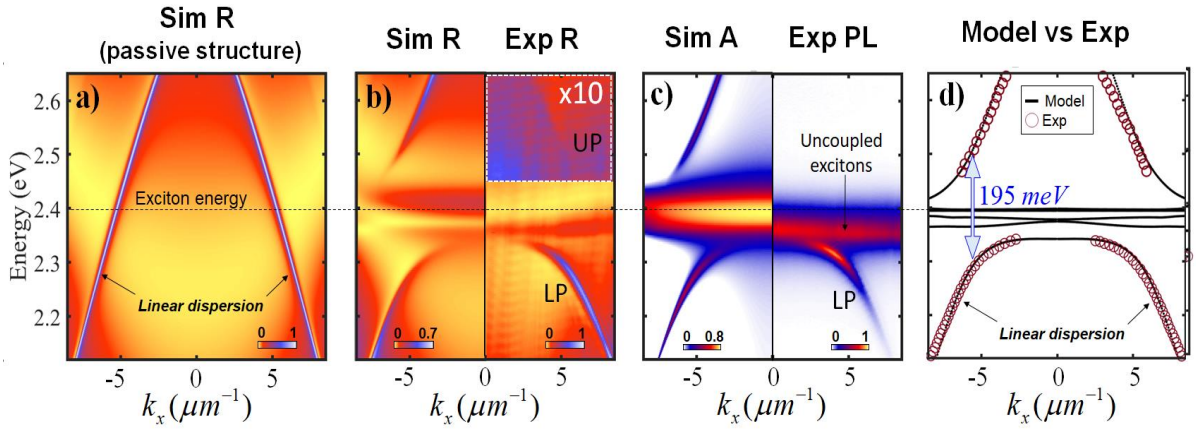

Figure 3.5. Structure A, S-polarization (a) Numerical simulations of the ARR for the passive structures. (b) Experimental results (right panel) and numerical simulations (left panel) of the ARR spectra for the active structures. (c) Experimental results of the ARPL response (right panel) compared to numerical simulations of the angular-resolved absorption by RCWA (left panel) for the active structures. (d) Numerical solution of photonic crystal polariton dispersions from a quantum model of radiation-matter interaction, compared to experimental results extracted from ARR measurements. The black dash line represents the energy of the PEPI excitonic resonance.

Within the measurement range, structure A exhibits a single linear S-polarized photonic dispersion shown as the simulated reflectivity of passive structure Figure 3.5a. The coupling between this Bloch mode with PEPI excitons is first revealed by reflectivity measurements. Figures 3.5b present the ARR experimental results (right panels) directly compared to the numerical simulations (left panels) performed on the active structures. From this result, the strong coupling regime induced by the presence of the strong excitonic response is clearly evidenced: the dispersion curve is bent when approaching the exciton energy, and undergo the typical anticrossing behavior as a function of the in-plane wave vector (scanned through the

incidence angle). The dispersion splits into an upper polariton (UP) and a lower polariton (LP) branch, respectively, with a good overall agreement between measurements and numerical simulations (Figure 3.5b).

Although the reflectivity experiment proves the existence of photonic crystal polaritonic modes in these PEPI metasurfaces, it is important to demonstrate that polariton states can be populated in these structures via optical pumping. Figure 3.5c presents the ARPL experimental results (right panels) performed on the active structures. To get a qualitative comparison, simulations of angle-resolved absorption are also presented on equivalent color scale plots (left panels). Below the bare exciton, the LP emission is clearly observed in these PL measurements, confirming the existence of polariton states in our samples. Typical to other room temperature polaritonic systems using high bandgap materials, the UP is not observed in PL measurements [120,121]. Regarding the signal from a non-dispersive band corresponding to uncoupled PEPI excitons, which is evident both from PL measurements and absorption simulations with a small spectral shift corresponding to the Stokes-shift, we notice that depending on the location within the PEPI pillar, an exciton can be at an anti-node or a node position of the photonic mode, thus can undergo strong coupling or weak coupling with these modes. This is different from text-book exciton quantum well polaritons, where all the excitons are equally coupled to the same Fabry-Perot mode [122].

The polaritonic modes calculated from the quatum model are presented in Figure 3.5d. Correspondingly, the experimental data extracted from the ARR measurements are also superimposed, showing a remarkably good agreement over the whole parameters range. The theoretical Rabi splitting energy is 195 meV.

From either experimental and simulation results, it is noticeable that the obtained polaritons have almost linear features similarly with the original uncoupled photons. We extracted the group velocity (normalized to the speed of light ($c=3.10^8$ m/s), $|v_g|/c$ from

experimental data and calculations of polariton dispersions from Hopfield matrix diagonalization. Linear dispersion in LP corresponds to $|v_g|/c \approx 0.42$ when $|k_x|$ exceeds 5 μm^{-1}. This linear polaritonic dispersion is similar to the one of guided polaritons recently reported from several groups [123,124]. Such high velocity regime is perfectly adapted to study the ballistic propagation of polaritons for transmitting information and gating signals between polaritonic devices [125].

3.2.2. Slow-light dispersion

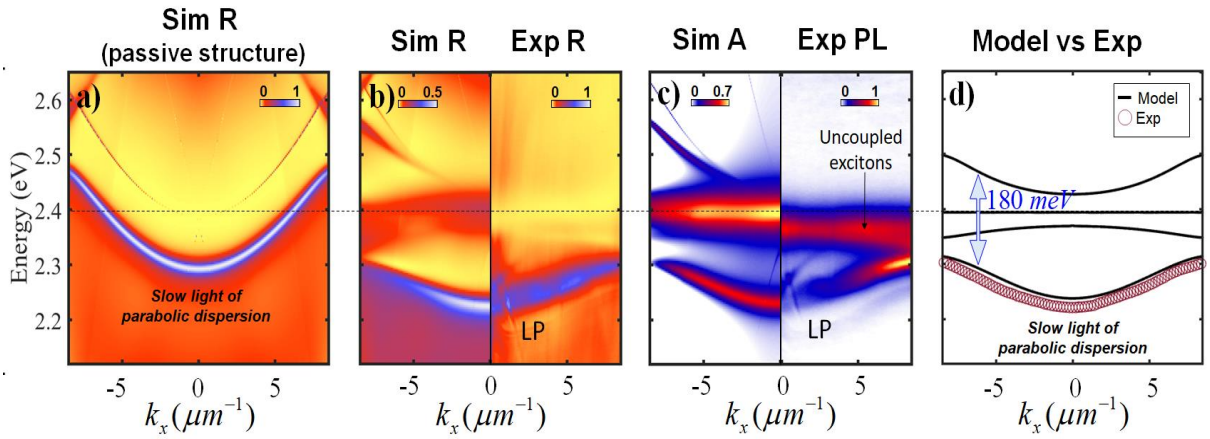

Figure 3.6. Structure B, P-polarization (a) Numerical simulations of the ARR for the passive structures. (b) Experimental results (right panel) and numerical simulations (left panel) of the ARR spectra for the active structures. (c) Experimental results of the ARPL response (right panel) compared to numerical simulations of the angular-resolved absorption by RCWA (left panel) for the active structures. (d) Numerical solution of photonic crystal polariton dispersions from a quantum model of radiation-matter interaction, compared to experimental results extracted from ARR measurements. The black dash line represents the energy of the PEPI excitonic resonance.

The strong coupling between the P-polarized photonic dispersion of structure B and PEPI exciton is revealed through characterization. The uncoupled photonic mode displays an almost parabolic curvature (Figure 3.6a). Under strong coupling with PEPI robust exciton, this photonic mode split into two polaritonic modes: an UP curvature exhibits low intensity, and a LP branch has parabolic dispersion close to normal incidence (shown by simulated ARR Figure

3.6b left panel). ARR measurement result is consistent with the numerical simulation (Figure 3.6b right panel) shown dispersion bent in surrounding of exciton resonance (2.4 eV). This anticrossing behavior which is the signature of strong coupling, confirmed the presence of generated polaritonic modes in the system.

We note that the PEPI model used for numerical simulations only takes into account the excitonic resonance, but not the highly absorptive continuum states above the PEPI bandgap (see section 2.1). This also explains the much weaker measured signal of UP as compared to the simulated one (Fig 3.5b). In the P-polarized measurement results of structure B (Fig 3.6b), the UP is not visible. This is also in agreement with the related simulations in the left panel, in which the simulated signal of this UP is already very weak.

Via optical pump, exciton-polariton states are populated exhibiting in ARPL signal (Figure 3.6c). Similarly with the previous structure, in PL measurements, the UP branch is not observed, and there is an emission of the uncoupled exciton. The spectral mismatch observed in uncoupled exciton between absorption simulation, and ARPL signal is due to Stokes-shift. Though the intensity distribution is different as absorption calculation do not take into account the relaxation mechanism in experimental PL. Overall, both the PL measurement and absorption simulation are in agreement demonstrating a slow light LP mode.

The elementary quantum theory emulates effectively polaritonic mode observed from ARR measurement (Figure 3.6d). The Rabi splitting is estimated at approximately 180 meV.

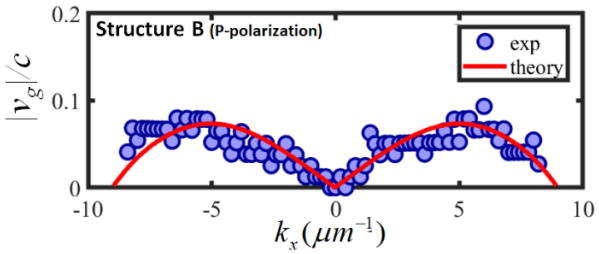

Figure 3.7. Group velocity extracted from ARR measurement of P-polarized mode in structure B.

Figure 3.7 presents the normalized $|v_g|/c$ corresponding to P-polarized LP in the structure B. Contrary to the previous case, here polaritons undergo a slow-light regime with a maximum of $|v_g|/c \approx 0.08$ corresponding to the inflexion points of the dispersion at $|k_x| \approx 5\ \mu m^{-1}$. We further notice that this behavior is quite similar to microcavity polariton dispersion. Such slow-light regime, exhibiting high density of states, would be well suited to study polaritonic non-linear effects, as well as to trigger the Bose-Einstein condensation of polaritons.

3.2.3. Multi-valley dispersion

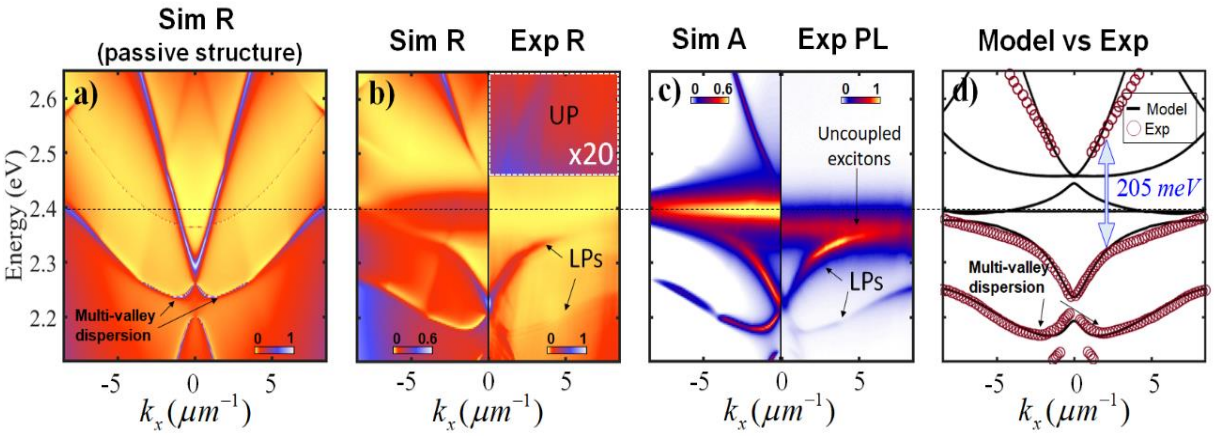

Figure 3.8. (a) Numerical simulations of the ARR for the passive structures. (b) Experimental results (right panel) and numerical simulations (left panel) of the ARR spectra for the active structures. (c) Experimental results of the ARPL response (right panel) compared to numerical simulations of the angular-resolved absorption by RCWA (left panel) for the active structures. (d) Numerical solution of photonic crystal polariton dispersions from a quantum model of radiation-matter interaction, compared to experimental results extracted from ARR measurements. The black dash line represents the energy of the PEPI excitonic resonance.

In the measurement range, structure B shows three S-polarized photonic modes: two curvatures with opposite group velocity and one multi-valley dispersion (Figure 3.8a). The light-matter interaction between S-polarized photonic modes and exciton in PEPI metasurfaces in structure B is revealed through ARR simulation and measurement. Figure 3.8b notes that there are two photonic modes strongly coupled with PEPI exciton resulting two LP branches

and two UP branches. The first curvature photonic mode is strongly coupled with exciton energy resulting to an UP state at energy above exciton that can be observed in both ARR simulation and measurement (Figure 3.8b), and a LP state with curvature anti-crossed excitonic resonance, starts to bend (along k_x) at $|k_x| \approx 2\ \mu m^{-1}$. The second photonic mode that is strongly coupled with exciton has two minima or multi-valley shape. The second UP state has relatively weak intensity though it is only visible in ARR simulation. The resulted LP state starts to bend at $|k_x| \approx 8\ \mu m^{-1}$, and shares the same multi-valley shape as the corresponding photonic mode. Through ARPL measurement, the two LP modes are clearly evidenced (Figure 3.8c). The experimental data is also superimposed to the quantum model (Figure 3.8d). A Rabi splitting energy of 205 meV is estimated.

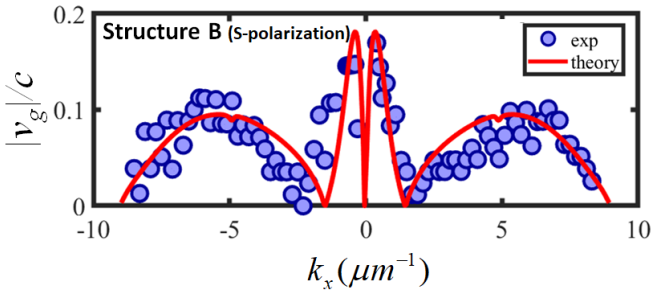

Figure 3.9. Group velocity extracted from ARR measurement of S-polarized mode in structure B

We calculated the group velocity corresponding to the S-polarized multi-valley band in the structure B reported in Figure 3.9. The two valleys correspond to the vanishing of group velocity at $|k_x| \approx 5\ \mu m^{-1}$. This multi-valley polaritonic dispersion (first observed by Wang et al. [126] could be the building block of polariton valleytronic physics [127,128]. Indeed, recent theoretical works have predicted that Bose-Einstein condensation of polaritons with W-shaped dispersion would take place at the valley extrema [128], thus paving the way to study Josephson oscillation in momentum space [129,130], spontaneous symmetry breaking and two-mode squeezing [127]. Moreover, when not working at the extrema but at $|k_x| = 0$ the W-shaped dispersion is also a perfect test bed for parametric scattering experiment [131].

3.3 Conclusion of the chapter

In conclusion, we propose periodically patterned excitonic metasurfaces as a novel platform to study exciton-polariton physics. In contrast to the traditional microcavity design, the metasurface approach offers high flexibility for the tailoring of polaritonic properties (group velocity, quality factor of localized modes, emission pattern, etc.). This platform is compact down to the sub-wavelength range, and can be applied to a wide range of excitonic materials. As a proof-of-concept, the strong coupling regime at room temperature in perovskite-based metasurfaces is experimentally observed. The results from both ARR and ARPL measurements show that the polariton dispersion shares the same shape as the one of uncoupled photonic modes when working out of the anticrossing region. This leads to polaritonic modes that can be engineered to display linear, slow-light, or even multi-valley characteristics.

CHAPTER 4

EXCITON – POLARITON BOUND STATE IN THE CONTINUUM

In the previous chapter, we have shown that the energy-momentum polaritonic dispersion can be tailored on demand with the use of perovskite metasurfaces. This has been done by engineering the real part of the polaritonic dispersion. Meanwhile, another strategy offers the possibility to manipulate polaritonic dispersion through its imaginary part (i.e., losses). Indeed, recent theoretical works have suggested that perovskite metasurfaces can harness the imaginary part of the polaritonic energy-momentum dispersion via concepts of such as Bound state in the continuum or exceptional point [132,133]. The aim of this chapter is to demonstrate experimentally the formation of polariton Bound state in the continuum and to investigate its topological properties in the excitonic metasurface made from PEPI perovskite.

Bound states in the Continuum (BICs) are peculiar localized states that are forbidden to radiate despite lying in a continuum of propagating waves. Once regarded as an `exotic' quantum mechanical effect [134], the origin of BICs is nowadays fully unraveled as a particular solution of wave equations, which has led to their exploitation in other fields where it is straightforwardly attributed to destructive interference mechanisms or symmetry mismatches [92]. One of the most active playground of BIC physics is contemporary Photonics [135], since most of optoelectronic devices rely on resonances and their coupling mechanisms with their environment. Indeed, the trapping of light through photonic BICs is a salient feature to enhance different light-matter interaction mechanisms, leading to various applications in microlasers [136–140], sensors [141], optical switches [139] and nonlinear optics [142–145]. Moreover, on the fundamental side, photonic BICs in periodic lattices are

pinned to singularities of farfield polarization vortex and can be considered as topological charges of non-Hermitian systems [95,146–148]. This topological nature, together with modern technological feasibility to tailor photonic materials, makes photonic BICs a fruitful platform to engineer polarization singularities of open photonic systems [137,149–151].

Very recently, the strong coupling regime between photonic BICs and excitonic resonances has been theoretically suggested [132,133,152,153], with two experimental demonstrations [45,154]. The result of such a coupling is the formation of polariton-BICs (pol-BICs): hybrid excitations that are completely decoupled from the radiative continuum. This scenario is quite different from the text-book architecture in which the strong coupling regime is engineered by embedding quantum wells at the antinode positions of planar microcavities, which always exhibit substantial non-radiative losses. As state-of-the-art, non-linear behaviors of pol-BICs [45] and the use of pol-BICs to trigger Bose-Einstein Condensation have been recently demonstrated [155]. However, most of these demonstrations are conducted at cryogenic temperatures. Therefore, demonstrating pol-BICs with room temperature operation would be the next important step for the development of polaritonic devices based on BIC concepts. Our objective has been to perform such a demonstration using the key properties of PEPI, exhibiting polaritonic behavior at room temperature.

4.1 Parameters for sample design

The metasurface is designed so that the exciton energy (E_X = 2.394 eV) is in the vicinity of the lowest Bloch resonances of the passive structure (PEPI is replaced by a dielectric material of constant refractive index n = 2.4). The metasurface of perovskite is fabricated using the same method as shown in chapter 3. The PEPI solution is infiltrated inside air holes of a pre-patterned silica backbone via spin coating, then followed by thermal annealing to form a square lattice of crystallized PEPI nano-pillars. The final sample is encapsulated with PMMA to protect PEPI

against humidity.

RCWA simulation were conducted with different tunable parameters of the structure to study the Bloch resonances in the vicinity of PEPI exciton energy. The lattice parameters of the metasurface such as lattice constant (a), filling factor (here defined as ratio of diameter of PEPI pillars over period FF=d/a), and PEPI thickness are essential in engineering the photonic energy-momentum dispersion. From the simulation results, a period a=330 nm is selected for the final design. Indeed, preliminary simulations showed that the structures with this period exhibit photonic BICs in the range of PEPI exciton in S-polarization.

Next, the effect of filling factor on dispersion engineering is studied by carrying out RCWA simulation of passive structures with various values of filling factors. In this part, we focus on the results of absorptions simulation. Unlike reflectivity dispersions which also show some signals from the background, these absorption dispersions exhibit the resonances coming from the metasurface (without back reflection), hence give us better way to observe BICs.

Figure 4.1 describes the absorption as a function of a/λ (proportional to photon energy) and the component of wavevector $k_x\left(2\pi/a\right)$ of structures having lattice constant a = 330 nm, PEPI of 180 nm thickness in total filled in 150 nm in height of SiO_2 hole lattice (150 nm PEPI completely filled in and 30 nm PEPI residues as slab), 200 nm of PMMA with three different values of filling factor in this example. As shown in Figure 4.1, within PEPI metasurface with period 330 nm, there are two photonic BICs (marked by the local vanishing in absorption dispersion) at Γ point observed in the vicinity of PEPI exciton: BIC_1 (located at higher energy) and BIC_2 (located at lower energy).

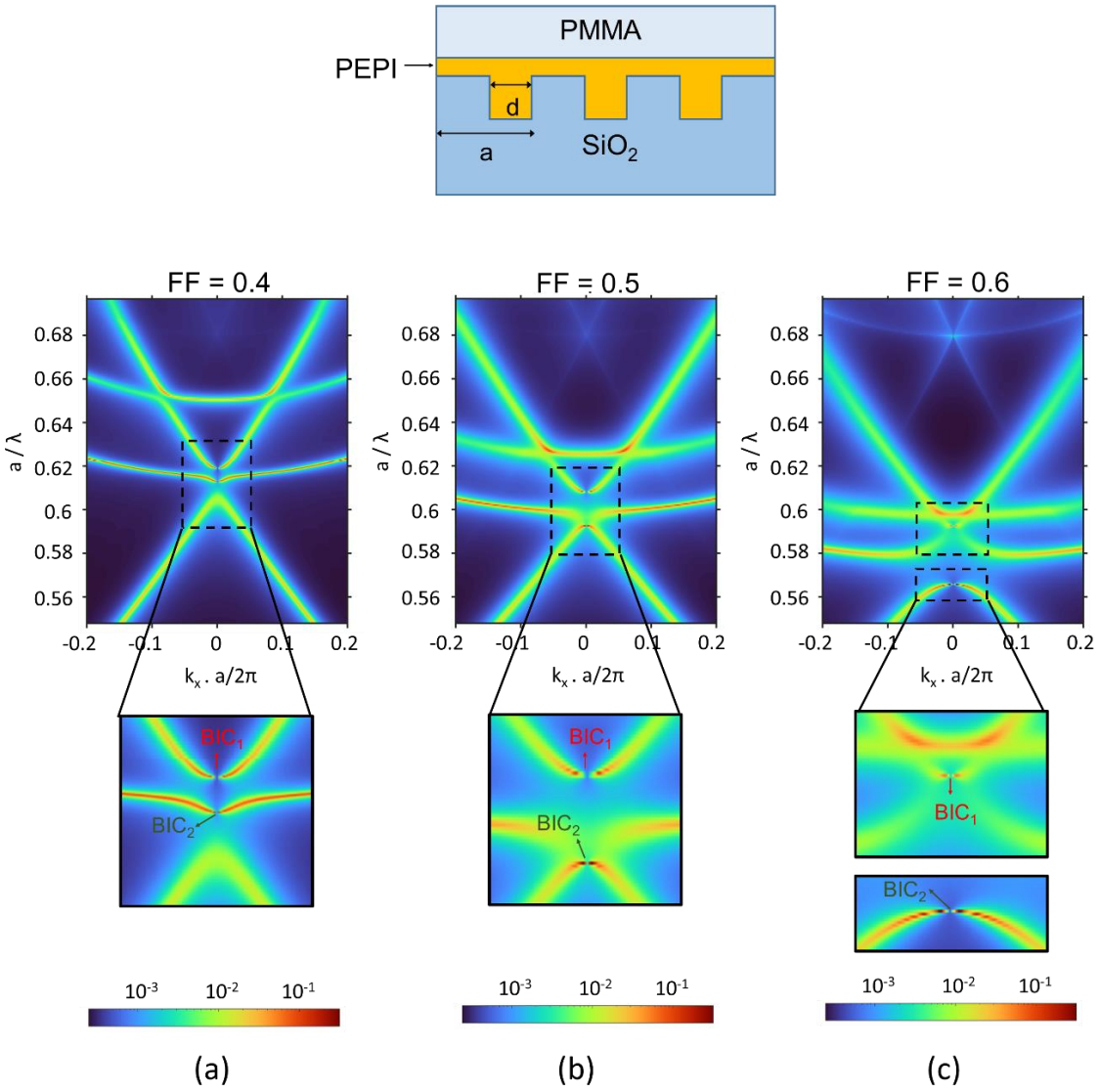

Figure 4.1. RCWA simulation showing angle-resolved absorption of passive structure with a=330nm, t_{hole}=150nm, $t_{PEPI\ total}$=180nm (150nm PEPI filled in + 30 nm PEPI slab) and three different values of filling factor: FF = 0.4 (a), FF = 0.5 (b), FF = 0.6 (c).

We can see that by increasing the filling factor from 0.4 to 0.5 and to 0.6, not only the dispersion is shifted to lower energy but also the positions of the two BICs are changed to different photonic bands. For example, with FF= 0.4 (Figure 4.1a), the lowest resonance is a leaky mode, BICs are located in two other bands, at slightly higher energy (one slow light mode and one fast mode). When FF increases to 0.5 (Figure 4.1b), the gap between two lowest

resonances is closed, leading to the degeneracy between these two modes. BIC_2 is now exchanged from the slow light mode to the lowest energy mode, the slow light mode becomes high-loss, meanwhile BIC_1 remains in the highest energy band. In the case FF= 0.6 (Figure 4.1c), the gap between the two highest energy mode is closed. Meanwhile, the gap between the slow light mode and the lowest energy band is reopened, BIC_1 is located in the highest band which is now degenerated with the slow light mode, BIC_2 remains in the lowest energy band. These band flip and BICs interband transition features have been investigated and modelled [132,156]. In these studies, it has been shown that the filling factor plays an important role to control the formation of BICs. Here, a filling factor of 0.4, presenting dispersion with two BICs located in separated bands is chosen for the final design.

We now investigate the effect of PEPI thickness and PEPI infiltration in photonic BICs. RCWA simulation of passive structure (a = 330 nm, FF = 0.4, t_{hole}=150 nm) were carried out varying three main different perovskite infiltration/thickness: partial infiltration of 100 nm-thickness (Figure 4.2a), full infiltration of 150 nm-thickness (Figure 4.2b), and full infiltration with a 30 nm-thick residual slab (Figure 4.2c).

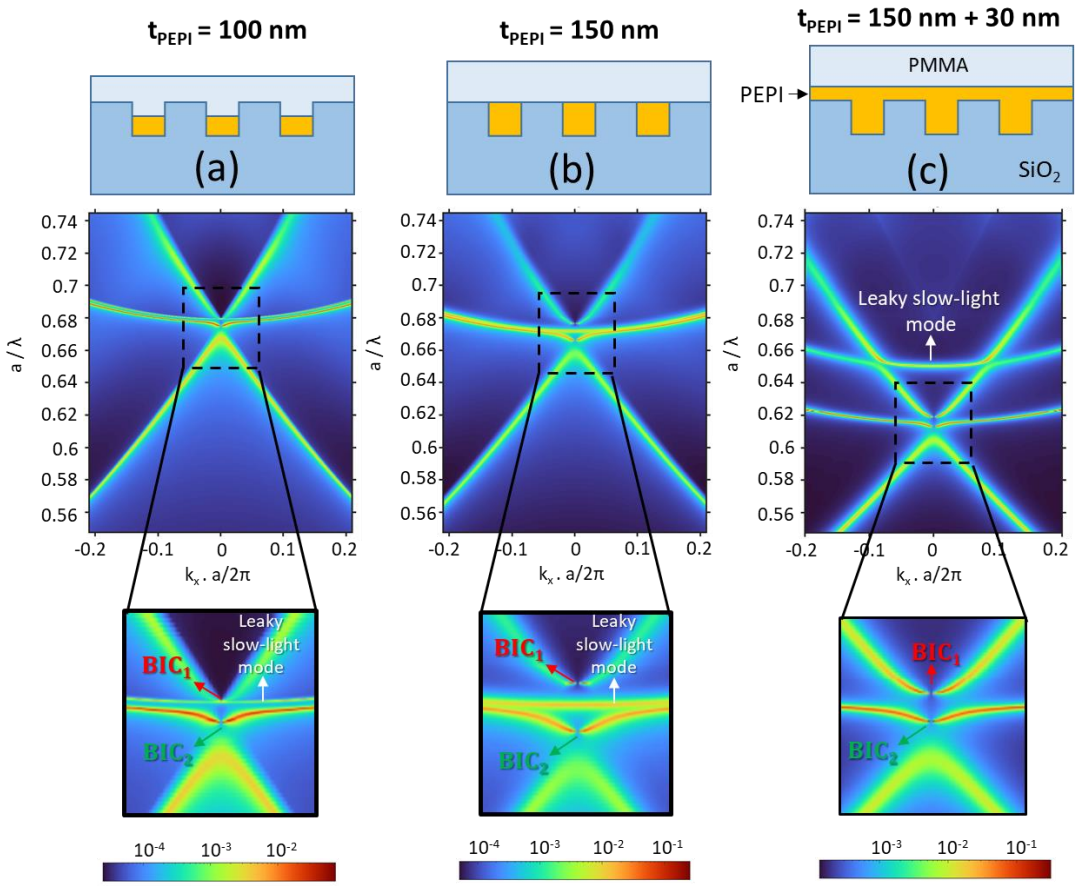

Figure 4.2. RCWA absorption simulation of passive structure (a = 330 nm, FF = 0.4) corresponding to three different perovskite infiltration: partial infiltration of 100 nm-thickness (a), full infiltration of 150 nm-thickness (b), and full infiltration with a 30 nm-thick residual slab (c).

Our simulations show that for partial infiltration, the BIC_1 mode almost degenerates with a leaky slow-light mode. For full infiltration, the degeneracy is lifted but the leaky slow-light mode is still in the vicinity of BIC_1 and may cause difficulty to characterize BIC features in experimental setup. However, when a 30 nm-thick residual slab is implemented, the leaky slow-light mode will lie at a much higher energy and our two BIC modes (BIC_1 and BIC_2) are well isolated. Here, the structure with a residual 30nm PEPI slab appears to be the most appropriate since it isolates the BIC mode from a slow-light leaky mode; it was therefore chosen for the final implementation.

4.2 Sample design and photonic BICs

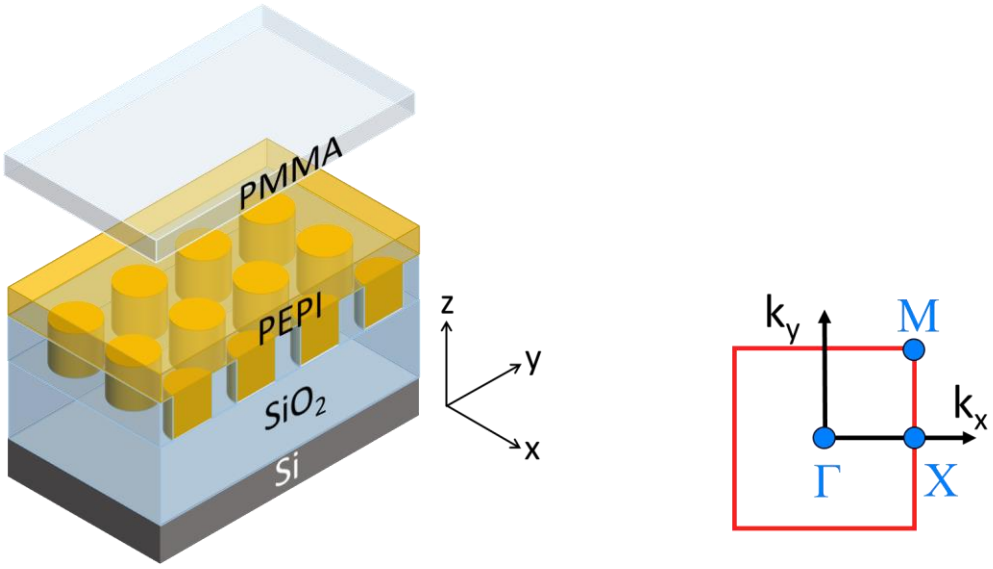

Figure 4.3. (a) Sketch of final design for perovskite metasurface. (b) The reciprocal space with Brillouin zone of size 2π/a, corresponding to a square lattice of period a.

The final design of the PEPI metasurface is illustrated in Figure 4.3a. The backbone consists of a 2 μm-thick thermal SiO_2 layer on a silicon substrate. It is pre-patterned into a square lattice of holes, with a period a = 330 nm, a diameter d = 132 nm, corresponding to a filling factor FF=0.4, and a depth t_{etch} = 150 nm. The crystallized perovskite layer has a total thickness t_{PEPI} = 180 nm in which 150 nm of PEPI completely filled in the SiO_2 hole lattice and a 30 nm-PEPI residue on top as a slab. The final structure is encapsulated by a 200 nm-thick PMMA layer. In this work, the dispersion is calculated and characterized along the ΓX direction (Figure 4.3 b).

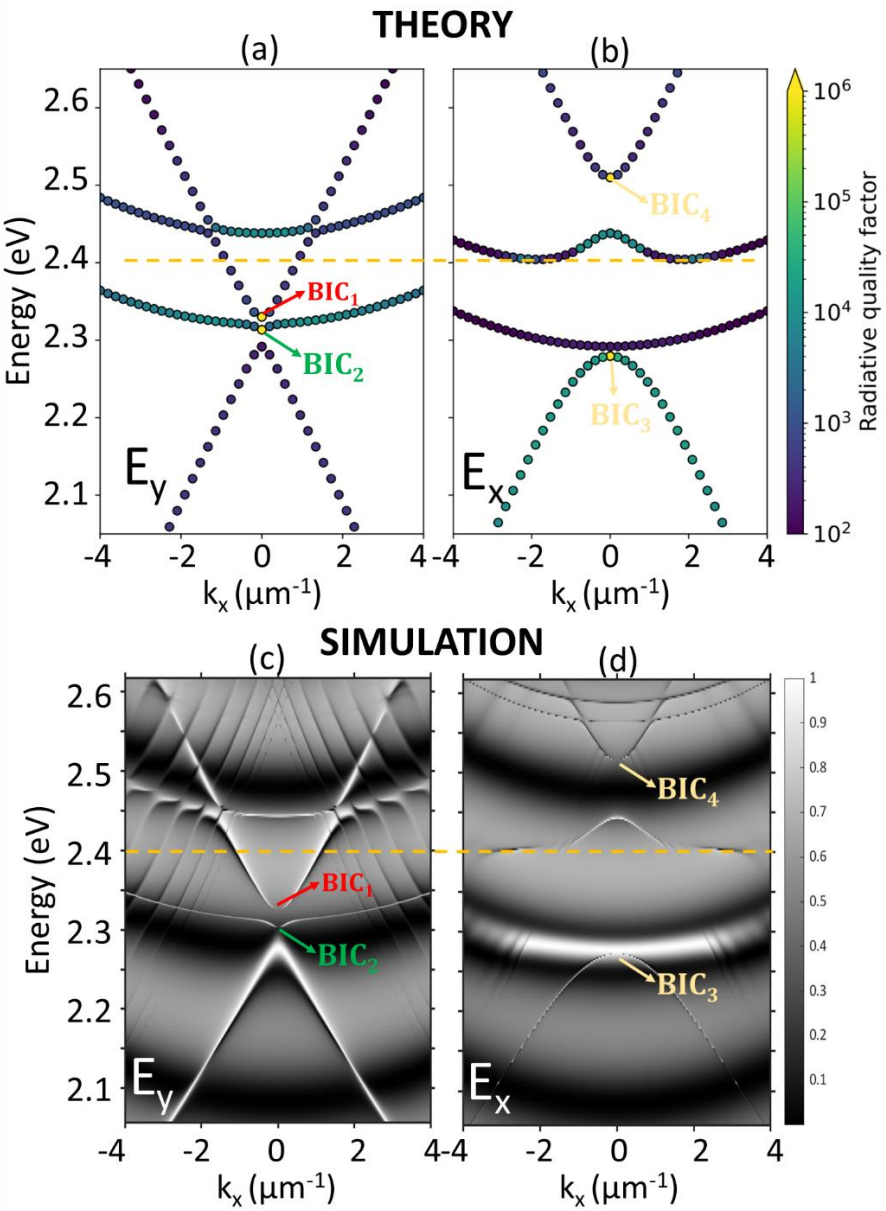

Figure 4.4. Comparison between theoretical band structure of the passive PEPI metasurface, calculated by using the GME method (top panels) for both odd parity (a) and even parity (b) with respect to the xz plane, and the angle-resolved reflectivity spectra simulated by RCWA method (lower panels) excited by two polarized lights: (c) ↕ (i.e. y) polarized light and (d) ↔ (i.e. x) polarized light.

The band structure of this metasurface shown in Figure 4.4 upper panels, has been modeled by Dario Gerace and Simone Zanotti from University of Pavia by Guided-Mode Expansion (GME) method [157] in the frame of a collaboration. This method was generalized to deal with multilayered and partially etched dielectric materials [158], was used to calculate

the theoretical band structure in the case of the final design of PEPI metasurface. This is compared with simulated band structures numerically simulated using the RCWA method. Here, the considered structure is the passive one. In Figure 4.4 upper panels, theoretical bands were calculated by GME for both odd and even parities with respect to the mirror symmetry for reflection on the xz (y = 0) plane. On the other hand, Figure 4.4 lower panels presents the calculated angle-resolved reflectivity (ARR) of the passive structure calculated using RCWA method when excited by two polarized lights: ↕ (i.e. y) polarized light or s-polarized (transverse electric, TE); and ↔ (i.e. x) polarized light or p-polarized (transverse magnetic, TM) with respect to the xz plane of incidence.

Similarly to the angle resolved absorption (Figure 4.1a, Figure 4.2c), ARR obtained from RCWA in ↕ (i.e. y) polarization shows two BICs corresponding to the local vanishings of reflectivity resonances at $k_x = 0$ and a leaky mode is shown in with a maximum slightly below 2.3 eV (Figure 4.4c). These results show very good agreement with the results of GME calculation for odd modes (Figure 4.4a), which confirms that the lowest mode is a bright one (low Q-factor) at Γ point, while two BICs are present at slightly higher energies exhibiting quality factors over 10^6.

Indeed, Figure 4.4b,d show that apart from BIC_1 and BIC_2 in ↕ (i.e. y) polarization, other photonic BICs (here denoted BIC_3 and BIC_4) exist and can be excited in ↔ (i.e. x) polarization. However, they are far from the excitonic resonances (BIC_3 is at lower frequency and BIC_4 is at higher frequency), and their strong coupling with the excitonic resonance is expected to result in pol-BICs with a strong photonic character. Later, we noted that these BICs are not populated in photoluminescence measurements.

As a results, we only focus on the study of only photonic BIC_1 and BIC_2. The theoretical electric field patterns of these photonic BICs are reported in Figure 4.5a,b, showing both Ex

and Ey components, both in vertical and planar cross sections. The odd parity of these spatial profiles for mirror symmetry through either xz or yz planes confirms that they are both symmetry-protected BICs, i.e., they are forbidden to couple to the radiative continuum due to their symmetry mismatch with radiative plane waves.

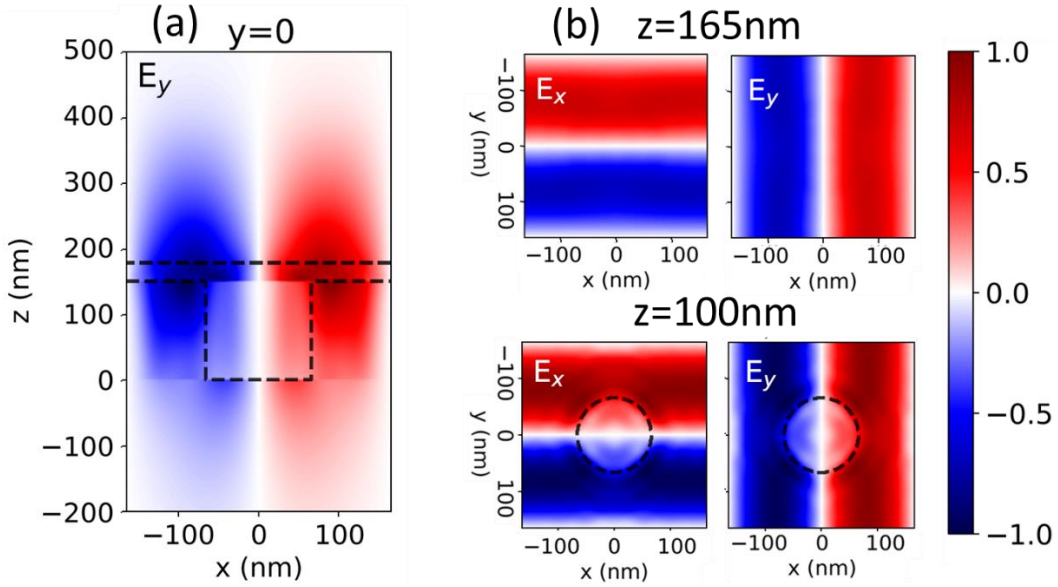

Figure 4.5. (a) Spatial distribution of the electric field in the xz plane within a single unit cell of the square lattice, as obtained for the BIC_1 mode, and (b) corresponding cross sections in the xy plane for two different vertical coordinates, corresponding either to the patterned region (PEPI infiltrated hole) or the uniform PEPI region.

4.3 Strong coupling between photonic BIC and excitonic resonance

We now investigate the coupling between PEPI excitons and the previous Bloch resonances, giving rise to polaritonic modes [43] . The experimental results of angle resolved reflectivity measurements (Figure 4.6b) and numerical ones from RCWA simulation (Figure 4.6c) are in good agreement. The strong coupling regime is evidently demonstrated in both experimental and numerical results, by comparison with the simulations of the passive structures (i.e., without considering the excitonic response) in Figure 4.6a. Indeed, all the dispersion curves are strongly red-shifted from the bare exciton energy to form polaritonic

branches. In particular, the anticrossings between the first lower polariton branch, here denoted LP, and the first upper polariton branch, here denoted UP, are clearly evidenced. The measured Rabi splitting $\hbar\Omega \approx 200$ meV, which is in good agreement with the previous reports on polaritons in a PEPI metasurface [159].

Since the polaritonic modes inherit the symmetry properties of their photonic component, the first two LP branches possess the same odd parity at Γ point as the one of BIC_1 and BIC_2. Therefore, they must be symmetry-protected pol-BICs, denoted as pol-BIC_1 and pol-BIC_2, according to their photonic counterparts.

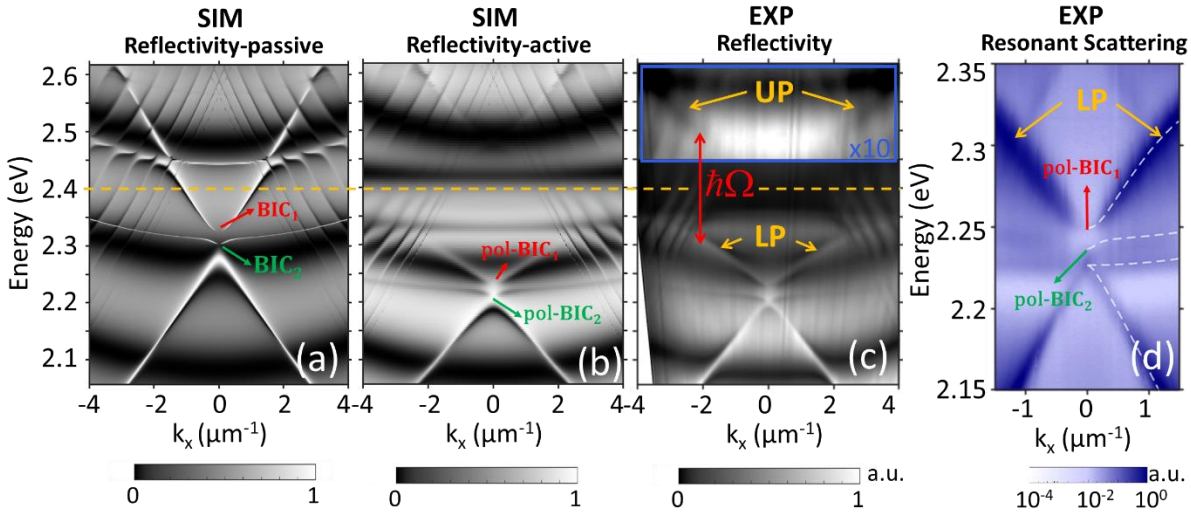

Figure 4.6. (a) Numerical simulations of the ARR spectra calculated for the passive structure, (b) same simulation for the active structure when excited by ↕ (i.e. y) polarized light; also here the dashed line indicates the bare excitonic resonance of PEPI. (c) Experimental result of the ARR of the PEPI metasurface when excited by ↕ polarized light. The measured Rabi splitting $\hbar\Omega \approx 200$ meV. (d) Experimental result of the angle-resolved resonant scattering of the PEPI metasurface, zoomed in the vicinity of the two pol-BICs. The excitation is polarized along ⤢ (i.e. 45 degrees) and the detection is analyzed along ⤡ (i.e. -45 degrees). The dotted lines are guides to the eye to distinguish the 4 polaritonic modes.

To evidence their decoupling from the radiative electromagnetic continuum, a

straightforward criterion is the vanishing of these resonances at the Γ point, i.e. at normal incidence with respect to the metasurface. Although these vanishing resonances are hinted in Figures 4.6(b,c), it is a tricky observation because the reflectivity resonances corresponding to these guided modes have Fano-like profiles superimposed on a shallow Fabry-Perot modulation deriving from the 2 μm-thick SiO_2 layer [160].

Figure 4.7 compares side by side numerical simulation results of ARR in Ey polarization of the same metasurface on two different substrates: 2μm SiO_2 on Si substrate and pure SiO2. These results allow to confirm which resonances come from the metasurface and not from the vertical Fabry-Perot resonances within the SiO_2 layer.

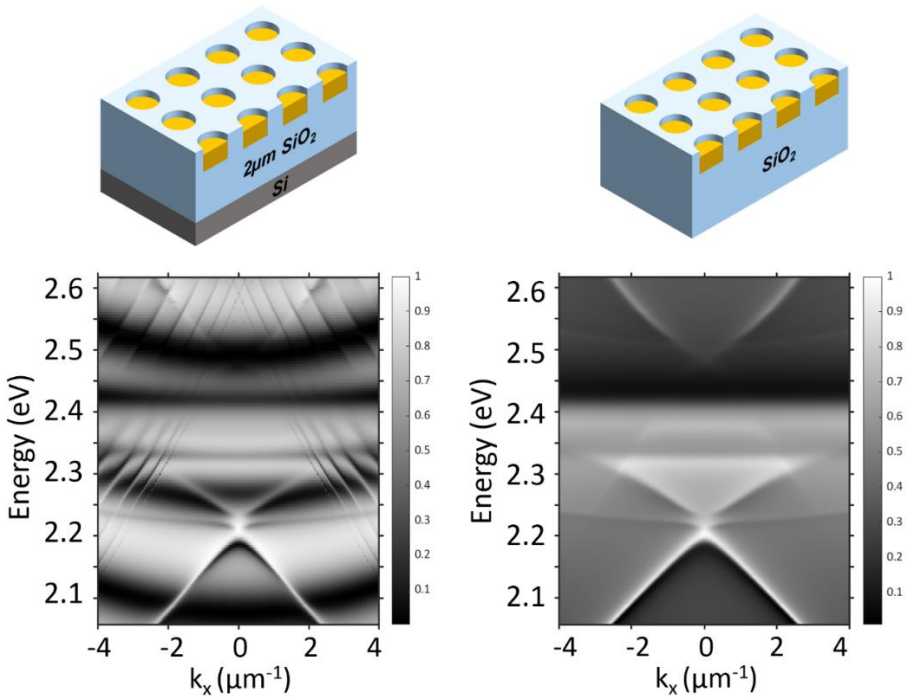

Figure 4.7. Comparison between angle-resolved reflectivity spectra simulated by RCWA method of PEPI infiltrated inside 2μm SiO_2 on Si substrate (left panel) and inside pure SiO_2 substrate (right panel).

We get rid of such a background by employing resonant scattering measurements [161], in which the excitation and detection are in cross-polarization configuration (excitation in 45-degrees polarization direction, and analyzed in -45-degrees one). As shown in Figure 4.6 d, we

observe all four polariton lower branches, corresponding to the four Bloch resonances previously discussed. Notably, the resonant scattering results feature both E_x and E_y polarized modes. Indeed, the leaky branch of high curvature of E_x polarization is observed in resonant scattering results, and not in reflectivity measurements of E_y polarization. Most importantly, as expected, the resonant scattering vanishes locally at the two pol-BICs.

The reflectivity and resonant scattering measurements show that the PEPI metasurface can host pol-BICs modes. To populate these polaritonic modes and study their farfield emission, we perform non-resonant pumping (λ_{laser} = 405 nm, 80 MHz, 50 ps) with the same Fourier spectroscopy setup. Angle-resolved photoluminescence results, shown in Figure 4.8a, indicate that only the LP branch is efficiently populated while other modes (the UP and photonic-like bands at low energy) are either not observed or weakly populated. This observation is in good agreement with polaritonic behaviors in high bandgap materials for which the photoluminescence emission is mainly visible for the first lower polariton branch. The farfield emission of the LP vanishes locally at $k_x = 0$ where the pol-BIC_1 resides. Such effect, already shown in Figure 4.8a, is clearly evidenced in Figure 4.8b where the photoluminescence intensity of the LP is tracked and reported. We note that the excitonic fraction of the pol-BIC_1 amounts to 35% as estimated from a simple model of two coupled oscillators, in which we take half of the Rabi splitting as the radiation matter coupling energy (off-diagonal element in the 2 matrices, much larger than the oscillators linewidths) and the exciton-photon detuning estimated from the passive photonic BIC_1 mode (Figure 4.4a) indicating that it is indeed a hybrid exciton-photon entity.

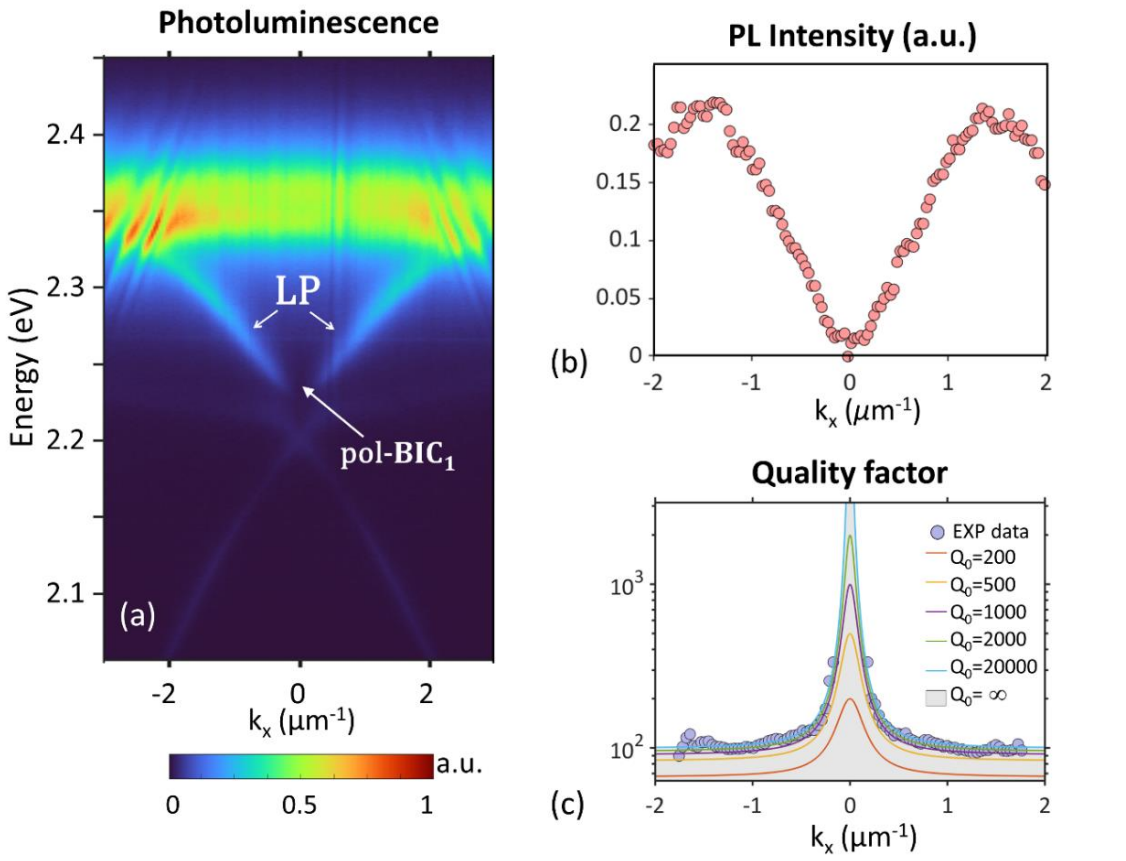

Figure 4.8. (a) Angle-resolved photoluminescence results, analyzed along ↕ (i.e. y). (b) Angle-resolved emission intensity of the LP. (c) The quality factor of the LP extracted from the photoluminescence measurements. The blue circles are experimental data, the solid lines correspond to the model in Eq 4.1 with Q_∞=95, α =5.9 μm^2 but using different values of Q_0. The gray shading area corresponds to $Q_0=\infty$.

We now discuss on the use of photonic BICs to enhance the quality factor of polaritonic modes. Although this effect has been briefly mentioned in Ref [45], the underlying mechanism of quality factor enhancement, as well as its intrinsic limit, has not been reported yet. Since photonic BICs possess an ideally infinite quality factor, one may expect the same for pol-BICs. However, due to their hybrid exciton-photon nature, the quality factor of pol-BICs is balanced between the non-radiative losses of the excitonic component and the one from the photonic BIC component [132]. They are thus quasi-BICs, whose quality factor is limited by non-radiative losses. Moreover, the C4 symmetry of the square-lattice imposes that the quality factor of

photonic BICs decreases as k^2_x at oblique angles [137]. Therefore, within a small angular window close to normal incidence, the quality factor Q (k_x) of the LP can be determined from a relatively simple law:

$$Q(k_x)^{-1} = Q_0^{-1} + \left(Q_\infty + \frac{\alpha}{k_x^2}\right)^{-1} \qquad \text{(Eq 4.1)}$$

in which Q_0 corresponds to the non-radiative losses originated from the excitonic component, $Q\infty$ corresponds to the radiative losses of the photonic BIC at high oblique angles, and the coefficient α dictates the decreasing rate of the photonic BIC. Figure 4.8c depicts the angular dependence of the quality factor of the LPB extracted from the photoluminescence spectra. The value of $Q\infty$ is easily extracted from the experimental data. Indeed, assuming that $Q\infty \ll Q_0$, the value of $Q\infty$ corresponds to the measured quality factor at high wavevector (> 1.5μm^{-1}). Thus $Q\infty \approx 100$. The value of Q_0 is more challenging to obtain since the photoluminescence signal from normal emission angle is strictly zero due to the BIC nature. Nevertheless, we can use the angular dependence of the quality factor to evaluate Q_0. The experimental data are nicely fitted by the model (Eq 4.1), with $Q\infty = 95$, $\alpha = 5.9$ μm^2 and $Q_0 > 1000$. Therefore, our pol-BIC exhibits a quasi-BIC nature, indeed, having infinite radiative quality factor inherited from the photonic component, but a finite non-radiative one (>1000) inherited from the excitonic component. This property is fundamental and crucial for designing polaritonic devices using BIC concepts: there is a trade-off between infinite quality factor (from photonic fraction) and giant nonlinearity (from excitonic fraction).

4.4 Topological nature of pol-BICs

Finally, we focus the discussion on the topological nature of pol-BICs. At the time of our study, this fundamental property of pol-BICs has not been addressed in the literature, either theoretically or experimentally. Despite being quasi-BICs with finite quality factor, we expect

that pol-BICs preserve the nature of singularities in momentum space. This is due to a complete decoupling from the radiative continuum (see Chapter 1, Section 1.5.3). As a consequence, every polaritonic branch that hosts a pol-BIC mode should exhibit a polarization vortex around this singularity. Thus, pol-BICs are expected to fully inherit the topological behavior of their photonic components.

The various polarization states of electromagnetic radiation can be presented by the Poincaré sphere and can be described by Stoke parameters S_1, S_2, S_3 which relate to the sphere coordinates of polarization state [162]. S_1 and S_2 characterize linear polarization while S_3 characterizes circular polarization.

Three Stoke parameters are calculated as follow:

$$S_1 = \frac{I_{\leftrightarrow} - I_{\updownarrow}}{I_{\leftrightarrow} + I_{\updownarrow}} \qquad S_2 = \frac{I_{\nearrow} - I_{\nwarrow}}{I_{\nearrow} + I_{\nwarrow}} \qquad S_3 = \frac{I_{\circlearrowleft} - I_{\circlearrowright}}{I_{\circlearrowleft} + I_{\circlearrowright}}$$

(Eq 4.2)

I is the intensity of the light when analyzed at each polarization. S_1 is the coordinate corresponding to the degree of horizontal (↔) versus vertical (↕) polarization. S_2 is the coordinate corresponding to the degree of diagonal (↗) versus anti-diagonal (↖) polarization. S_3 is the coordinate corresponding to the degree of left circular (↺) versus right circular (↻) polarization.

Here we applied a band pass filter to select the signal at around pol-BIC_1 (between E_1 = 2.285 eV and E_2 = 2.22 eV). Figure 4.9 shows the PL dispersion of LP before and after the use of the spectral filter.

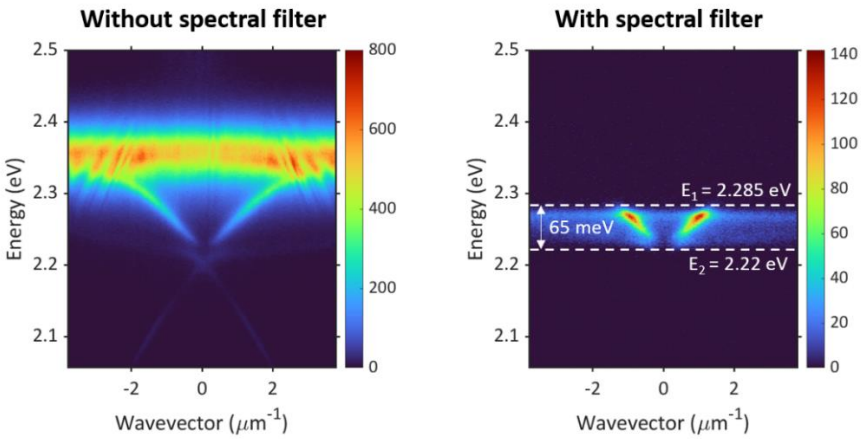

Figure 4.9. Experimental angle-resolved photoluminescence dispersion with and without spectral filter excited by ↕ polarized light.

For mapping the Stoke parameters, a half wave plate, a quarter wave plate and a polarization analyzer are used to select each one of the six polarization states (i.e., ↔). Isofrequency maps of populated LP (in the pol-BIC$_1$ selection range) excited in four polarization $I_{\updownarrow}$, $I_{\leftrightarrow}$, $I_{\nearrow}$, $I_{\nwarrow}$ are shown in Figure 4.10 giving the information on the topological singularities of pol-BIC$_1$. These results present the polarization states of the perovskite emission at each point in the k_x-k_y plane.

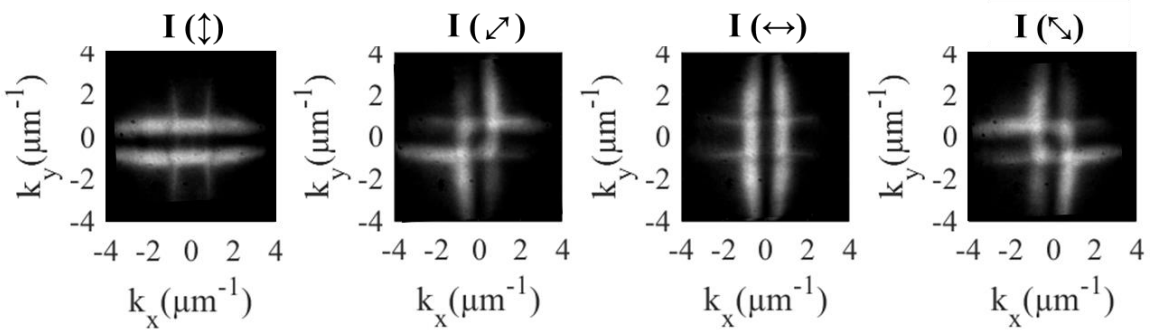

Figure 4.10. Four polarization components ($I_{\updownarrow}$, $I_{\nearrow}$, $I_{\leftrightarrow}$, $I_{\nwarrow}$) of PL in the Fourier plane (i.e. k_x - k_y). These PL measurements were conducted at around pol-BIC$_1$.

From the isofrequency maps, we can calculate the values of the Stoke parameters following Equation 4.2. We note that the value of S_3 Stoke parameter obtained from this system, is relatively small: $|S_3| \ll 1$. Moreover, it is momentum-mismatched with the BIC as it takes

place at large wavevectors (k~5 μm^{-1}), while the BIC is at k=0. For this reason, though S_3 value is different than zero, it is not expected to modify the results for the topological charge. Here, we focus on linear polarization of pol-BIC$_1$ (S_1 and S_2).

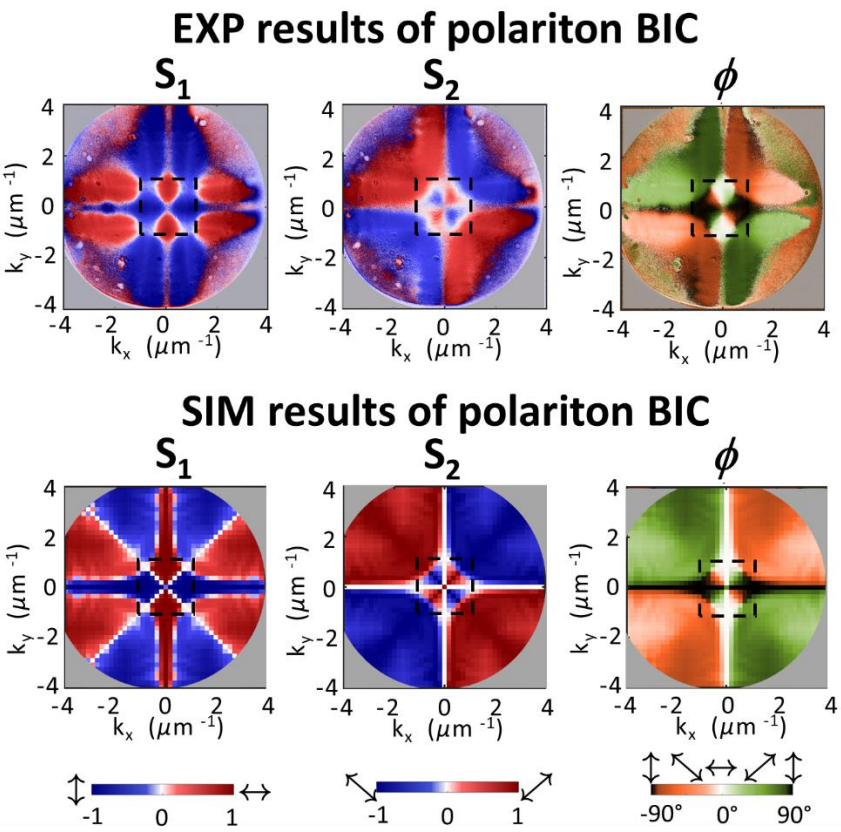

Figure 4.11. Stoke parameters obtained from experiments and from RCWA simulation in wide angle, between k_{min}=-4 and k_{max}=4. The interested range to study pol-BIC$_1$ vortex feature is marked inside dashed-line square.

Figure 4.11 shows the normalized Stokes parameters (S_1, S_2, and polarization orientation φ) at polariton bands above pol-BIC$_1$ energy calculated from the four polarization components obtained from PL characterization (Figure 4.10) and numerical simulation. From these results, we can confirm that there is a good match between PL isofrequency measurements and numerical simulation by RCWA method. To investigate the polarization vortex feature appearing near the Γ point, we take a closer view at pol-BIC$_1$ by zooming in Stokes parameters between $k_{min} = -1\ \mu m^{-1}$ and $k_{min} = 1\ \mu m^{-1}$ (Figure 4.12).

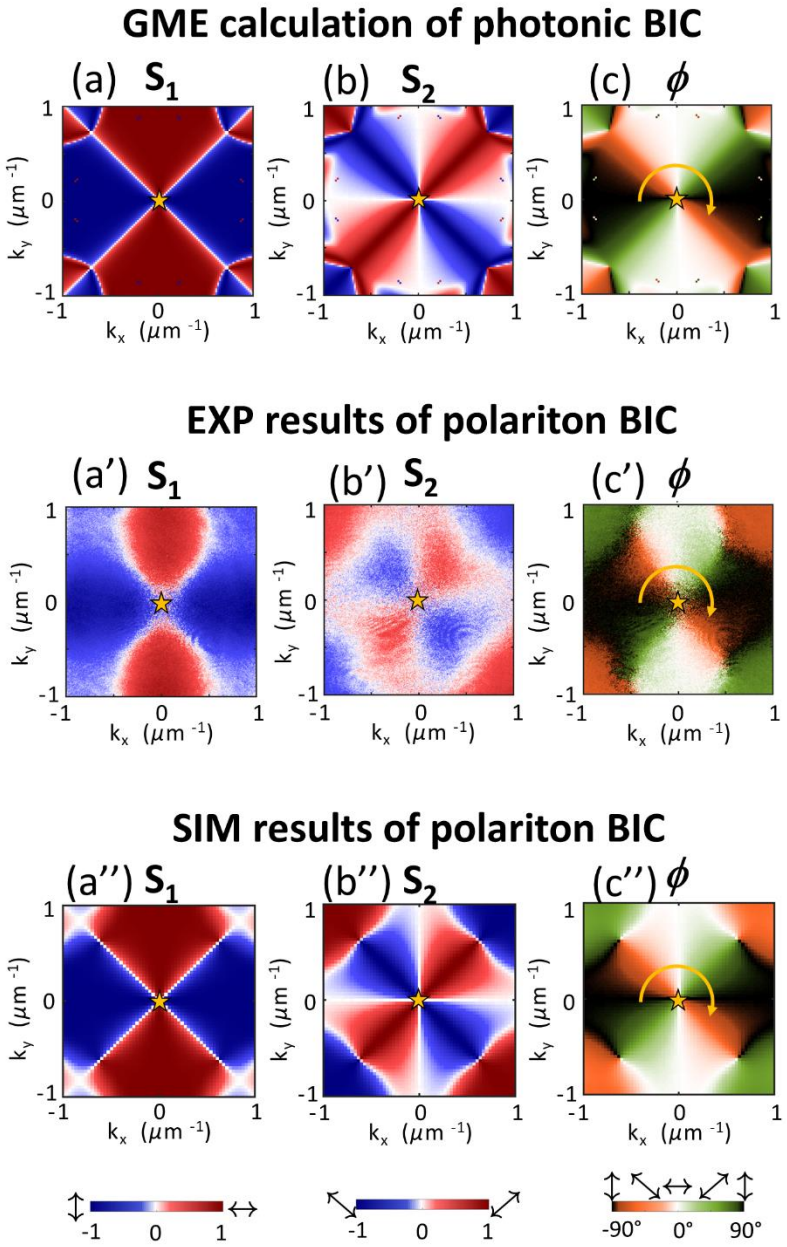

Figure 4.12. Theoretical Stokes parameters S1 (a), S2 (b), and the polarization orientation φ (c) as obtained from GME simulations of the passive structure and corresponding to the BIC₁ Bloch mode. Experimental results for the mapping of S₁ (a'), S₂ (b'), and the polarization orientation φ (c') corresponding to pol-BIC₁. Numerical results of S₁ (a''), S2 (b''), and polarization orientation (c''), as obtained from RCWA simulations of the active structure and corresponding to the pol-BIC₁.

At first, we verify the topological nature of the purely photonic BIC_1 of the passive photonic structure calculated from the GME results (see Figure 4.4a). Figures 4.12a,b depict

the theoretically determined Stokes parameters S_1 and S_2 of the photonic BIC_1. These results clearly evidence the existence of a polarization singularity at the Γ point in the reciprocal space. From the mapping of S_1 and S_2, we can easily extract the polarization orientation, φ (given by the relation $\tan\{2\varphi\} = S_2/S_1$). The latter is reported in Figure 4.12c, showing that φ decreases by an angle 2π when the Γ point is encircled. Therefore, the photonic BIC_1 is associated to a topological charge q, given by [95]:

$$q = \frac{1}{2\pi}\oint_C dk.\nabla_k\phi = -1 \qquad \text{(e.q 4.3)}$$

This numerical result is in good agreement with the topological charge predicted by group theory corresponding to the C4 in-plane symmetry of our square lattice (see detail in Appendix C). We now investigate experimentally the polarization pattern of the LP branch in the vicinity of the pol-BIC_1. Figures 4.12a',b',c' present the measured Stokes parameters S_1 (Figure 4.12a'), S_2 (Figure 4.12b') and the extracted orientation φ (Figure 4.12c'). The corresponding numerical results of the active structure, obtained by RCWA simulations, are presented in Figures 4.12a",b",c", showing an almost perfect agreement with the experimental data. Both experimental and numerical results clearly evidence a polarization vortex, associated to a topological charge $q = -1$ of the LP branch at the Γ point. Most importantly, the striking similarity between the calculated polarization patterns of BIC_1 (Figures 4.12a,b,c) and the ones measured from pol-BIC_1 confirm that the topological charge of the purely photonic BIC, $q = -1$, has been fully transferred to the polaritonic one. In other words, the topological nature of pol-BICs is indeed originated from the purely photonic BIC components.

4.5 Conclusion of the chapter

In conclusion, we have experimentally demonstrated the formation of polariton BICs at room temperature in a perovskite-based resonant metasurface. This is the first observation of the topological charge of polariton BICs. Moreover, the quasi-BIC nature, resulting from the hybridization between photonic BIC and excitonic resonance, is discussed and analyzed for the first time: as hybrid eigenmodes, these excitations inherit the non-radiative losses from the excitonic component, but at the same time preserve the topological nature of the purely photonic BIC. Our results suggest that excitonic metasurface is a promising platform to reveals and exploits polariton effects (such as nonlinearity, or interaction with a magnetic field) with the engineering of polarization singularities. A straightforward application of the current work is to engineer polarization vortex beam lasing by reaching the Bose-Einstein condensation regime. Such highly directional coherent light sources, exhibiting polarization singularities at the center with doughnut-shape intensity, are highly desirable for applications in high-resolution imaging [163,164], focusing [165–167], optical manipulation [168,169], communication [170,171] and data storage [172]. From a fundamental point of view, this would pave the way to explore new regimes of polariton condensation and quantum fluids of light, in which the condensate is totally decoupled from the radiative continuum and is purely non-radiative. Another attractive perspective is to use polariton nonlinearity, inherited from the excitonic component [173] to control the merging/splitting of topological charges [137,140], or to explore the multistable regimes of BIC physics [142,144]. Such a regime, only theoretically predicted [142,144], would pave the way towards ultrafast and low threshold all-optical devices such as polariton memories, switches, or transistors operating at room temperature.

CHAPTER 5

BALLISTIC PROPAGATION OF EXCITON-POLARITONS IN PEROVSKITE METASURFACE

In this chapter, our objective is to exploit the concept of patterned excitonic surface, with a view to study polariton propagation. In particular, the major challenge is to obtain long-distance polariton propagation at room temperature, with a high excitonic component. Before presenting original results, I will first review the state of the art of polariton propagation.

5.1 State of the art of polariton propagation

Study of polariton propagation is the key to develop polaritonic signal transmitting devices with high speed and efficiency. Thanks to their hybrid nature, the propagation of these quasiparticles exhibits properties that cannot be obtained with pure photonic or excitonic transport. First, inherited from the photonic component, exciton – polaritons possess small effective mass and high group velocity. These features make it possible to obtain ballistic propagation for polariton transport over macroscopic distance, and optical access to mold this propagation by engineering potential landscape [174,175]. Moreover, thanks to the excitonic component, polariton transport can reveal nonlinear behaviors such as propagating solitons [176], nonlinear tunneling effect [177]or even entering superfluid regime [178–180]. Finally, it is possible to drive the polariton propagation by external field that interacts with the polariton flow via its excitonic component [181] [182].

Material	**Photonic modes** (type of confinement)	**D** (μm)	**L** (μm)	v_g (μm/ps)	τ (ps)	**T** (K)	**Wx** (%)	**Ref.**
GaAs	Microwire FP	100	30	2	15	10	32	[183]
GaAs/	Planar FP	200	140	1.43	> 100	< 10	10 – 20	[175,184–187]
InGaAs	Guided modes in waveguides	500	280	26	10.7	5	47	[188]
GaAs	island + modulated microwire FP	60	35	2	17.5	10	39	[189]
GaN	Waveguide	55	100	25	1-2	4	4	[190]
Organic	Bloch surface waves	120	24	120	0.2	RT	20	[123,191]
TMD	Bloch surface waves	60	15	149	0.103	RT	16	[19]
$CsPbBr_3$ Perovskite	Microwire FP	60	30	10	3	RT	30	[22]
PEPI Perovskite	**Guided resonances in metasurface**	**100**	**21**	**30**	**1.26**	**RT**	**75**	**This work**

Table 5.1. Detailed properties of polariton propagation generated from strongly coupling of excitons from different materials with photons from different optical cavities. When the confinement is generated by Fabry-Pérot cavity, the photonic mode is noted as FP. D is the observed propagation distance. L is propagation length that is extracted from the decay length of polariton propagation during the propagation. This length is also given by multiplying the group velocity by the lifetime $L = v_g \times \tau$. When the propagation is observed at room temperature, the temperature is noted as RT.

Table 5.1 reports and compares the properties of ballistic polariton propagation in the literature. One may see from this table that the various choices of material platform and photonic confinement strategies lead to very different properties (temperature of operation, propagation length, group velocity, lifetime, exitonic fraction).

On the material side, GaAs-based systems are the most used materials for exciton-polariton demonstrations and also in polariton propagation [175,183–189]. GaAs quantum

wells, possessing high crystal quality and a significant narrow exciton linewidth, can exhibit even greater quality factor than cavity photons. Hence, the most common strategy to enhance lifetime of GaAs polariton for long distance propagation focused on improving the quality factor of the cavity. This is shown in Table 5.1. Most of the works on GaAs system use Fabry Perot cavity made of Distributed Bragg Reflectors possessing quality factor in the range of few ten thousands. This resulted in long lifetime polariton states. In 2013, Steger et al. have demonstrated cavity GaAs/AlAs polariton with lifetime ranging up to 100 ps, likely two order of magnitude larger than the lifetime of other excitonic material based polaritons, leading to propagation length above 140 μm [184]. Although GaAs based polaritonic systems exhibit impressive transport performance, their working temperature is limited to cryogenic temperature which is not compatible for practical applications. A wide range of excitonic materials have been studied including organic materials [123,191,192], ZnO [125], GaN [190], TMD [19] and perovskite [22] to bring polariton propagation to room temperature.

Moreover, regarding the photonic aspect, while planar cavity is still the most popular configuration to study strong coupling physics, photonic guided modes in wave guides or dielectric surface modes (Bloch surface waves) have recently become a popular confinement scheme to demonstrate propagating polaritons thanks to a superior group velocity with respect to the one of Fabry-Pérot confinement. Indeed, using high-speed guided modes can cope with a lower material quality to obtain macroscopic propagation length. For example, the propagation length of 143 μm in GaAs based Fabry-Pérot polaritons, with a 100 ps lifetime reported by Steger *et al.,* led to the relatively low group velocity of ~1.43 μm/ps. This is surpassed by the InGaAs waveguide polariton demonstrated by Walker *et al*. with propagation length of 280 μm thanks to its much higher group velocity of 26 μm/ps despite the shorter lifetime of 10.7 ps [188]. Similar waveguide scheme has been used to make polariton

propagation in the GaN platform with propagation length up to 100µm despite a polariton lifetime of 1 ps at cryogenic temperature [190]. Importantly, in 2017, Lerario *et al.* reported on polariton created from the strong coupling of organic excitons and with a Bloch surface wave which can propagate for hundreds of microns and exhibit important nonlinear behaviors [123]. Using similar photonic platform, Barachati *et al.* have demonstrated propagation of organic polariton at room temperature up to 60 µm [19].

There are two main challenges to obtain macroscopic propagation (>100µm) of polaritons with high excitonic fraction (W_X> 50%), so as to take advantage of the hybrid nature of these quasiparticles in novel communication devices. First, most of room temperature excitonic materials have lower quality in comparison to the traditional GaAs platform. This leads to substantial losses from nonradiative effects, as well as localized disorder structure which can induced back scattering and affect the polariton propagation [191]. Most critically, the thermal broadening of excitonic resonance at room temperature makes macroscopic propagation of highly excitonic polaritons extremely difficult. Indeed, let's take the case of PEPI-based polariton, the linewidth γ_X=30meV of perovskite excitons at room temperature suggests that the polaritons of W_X> 50% would have a minimum linewidth of γ_{pol}=15 meV (this value is achieved if the photonic cavity factor is infinite and if there is no other loss sources). This linewidth corresponds to a polariton lifetime τ=43 fs, leading to a propagation length less than L=1.3 µm for a typical guided mode group velocity v_g=30 µm/ps.

To deal with the quality of excitonic materials, we will adopt the thermal imprinting method presented in chapter 2 to achieve large-scale surface (few millimeters) with overly good homogeneity subwavelength patterned surface. Moreover, the thermal broadening of perovskite excitons can be solved by exploiting an elegant effect of strong coupling physics itself: if the Rabi splitting is high enough, polaritons will be completely isolated from thermal

perturbation [193]. (See Appendix D)

5.2. Polaritonic modes in large surface nano-imprinted perovskite

Large surface with overall good homogeneity of pillar lattice PEPI metasurfaces were fabricated using thermal imprinting method (see detail in Chapter 2). PEPI was deposited on substrates made of 2 µm thick SiO_2 on Si, crystallized then imprinted with a hole-lattice Si mold forming a pillar lattice metasurface. Here we study a structure with period 300 nm and filling factor of 1. The thickness of PEPI estimated in total is around 110 nm with pattern thickness $t_{pattern} = 70\ nm$ and unpattern thickness $t_{slab} = 40\ nm$ (see Figure 5.1). The morphology of imprinted pattern metasurface has been presented in Chapter 2.2 with homogeneous pattern over few mm. This is expected to reduce the non-radiative loss of the emission, enhance the lifetime and propagation length of polariton and in the metasurface. In order to optimize the photon lifetime needed for macroscopic propagation, a maximum of filling factor has been chosen to optimize the photonic quality factor thanks to a weak modulation of the refractive index.

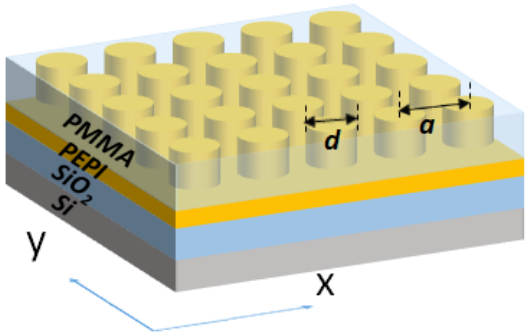

Figure 5.1. Sketch of the sample design. Here the perovskite pillar has diameter d=300nm and separated by the same distance a=300nm. The total thickness of perovskite layer is about 110nm, with pattern thickness of 70nm.

In this example, exciton-polariton features were studied by ARR, ARPL, and resonant scattering along ΓX direction. For the ARR and ARPL, the signals are analyzed in two different polarizations: E_y (i.e. S-polarization with respect to xz plane) and E_x (i.e. P-polarization with respect to xOz plane) (see Figure 5.2a,b). The resonant scattering results are obtained from cross-polarization measurement (excitation polarized along 45° and detection polarized along -

45° with respect to x-axis). This experiment reveals all radiative polaritonic modes and at the same time get rid of the background signal of specular reflection. Here we focus on the lower polaritonic modes of energy below the excitonic resonance (i.e. E_X=2.394 eV). As shown in Figures 5.2a and b, we observe 4 polaritonic modes: two dispersive modes LP_1 and LP_3; and two non-dispersive modes LP_2 and LP_4. The strong coupling regime between photonic Bloch resonances and PEPI exciton is evidenced by the bending of LP_1 branch when approaching the excitonic dispersion.

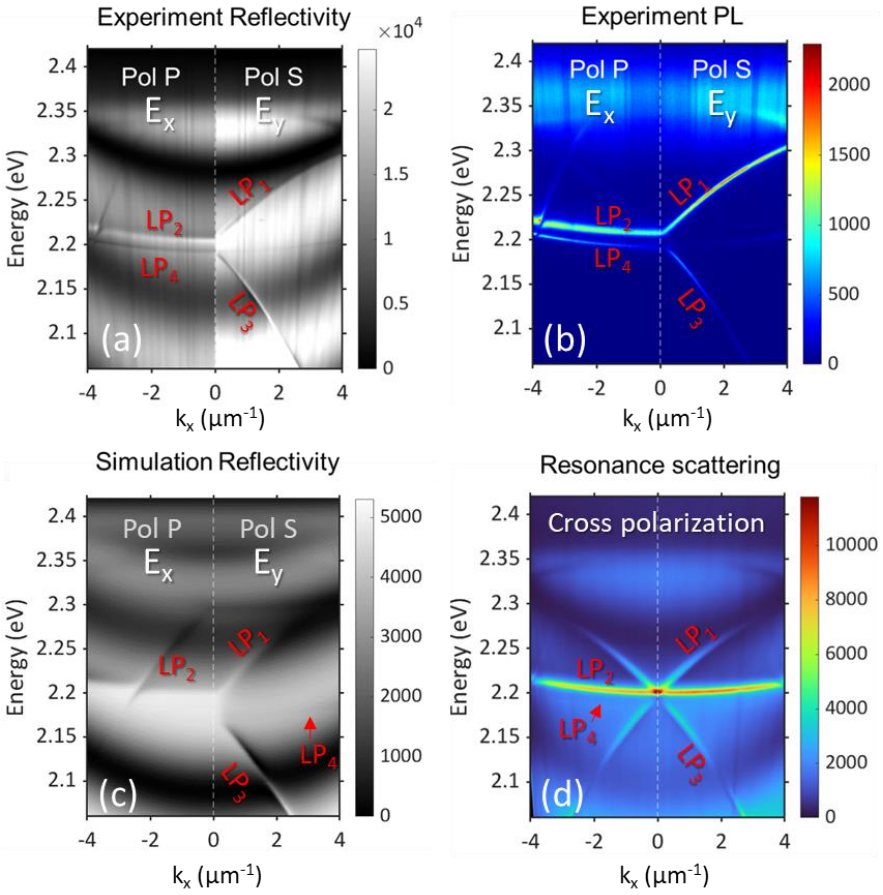

Figure 5.2. ARR experimental results (a) in comparison with RCWA simulation results (b) in P- and S-Polarization, resonance scattering characterization result (c) without polarization selection, experimental ARPL in S- and P-Polarization (d).

From these results one can see that LP_3 and LP_4 exhibit symmetry-protected BIC (the polaritonic resonances vanish locally the Γ point), corresponding to infinite radiative lifetime

(see Chapter 4). However, these points are not suited for studying polariton propagation since they have zero group velocity. In general, both LP_2 and LP_4 are not suited for studying polariton propagation due to their low group velocity, and the propagation with LP_3 mode is not very interesting because this mode is almost a photonic mode. Therefore, we will focus on the polaritons in the LP_1 mode for studying propagation along x-direction. In the following, we will study in detail this mode to have all needed parameters for the propagation experiment.

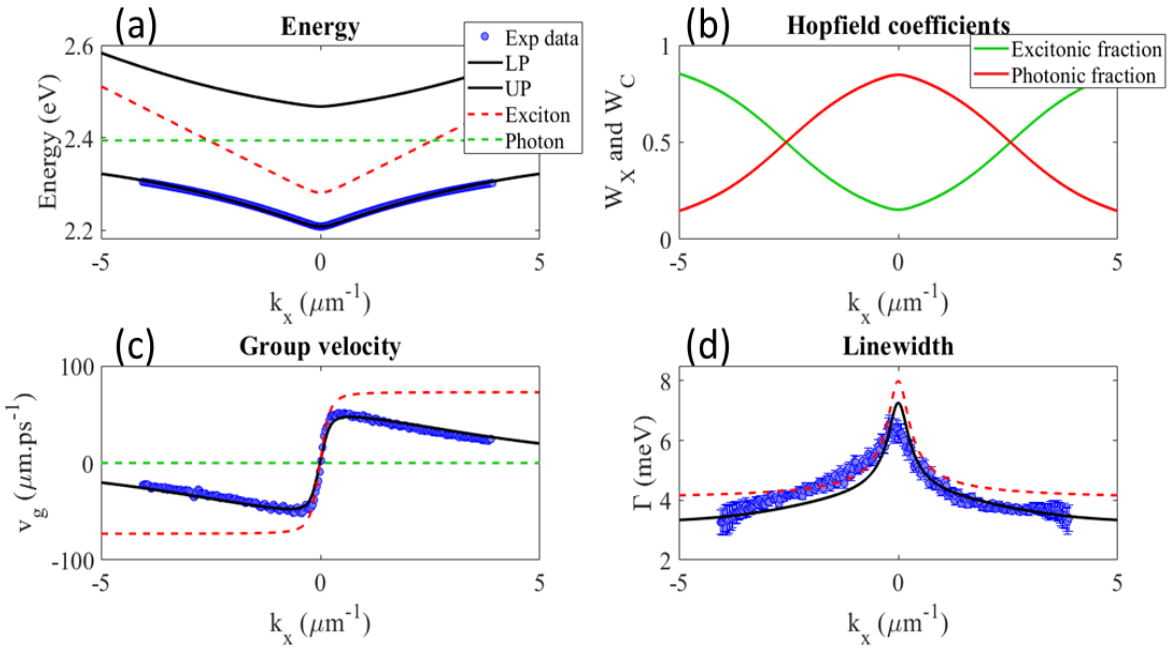

Figure 5.3. Energy peak position (a), Hopfield coefficients (b), group velocity (c) and linewidth (d) of the polaritonic branch LP_1. Blue dots are extracted data from ARPL, red-dash lines and green-dash lines are the theoretical values for photonic and excitonic resonance respectively. Black lines are theoretical curves for polaritonic modes.

Figure 5.3 presents the energy position, group velocity and linewidth of LP_1 that are extracted from ARPL experiments. The results are nicely fitted by the coupled oscillator model presented in section 1.3 of Chapter 1, in which the complex photonic mode is given by [94]:

$$\tilde{E}_c(k_x) = E_0 + i\gamma_c + \sqrt{(vk_x)^2 + (\mathrm{U} + i\gamma_c)^2} \qquad \text{(eq.5.1)}$$

Here E_0=2279 meV and v=48μm/ps are the energy and the group velocity of TE guided photonic mode at propagation constant 2π/a in the unpatterned PEPI slab. U=10 meV is the coupling strength between counter-propagating guided modes in presence of the periodic corrugation. γ_c=4 meV corresponds to the radiative losses of guided modes once brought above the light line via band folding mechanisms. The photon energy (linewidth) is then given by the real (imaginary) part of $\tilde{E}_C(k_x)$. From these results, we extract a Rabi splitting energy of $\hbar\Omega$ =230 meV (Figure 5.3a). The excitonic fraction reach 50% when wavevector k_x=2.6 μm^{-1} (Figure 5.3b), at which the polariton group velocity v_g=30μm/ps.

Intriguingly, the polariton linewidth gets narrower when the excitonic fraction increases (Figure 5.3d). At 50% excitonic fraction (k_x=2.6 μm^{-1}), the measured polariton linewidth is about 4meV, which is one order of magnitude smaller than the exciton linewidth (γ_X=30meV). This unusual narrowing of polariton linewidth is explained by the suppression of the thermal broadening for polaritonic states for high Rabi splitting energy. Indeed, as developed in details in the Appendix D, since the Rabi splitting energy is well above the energy E_{LO}~20meV of optical phonons in PEPI [69,194], the thermal broadening is quenched as long as polariton energy is bellow E_X-E_{LO}~2.37 eV [193]. As a consequence, the exciton linewidth in the coupled oscillator model is only given by the exciton linewidth Γ_0 (linewidth at 0K) and nonradiative losses γ_{nr} at 0K: $\Gamma_0 + \gamma_{nr}(0K)$. For the theoretical fitting shown in Figure 5.3d, we choose Γ_0 = 4 meV.

Finally, one may show that the C_4 symmetry of the structure leads to the same polaritonic dispersion along k_y but now polarized along E_x (S-polarization for the yz plane).

5.3. Polariton propagation in real space

In this section, we will present results of propagation experiment with ~50% excitonic

fraction polaritonic state. From the photoluminescence signal under non-resonant pumping (λ_{laser} = 405 nm, 80 MHz, 50 ps), this fraction is spectrally selected by using a spectral bandpass filter centered at λ_0 = 543 nm (E_0=2.283eV) (see Figure 5.4). This spectral filtering corresponds to an average wavevector of 2.8 μm^{-1} with excitonic fraction of 55%.

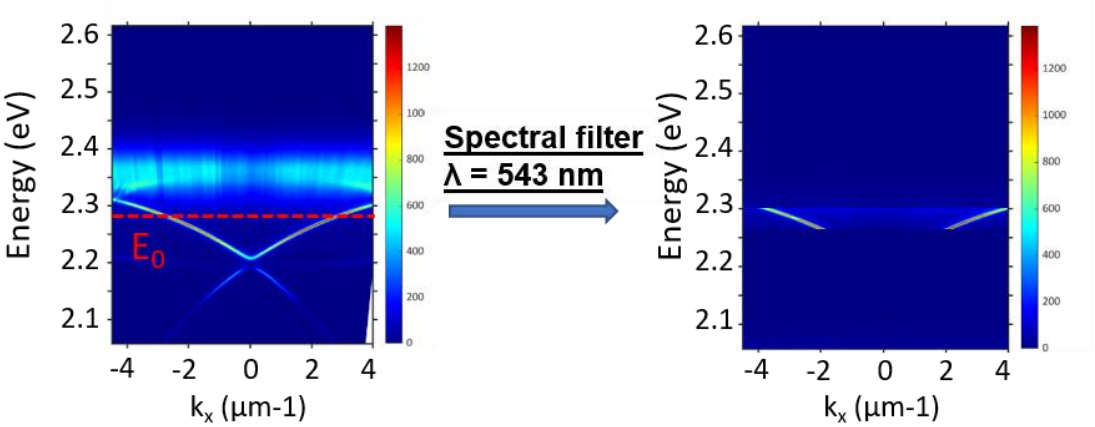

Figure 5.4. ARPL signal before and after spectral filtering

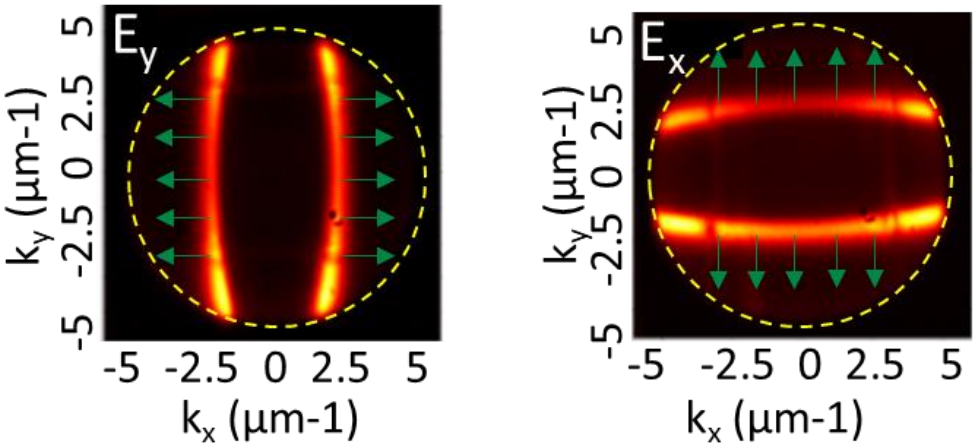

Figure 5.5. Iso-frequency wavevector dispersion of spectral filtered exciton-polaritons obtained from mapping the farfield emission polarized in E_y (left) and E_x (right) onto a SCMOS camera sensor. The green arrows indicate the group velocity patterns. The yellow dashed circles indicate the numerical aperture

Since the propagation direction is dictated by the group velocity vectors, it is crucial to investigate the group velocity pattern of the polaritons at the chosen energy before studying the propagation itself. This pattern can be directly visualize from the iso-frequency mapping of the

polaritonic modes. Indeed, the group velocity follows the normal direction of the iso-frequency curves because it is defined by the gradient of the energy surface in momentum space: $\vec{v}_g = \frac{1}{\hbar}\vec{g}rad_k E$. Figure 5.5 presents the measured iso-frequency map for different polarization selection, obtained by projecting the far-field photoluminescence emission onto a SCMOS camera sensor. Two polaritonic modes at this energy are revealed: one is polarized in E_y and only dispersive along k_x; the other one is polarized in E_x and only dispersive along k_y. These results are in good agreement with the observation in the previous section about the LP_1 mode and its twin in k_y direction. It shows that the dispersion in E_y polarization contains two curves nearly in parallel with each other along k_y, thus the group velocity pattern is uniformed and along x direction. Similarly, in polarization E_x, the group velocity pattern is uniformed and along y direction.

To demonstrate experimentally that the group velocity in each direction is constant, we perform ARPL measurements along k_x direction for different values of k_y. This has been done by shifting laterally the farfield photoluminescence image with respect to the entrance slit of the imaging spectrometer. Each image obtained in the CCD sensor, coupled to the output of the spectrometer, corresponds to a k_y "slice" of APRL along k_x [see Figure 5.6(a)]. From the measured dispersions, the group velocity and linewidth are extracted [Figure 5.6 (b-c)]. The estimated group velocity (v_g=30μm/ps) is independent of k_y which is consistent to the iso-frequency map. Moreover, the polariton linewidth also remains the same (γ_{pol}=4meV) for all k_y values.

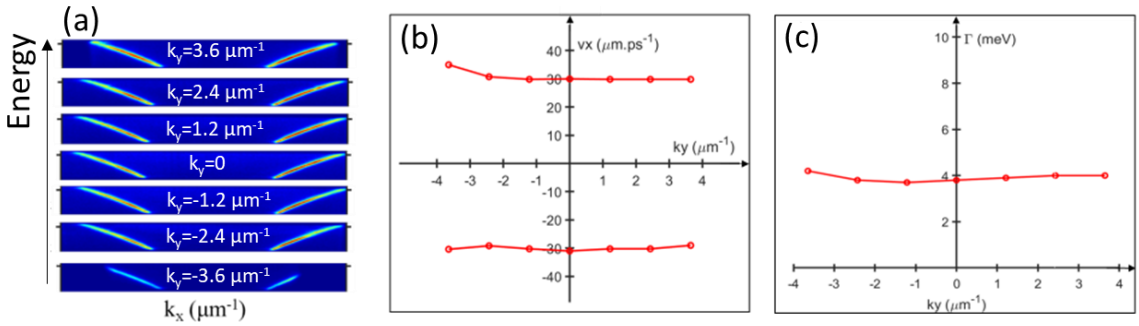

Figure 5.6. (a) Experimental results of ARPL along k_x in E_y polarization for different values of k_y. (b,c) Extracted of group velocity and linewidth from ARPL dispersion along k_y

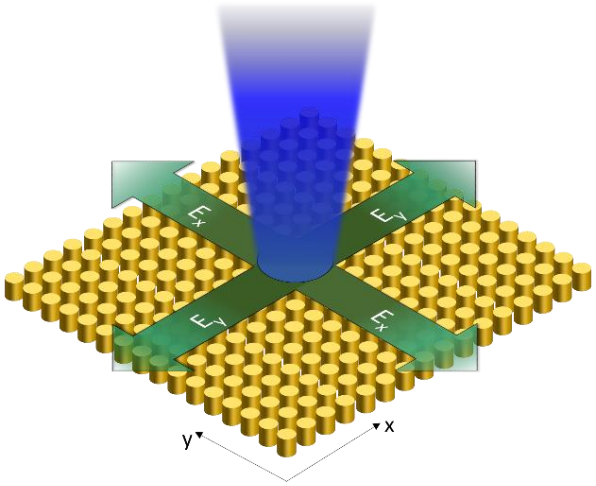

Figure 5.7. Sketch of the propagation scheme for polaritons at the selected energy. This consists of two unidimensional flows along x and y of the same group velocity v_g=30µm/ps but of different polarizations (green arrows). The blue beam indicates the excitation light.

From previous observations, we expect that the polariton propagation in the 2D metasurface consists of two unidimensional flows of uniform group velocity along x and y directions and of orthogonal polarizations (see Figure 5.7). Such a propagation scenario is experimentally demonstrated by visualizing the farfield image in real space. Figure 5.8(a) presents the spectrally filtered photoluminescence image in real space, measured in E_y polarization. In this experiment, the non-resonant pumping of ~2-3 µm diameter is focalized at x=y=0. It shows clearly that polaritons are locally injected at x=y=0 under the pump spot and propagate along x axis. Strikingly, even at x=80µm away from the pumping spot, the polariton flow still stay tightly confined along y direction within the pump spot (Figure 5.8a). This observation confirms that the velocity vector is only along x direction. Evidently, by changing

the polarization between E_y and E_x, we can choose to have propagation along x or y direction.

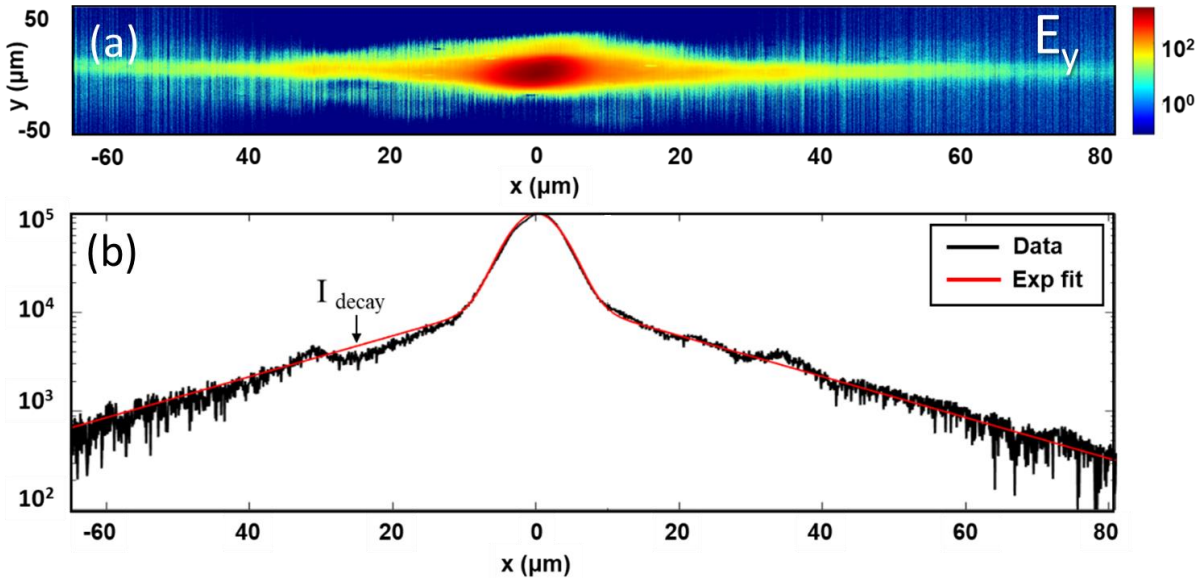

Figure 5.8. (a) Spatially resolved photoluminescence image of the polaritonic states filtered at 543nm, with E_y polarization selection. (b) Intensity profile selected at y=0. The black line is the experimental data, the red line is the fitting results using (eq 5.2)

To evaluate quantitatively the propagation properties, the intensity profile at y=0 is extracted from the photoluminescence image (see Figure 5.8b). We still have part of PEPI uncoupled excitonic resonance around the excitation center. This is due to the fact that bare PEPI excitons has relatively broad linewidth, and the tail of its emission cannot be totally filtered out in the detection. Still, these excitons possess effective mass and no velocity that make them unable to propagate. As shown in Figure 5.8, the excitonic reservoir can be observed only within the excitation spot. Hence, it is safe to confirm that the PL signal detected away from the pumping spot purely responds to the propagated polariton.

The PL intensity are then fitted using two components: a Gaussian in the middle displays the excitonic reservoir, and only outside we have propagation of polariton which is fitted by an exponential decay curve:

$$I(x) = I_0 e^{-x^2/2w^2} + I_1 e^{|-x|/L} \quad \text{(Eq 5.2)}$$

Where x is the distance from the pumping, w is the size of the pumping spot and L is the decay length where PL intensity decreased by a factor of e^{-1}. By fitting this model, we estimated propagation constant L= 21 µm and the pumping spot size w≈ 3.5 µm ($I_0 = 85 \cdot 10^3, I_1 = 15 \cdot 10^3$) . This value of decay length corresponds to a polariton lifetime of 0.7 ps if we assume that the propagation is ballistic. This lifetime corresponds to a homogenous linewidth of 0.94 meV. We note that this linewidth is much smaller than the value 4meV measured from ARPL experiment. Therefore the measured polariton linewidth rom ARPL is mostly dominant by inhomogeneous effect.

To sum up, under non-resonant excitation, we detected unidimensional PL signal of 50% excitonic-fraction polaritons over 80 µm away from the pumping spot and the exponential decay of the PL signal display a propagation length of 21 µm. However, the ballistic character of this exciton-polariton propagation remains unknown. Indeed, as it has been demonstrated by Hou et al. in propagation experiment with organic polaritons that the decay length may substantially different from the propagation length when there is backscattering due to disorders and energy transferring [191].

5.3. Exciton-polaritons propagation in k-space

To investigate the ballistic nature of our polariton propagation, the propagation is now monitored in the momentum space to probe possible backscattering. To do so, a slit of S=17µm width, playing the role of a spatial filter, is put at the intermediate image position in the optical path of the ARPL experiment setup. By moving the slit position along x-axis, we can probe the polariton dispersion under or far from the excitation spot. In this experiment, the spectral filter from the previous experiment is removed. The experimental results corresponding to three different slit positions are shown in Figure 5.9.

Under the pumping spot (x=0), the ARPL results show all polaritonic branches which were previously discussed in section 5.2. One may note that all branches are broadened

compared to the ones measured without spatial filter [see Figure 5.2(b)]. This is due to an uncertainty on the emitted wavevector $\Delta k_x=1/S$ introduced by the spatial filter. Moreover, the intensity distribution is very different from the one measured without the spatial filter: the strongest signals are observed from the uncoupled excitons and zero-group velocity point in polariton branches. Indeed, polaritons/excitons injected in these states cannot propagate and would radiatively emit photoluminescence under the pump spot, while states of non-zero group velocity would propagate out of the pump spot.

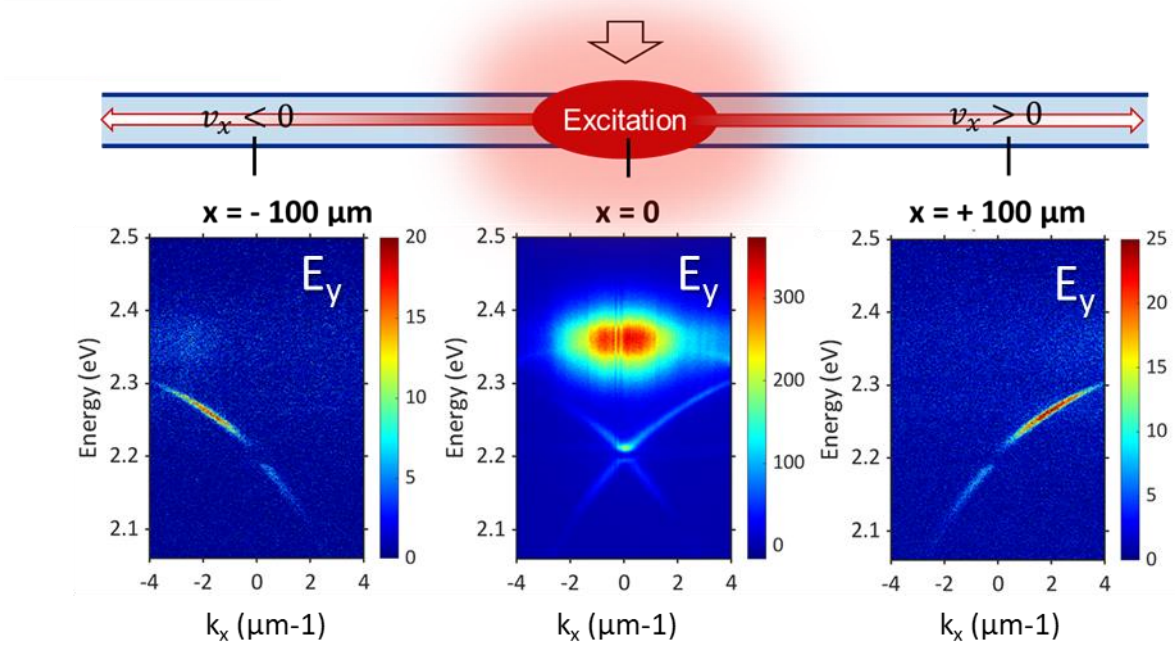

Figure 5.9. Spatially filtered ARPL measurements at three different positions along the propagation x-axis s: x = + 100 µm, x = - 100 µm and x = 0 (pumping spot)

At x = +(-) 100 µm away from the excitation, only polaritonic states at positive(negative) group velocity is observed. This observation demonstrates clearly that polaritons propagated ballistically throughout two sides of x axis with no sign of backscattering. Moreover, thanks to the absence of the signal from uncoupled excitons, we can now observe much more clearly a narrowing of polariton branch when approaching the excitonic energy. This confirms again our interpretation on the quenching of the thermal broadening. Most impressively, this propagation

across 100 µm is observed even with polarions at k_x=4 µm^{-1}, corresponding to an excitonic fraction of 75%. Since the extracted lifetime for polariton state of 55% excitonic fraction is 0.7 ps, and is only limited by the photonic losses (see Appendix D), we estimate that the lifetime of 75% excitonic fraction polaritons one is about 1.26 ps.

5.4 Conclusion of the chapter

In conclusion, we have demonstrated experimentally the ballistic propagation of exciton polaritons within the patterned PEPI metasurface. Room temperature exciton polaritons are populated via non-resonant laser excitation and detected at distance 100 µm with no back scattering. Impressively, the propagation is observed even with an excitonic fraction as high as 75%. Such performance is achieved thanks to the quenching of the thermal broadening for PEPI polaritons, combined with high quality of the large scale perovskite imprinted structures.

CONCLUSION

This work explored a new platform to make exciton polaritons called excitonic metasurface. We have experimentally demonstrated the strong coupling between guided resonances of 2D subwavelength lattices and exciton resonance of PEPI perovskite. Consequently, exciton-polaritons were created, observed at room temperature, exhibiting remarkable binding energy of around 200 meV in all of our samples. These results were revealed by angle-resolved reflectivity and angle-resolved photoluminescence and perfectly reproduced by numerical simulation.

Taking the advances in photonic crystal physics, our design of subwavelength excitonic metasurfaces have proved to offer a high degree of freedom to modulate polariton dispersions. Indeed, our results showed that, by simply changing the symmetry parameters of the lattice, polaritons can be tailored on demand into:

- Linear dispersion: exhibiting high group velocity, up to 126 μm/ps, which is desired to study polariton ballistic propagation for signal transmitting devices.
- Slow-light dispersion, with a parabolic shape and high polariton density of states at k=0, as the group velocity approaches zero. This regime would enhance Bose-Einstein condensation or could be suited to study polariton nonlinear effect.
- Multi-valley dispersion, i.e. W-shape with two minima off-Γ which; this could be the building block of polariton valleytronic physics.

Additionally, we have investigated experimentally the formation of exciton-polaritons resulting from the mixing at room temperature between PEPI excitons and an optical BIC of the subwavelength-scale metasurface. At that moment, these polariton BICs were revealed for the 1st time, with reflectivity, resonant scattering and photoluminescence measurements. Although pol-BICs only exhibit a finite quality factor bounded by the non-radiative losses of

the excitonic component, it fully inherits BIC's peculiar features: a total uncoupling to the radiative continuum associated with a local vanishing of the far-field radiation in the momentum space. Most importantly, our experimental results confirm that the topological nature of the photonic BIC is perfectly transferred to the pol-BICs. This is evidenced by the observation of the polarization vortex in the far-field of polaritonic emission.

At the beginning of this thesis, I started to fabricate PEPI metasurfaces by filling PEPI inside pre-patterned SiO2 backbones using spin coating. This technique requires simple implementation allowing to fabricate multiple structures quickly. Our results on dispersion engineering were obtained from infiltrated PEPI/SiO2 metasurfaces. However, we faced a challenge to reproduce the design and to obtain large homogeneous surface due to the limited control of PEPI infiltration. The thermal imprinting process was then developed in order to fabricate a uniform metasurface with quality enhancement, better control and high reproducibility. Large-scale homogeneous PEPI metasurfaces were produced to study polariton propagation. Within these metasurfaces, polaritons propagating ballistically were detected at a distance of 100 µm away from the excitation spot with no backscattering. Interestingly, these propagating polaritons possess an excitonic fraction as high as 75%.

Finally, we have investigated the polariton dispersion engineering at room temperature by patterning PEPI excitonic material into subwavelength periodic structures. Our design is compact, straightforward, works in the subwavelength regime, and provides a high degree of freedom for dispersion engineering thanks to the rich confinement schemes of metasurfaces. Our approach is naturally in the scheme of integrated optics, and perfectly adapted for large-scale fabrication methods such as nanoimprint and solution spincoating. It thus would pave the way for making low-cost integrated polaritonic devices operating at room temperature.

On the more fundamental side, perspectives include the demonstration of key physical phenomena such as polariton scattering, and Bose-Einstein condensation at room temperature which could benefit from the excitonic metasurfaces designed and fabricated using the approaches developed in this thesis.

APPENDICES

Appendix A: Optical characterization setup

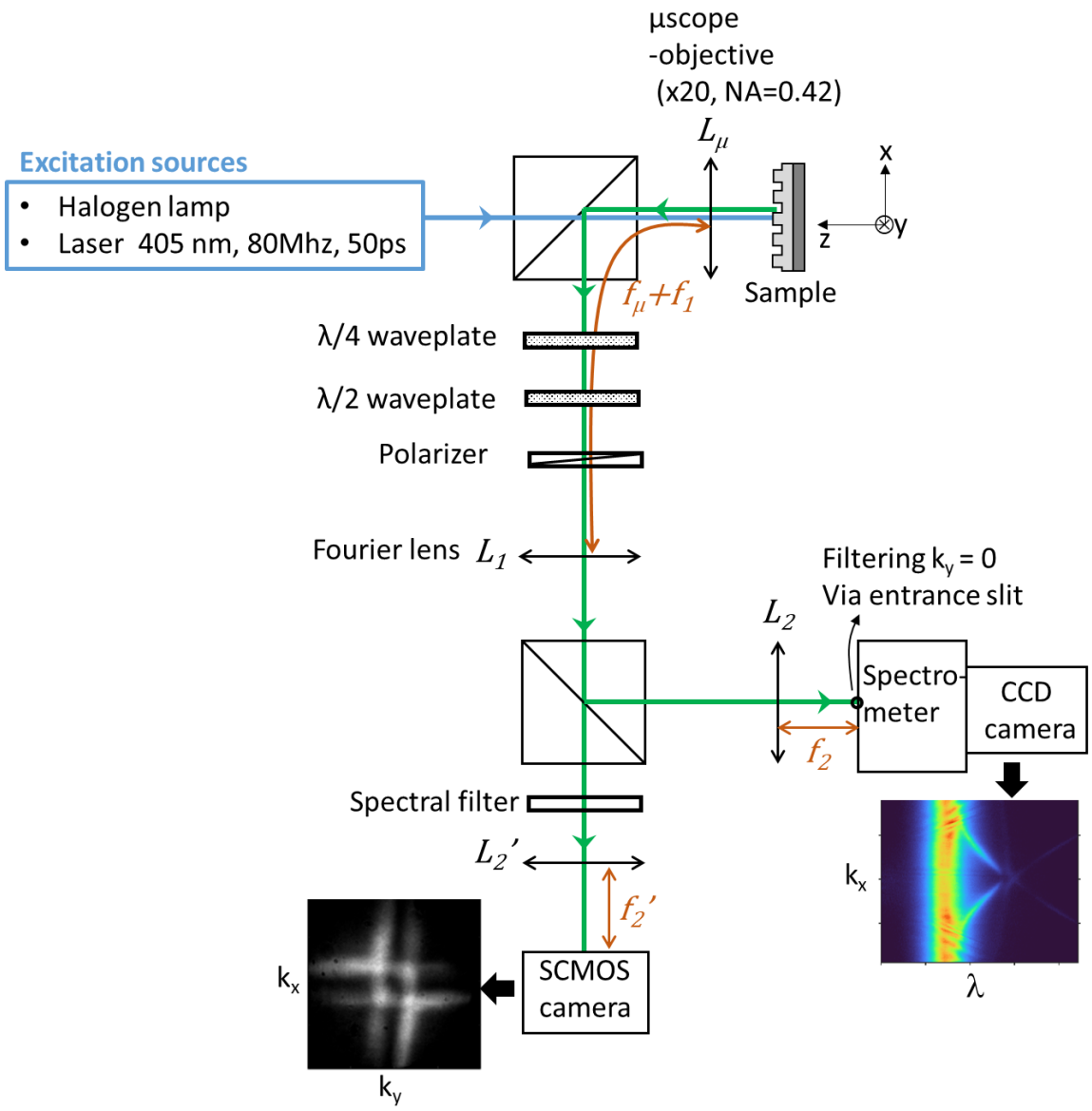

Appendix B: Numerical simulations of the strong coupling between photonic Bloch modes and PEPI exciton

We show here the numerical simulation results of active structure of PEPI metasurface (designed in Chapter 3) showing the effects of lattice parameters on polaritonic dispersion

- The effect of aspect ratio d/a on dispersion

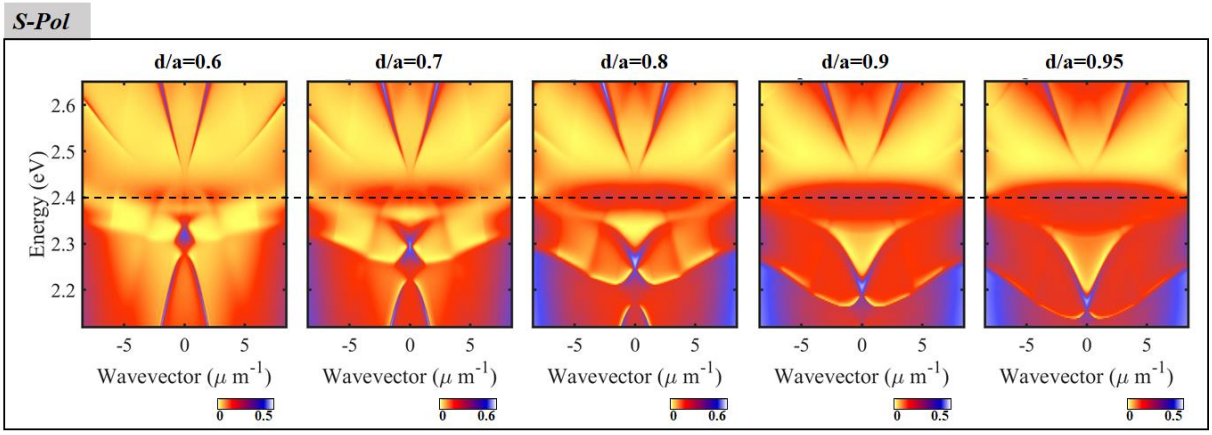

B1. Numerical simulation in S-polarization of the active structure of PEPI 2D lattice metasurfaces for different d/a values with fixed period a=350nm and PEPI thickness t_{PEPI}=50nm

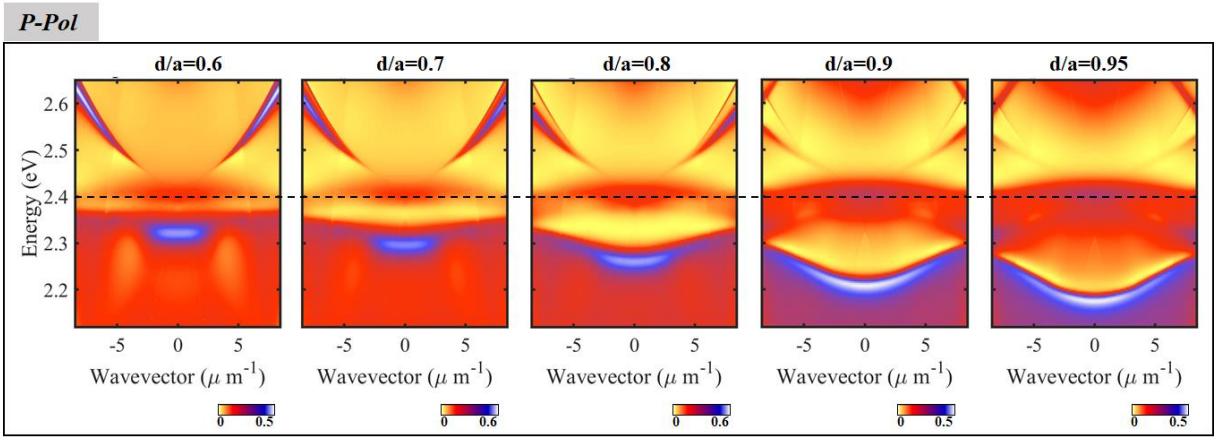

B2. Numerical simulation P-polarization of the active structure of PEPI 2D lattice metasurfaces for different d/a values with fixed period a=350nm and PEPI thickness t_{PEPI}=50nm

- The effect of PEPI thickness on dispersion

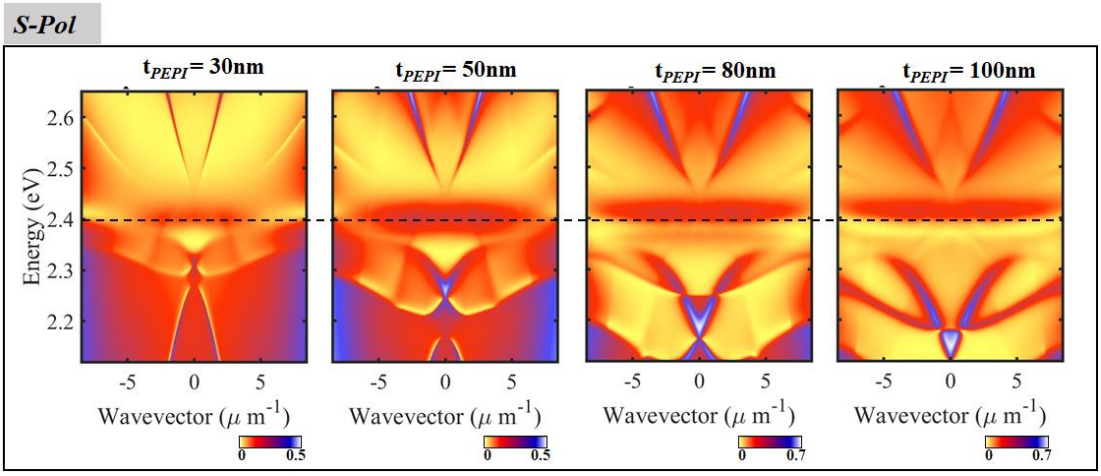

B3. Numerical simulation in S-polarization of the active structure of PEPI 2D lattice metasurfaces for different values of PEPI thickness with fixed period a=350nm and d/a=0.8

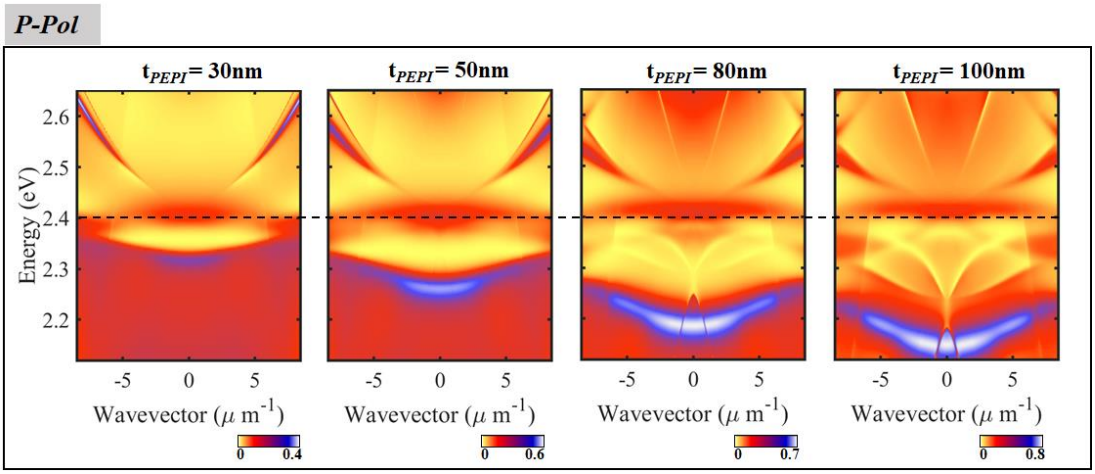

B4. Numerical simulation in P-polarization of the active structure of PEPI 2D lattice metasurfaces for different values of PEPI thickness with fixed period a=350nm and d/a=0.8

Appendix C: Topological nature of photonic BIC

More details on the topological nature of the two BIC states (BIC_1 and BIC_2) in chapter 4 are shown here. The topological charge of the BIC depends on the symmetry of the photonic modes at the Γ point, as given by irreducible representation ('irrep') of the point group. This is demonstrated in the figure C1: the BIC_1 state, which is the one considered in chapter 4 of the manuscript, corresponds to irrep B of the $\mathbf{C_4}$ point group, as seen by the transformation properties of the electric field components ($C_4E = -E$, where C_4 is a rotation by 90 degrees), and it has a topological charge q=-1. To give an example of different symmetry, BIC_2 corresponds to irrep A ($C_4E = +E$) and it has a topological charge q=+1. The value of the topological charges follow from the phase maps of the polarization field, as shown in the figure C2.

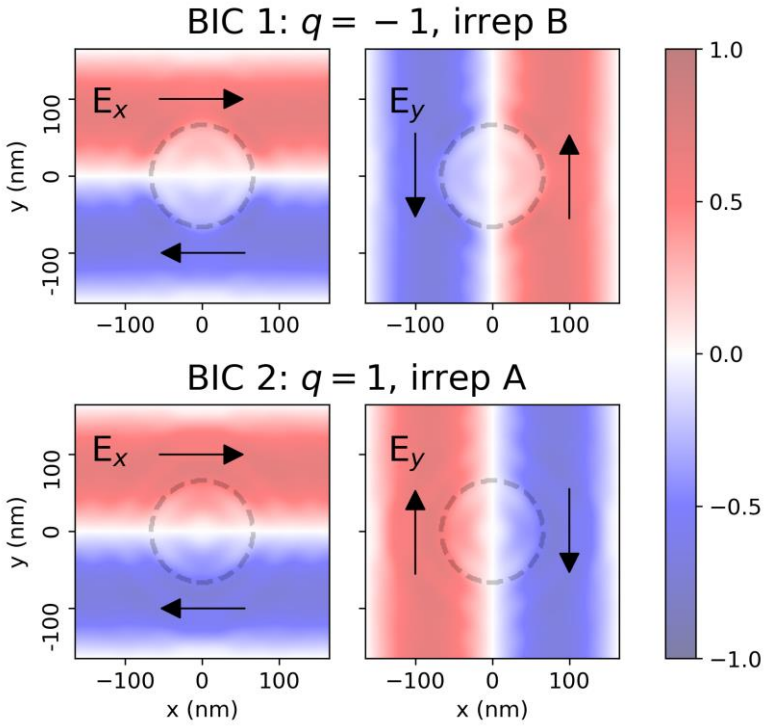

Figure C1. Symmetry properties of BIC_1 and BIC_2.

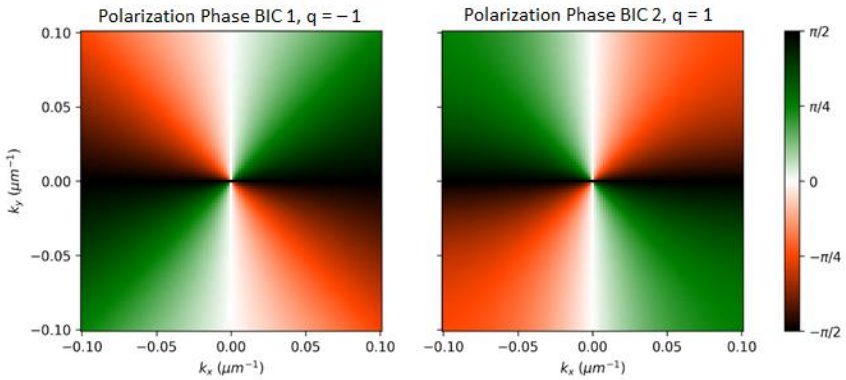

Figure C2. Polarization orientation of BIC_1 and BIC_2

Appendix D: Polaritonic linewidth in a nutshell

Due to the exciton-phonon couplings, the broadening of excitonic linewidth γ_X as a function of temperature is given by:

$$\gamma_x(T) = \Gamma_0 + \alpha T + \frac{\gamma_{LO}}{exp\left(\frac{E_{LO}}{k_B T}\right) - 1} \quad \text{(eq.1.1)}$$

Where Γ_0 is the linewidth at T=0K, taking into account γ_0 – the homogeneous linewidth at T=0K, and γ_{ih} – the inhomogeneous broadening. The linear term αT is the broadening due to couplings between excitons and acoustical phonons, and the last term corresponds to the broadening due to couplings between excitons and optical phonons of energy E_{LO}.

The homogeneous linewidth γ_0 is given by both radiative and nonradiative dephasing mechanism at 0K. For the case of 2D hybrid perovskite, a lower limit of lifetime τ_0 >100ps has been obtained by time-resolved photoluminescence at low temperature [195] That suggest an upper limit $\gamma_0 < 0.065$ meV. Temperature dependent spectroscopy on PEPI [69,194,196] determine an optical phonons energy E_{LO}~20 meV, Γ_0~25 meV and α~0.03meV/K. Moreover, these author also suggest that Γ_0 (the linewidth at 0K) is mainly due to inhomogeneous broadening, with values of ~3-10 meV depending on the fabrication. Using these values, one may estimate γ_X ~ 33-40meV at room temperature, which is in good agreement with our excitonic model of γ_X =30meV.

The damped coupled oscillator model (see Section 1.3 of Chapter 1) suggests that polariton linewidth is given by an average of the excitonic linewidth γ_X and the photonic linewidth γ_C:

$$\gamma_{pol} = W_C.\gamma_C + W_X.\gamma_X \quad \text{(eq.1.2)}$$

where W_C and W_X are the photonic and excitonic fractions respectively. This simple expression

perfectly captures the hybrid nature of exciton-polaritons and has been widely used to study strong coupling regime physics in both cryogenic and room temperature. Using this model, we expect that for PEPI-based polaritonic state of 50% excitonic fraction, the polariton linewidth has a lower limit of 15 meV at room temperature. This value is much higher than 4meV that is experimentally measured in Chapter 5 for PEPI metasurface. Moreover, from the propagation experiment of Chapter 5, we extract a polariton lifetime of 0.7 ps. That corresponds to a homogenous linewidth of 0.94 meV for PEPI-based polaritonic state of 50% excitonic.

In the following, we will discuss how the simple expression of (eq.1.2) fails to describe the polariton linewidth of PEPI metasurface at room temperature. Indeed, in this formulation, excitons were first coupled to phonons, leading to its thermal broadening, then coupled to photons to make exciton-polaritons. However, as explained by Savona and Piermarocchi [197], this interpretation is in general incorrect since exciton-photon interaction is order of magnitude stronger than exciton-phonons. Thus polaritons are first created from photons and "isolated" excitons, and the thermal broadening is due to polariton-phonon interaction but not exciton-phonon interaction. As a consequence, the polariton linewidth is correctly given by:

$$\gamma_{pol}(T) = W_c\gamma_c + W_x\Gamma_0 + \gamma_T(T) \qquad \text{(eq. 1.3)}$$

where $\gamma_T(T)$ is the thermal broadening issues from polariton-phonon interactions.

Interestingly, as theoretically suggested and experimentally demonstrated by Trichet *et al*. [193], the thermal broadening can be completely quenched if polariton modes are "protected" from the bare exciton modes by an energy larger than E_{LO}: $E_{pol} < E_X - E_{LO}$. For the case of polaritons with 50% exciton fraction, thermal broadening is completely quenched if half of the Rabi splitting energy exceeds the LO phonon energy:

$$\frac{\hbar\Omega}{2} > E_{LO} \qquad \text{(eq. 1.4)}$$

This condition is difficult to be satisfied for III-V semiconductor but can be meet for materials with stronger oscillator strength such as PEPI. Indeed, for the case of polariton in PEPI metasurface, the Rabi splitting $\hbar\Omega \sim 200$ meV and largely exceeds the LO phonon energy. Thus for PEPI polaritons, we can safely assume that $\gamma_T = 0$.

Finally, considering that the thermal broadening is quenched for PEPI polaritons, the expression of PEPI polaritonic linewidth is reduced to:

$$\gamma_{pol} = W_C . \gamma_C + W_X . \Gamma_0 \qquad \text{(eq. 1.5)}$$

Therefore, **the polariton linewidth is still given by the expression from coupled damped oscillators, but the exciton contribution is the excitonic linewidth at 0K. Consequently, since the polariton lifetime is given by the homogeneous linewidth γ_0, we have:**

$$\tau = \frac{\hbar}{W_C . \gamma_{C,h} + W_X . \gamma_0} \qquad \text{(eq. 1.6)}$$

where $\gamma_{C,h}$ is the photon homogenous linewidth. Since $\gamma_0 < 0.065$ meV, we can safely suppose that in general polariton lifetime only depends on the photonic component:

$$\tau = \frac{\hbar}{W_C . \gamma_{C,h}} \qquad \text{(eq. 1.7)}$$

However, for the case of polariton BIC, the photon homogenous linewidth is strictly zero, thus the polariton lifetime is dictated by the excitonic losses:

$$\tau_{pol-BIC} = \frac{\hbar}{W_X . \gamma_0} \qquad \text{(eq. 1.8)}$$

BIBLIOGRAPHY

[1] A. M. Fox, *Optical Properties of Solids* (Oxford University Press, 2001).

[2] K. W. Böer and U. W. Pohl, *Semiconductor Physics* (Springer, Cham, 2020).

[3] A. Kavokin, Baumberg J., G. Malpuech, and F. P. Laussy, *Microcavities* (2006).

[4] D. Bajoni, J. Phys. D. Appl. Phys. **45**, (2012).

[5] M. Wouters and I. Carusotto, Phys. Rev. B **75**, 75332 (2007).

[6] C. Weisbuch, M. Nishioka, A. Ishikawa, and Y. Arakawa, Phys. Rev. Lett. **69**, 3314 (1992).

[7] D. Sanvitto and S. Kéna-Cohen, Nat. Mater. **15**, 1061 (2016).

[8] S. Christopoulos, G. B. H. Von Högersthal, a. J. D. Grundy, P. G. Lagoudakis, a. V Kavokin, J. J. Baumberg, G. Christmann, R. Butté, E. Feltin, J. F. Carlin, and N. Grandjean, Phys. Rev. Lett. **98**, 1 (2007).

[9] K. S. Daskalakis, P. S. Eldridge, G. Christmann, E. Trichas, R. Murray, E. Iliopoulos, E. Monroy, N. T. Pelekanos, J. J. Baumberg, and P. G. Savvidis, Appl. Phys. Lett. **102**, (2013).

[10] M. Zamfirescu, A. Kavokin, B. Gil, G. Malpuech, and M. Kaliteevski, Phys. Rev. B **65**, 161205 (2002).

[11] H. Franke, C. Sturm, R. Schmidt-Grund, G. Wagner, and M. Grundmann, New J. Phys. **14**, 13037 (2012).

[12] D. G. Lidzey, D. D. C. Bradley, M. S. Skolnick, T. Virgili, S. Walker, and D. M. Whittaker, Nature **395**, 53 (1998).

[13] N. Takada, T. Kamata, and D. D. C. Bradley, Appl. Phys. Lett. **82**, 1812 (2003).

[14] R. J. Holmes and S. R. Forrest, Phys. Rev. Lett. **93**, 186404 (2004).

[15] X. Liu, T. Galfsky, Z. Sun, F. Xia, E. Lin, Y.-H. Lee, S. Kéna-Cohen, and V. M. Menon, Nat. Photonics **9**, 30 (2014).

[16] G. Grosso, Nat. Photonics **11**, 455 (2017).

[17] S. Dufferwiel, T. P. Lyons, D. D. Solnyshkov, A. A. P. Trichet, A. Catanzaro, F. Withers, G. Malpuech, J. M. Smith, K. S. Novoselov, M. S. Skolnick, D. N. Krizhanovskii, and A. I.

Tartakovskii, Nat. Commun. **9**, 4797 (2018).

[18] R. Gogna, W. Burg, E. Tutuc, and H. Deng, Nat. Commun. 1 (2018).

[19] F. Barachati, A. Fieramosca, S. Hafezian, J. Gu, B. Chakraborty, D. Ballarini, L. Martinu, V. Menon, D. Sanvitto, and S. Kéna-Cohen, Nat. Nanotechnol. **13**, 906 (2018).

[20] J. Zhao, R. Su, A. Fieramosca, W. Zhao, W. Du, X. Liu, C. Diederichs, D. Sanvitto, T. C. H. Liew, and Q. Xiong, Nano Lett. **21**, 3331 (2021).

[21] R. Su, C. Diederichs, J. Wang, T. C. H. Liew, J. Zhao, S. Liu, W. Xu, Z. Chen, and Q. Xiong, Nano Lett. **17**, 3982 (2017).

[22] R. Su, J. Wang, J. Zhao, J. Xing, W. Zhao, C. Diederichs, T. C. H. Liew, and Q. Xiong, Sci. Adv. **4**, (2018).

[23] R. Su, S. Ghosh, J. Wang, S. Liu, C. Diederichs, T. C. H. Liew, and Q. Xiong, Nat. Phys. (2020).

[24] W. Du, S. Zhang, J. Shi, J. Chen, Z. Wu, Y. Mi, Z. Liu, Y. Li, X. Sui, R. Wang, X. Qiu, T. Wu, Y. Xiao, Q. Zhang, and X. Liu, ACS Photonics **5**, 2051 (2018).

[25] W. Bao, X. Liu, F. Xue, F. Zheng, R. Tao, S. Wang, Y. Xia, M. Zhao, J. Kim, S. Yang, Q. Li, Y. Y. Wang, Y. Y. Wang, L.-W. Wang, A. H. MacDonald, and X. Zhang, Proc. Natl. Acad. Sci. **116**, 20274 LP (2019).

[26] Q. Han, J. Wang, J. Lu, L. Sun, F. Lyu, H. Wang, Z. Chen, and Z. Wang, ACS Photonics **7**, 454 (2020).

[27] G. Lanty, S. Zhang, J. S. Lauret, E. Deleporte, P. Audebert, S. Bouchoule, X. Lafosse, J. Zuñiga-Pérez, F. Semond, D. Lagarde, F. Médard, and J. Leymarie, Phys. Rev. B - Condens. Matter Mater. Phys. **84**, 1 (2011).

[28] V. Savona, C. Piermarocchi, A. Quattropani, F. Tassone, and P. Schwendimann, Phys. Rev. Lett. **78**, 4470 (1997).

[29] D. M. Whittaker, P. Kinsler, T. A. Fisher, M. S. Skolnick, A. Armitage, A. M. Afshar, J. S. Roberts, G. Hill, and M. A. Pate, Superlattices Microstruct. **22**, 91 (1997).

[30] T. Freixanet, B. Sermage, A. Tiberj, and R. Planel, Phys. Rev. B **61**, 7233 (2000).

[31] R. Huang, Y. Yamamoto, R. Andre, J. Bleuse, M. Muller, and H. Ulmer-Tuffigo, in *Tech. Dig. Summ. Pap. Present. Quantum Electron. Laser Sci. Conf. Postconf. Tech. Dig. (IEEE Cat. No.01CH37172)* (2001), pp. 100–101.

[32] A. Brehier, R. Parashkov, J. S. Lauret, and E. Deleporte, Appl. Phys. Lett. **89**, 23 (2006).

[33] J. Wenus, R. Parashkov, S. Ceccarelli, A. Brehier, J. S. Lauret, M. S. Skolnick, E. Deleporte, and D. G. Lidzey, Phys. Rev. B - Condens. Matter Mater. Phys. **74**, 1 (2006).

[34] a. Amo, J. Lefrere, S. Pigeon, C. Adrados, C. Ciuti, I. Carusotto, R. Houdre, E. Giacobino, and A. Bramati, Nat. Phys. **5**, 14 (2008).

[35] G. Lanty, J. S. Lauret, E. Deleporte, S. Bouchoule, and X. Lafosse, J. Lumin. **129**, 1985 (2009).

[36] M. Galbiati, L. Ferrier, D. D. Solnyshkov, D. Tanese, E. Wertz, A. Amo, M. Abbarchi, P. Senellart, I. Sagnes, A. Lema\^\itre, E. Galopin, G. Malpuech, and J. Bloch, Phys. Rev. Lett. **108**, 126403 (2012).

[37] T. Jacqmin, I. Carusotto, I. Sagnes, M. Abbarchi, D. D. Solnyshkov, G. Malpuech, E. Galopin, A. Lemaître, J. Bloch, and A. Amo, Phys. Rev. Lett. **112**, 116402 (2014).

[38] V. G. Sala, D. D. Solnyshkov, I. Carusotto, T. Jacqmin, A. Lemaître, H. Terças, A. Nalitov, M. Abbarchi, E. Galopin, I. Sagnes, J. Bloch, G. Malpuech, and A. Amo, Phys. Rev. X **5**, 11034 (2015).

[39] F. Baboux, L. Ge, T. Jacqmin, M. Biondi, E. Galopin, A. Lema\^\itre, L. Le Gratiet, I. Sagnes, S. Schmidt, H. E. Türeci, A. Amo, and J. Bloch, Phys. Rev. Lett. **116**, 66402 (2016).

[40] P. St-Jean, V. Goblot, E. Galopin, A. Lemaître, T. Ozawa, L. Le Gratiet, I. Sagnes, J. Bloch, and A. Amo, Nat. Photonics **11**, 651 (2017).

[41] C. E. Whittaker, E. Cancellieri, P. M. Walker, D. R. Gulevich, H. Schomerus, D. Vaitiekus, B. Royall, D. M. Whittaker, E. Clarke, I. V Iorsh, I. A. Shelykh, M. S. Skolnick, and D. N. Krizhanovskii, Phys. Rev. Lett. **120**, 97401 (2018).

[42] D. Tanese, H. Flayac, D. Solnyshkov, A. Amo, A. Lemaître, E. Galopin, R. Braive, P. Senellart, I. Sagnes, G. Malpuech, and J. Bloch, Nat. Commun. **4**, (2013).

[43] D. Gerace and L. C. Andreani, Phys. Rev. B **75**, 235325 (2007).

[44] D. Bajoni, D. Gerace, M. Galli, J. Bloch, R. Braive, I. Sagnes, A. Miard, A. Lemaître, M. Patrini, and L. Claudio Andreani, Phys. Rev. B **80**, (2009).

[45] V. Kravtsov, E. Khestanova, F. A. Benimetskiy, T. Ivanova, A. K. Samusev, I. S. Sinev, D. Pidgayko, A. M. Mozharov, I. S. Mukhin, M. S. Lozhkin, Y. V Kapitonov, A. S. Brichkin, V. D. Kulakovskii, I. A. Shelykh, A. I. Tartakovskii, P. M. Walker, M. S. Skolnick, D. N. Krizhanovskii, and I. V Iorsh, Light Sci. Appl. **9**, 56 (2020).

[46] T. Fujita, Y. Sato, T. Kuitani, and T. Ishihara, Phys. Rev. B **57**, 12428 (1998).

[47] J. Ishi-Hayase and T. Ishihara, Semicond. Sci. Technol. **18**, (2003).

[48] K. Sumioka, H. Nagahama, and T. Tsutsui, Appl. Phys. Lett. **78**, 1328 (2001).

[49] S. A. Kulkarni, S. G. Mhaisalkar, N. Mathews, and P. P. Boix, **1800231**, 1 (2019).

[50] A. Perumal, S. Shendre, M. Li, Y. K. E. Tay, V. K. Sharma, S. Chen, Z. Wei, Q. Liu, Y. Gao, P. J. S. Buenconsejo, S. T. Tan, C. L. Gan, Q. Xiong, T. C. Sum, and H. V. Demir, Sci. Rep. **6**, 36733 (2016).

[51] W. Deng, X. Xu, X. Zhang, Y. Zhang, X. Jin, L. Wang, S.-T. Lee, and J. Jie, Adv. Funct. Mater. **26**, 4797 (2016).

[52] H. Huang, F. Zhao, L. Liu, F. Zhang, X. Wu, L. Shi, B. Zou, Q. Pei, and H. Zhong, ACS Appl. Mater. Interfaces **7**, 28128 (2015).

[53] F. Deschler, M. Price, S. Pathak, L. E. Klintberg, D.-D. Jarausch, R. Higler, S. Hüttner, T. Leijtens, S. D. Stranks, H. J. Snaith, M. Atatüre, R. T. Phillips, and R. H. Friend, J. Phys. Chem. Lett. **5**, 1421 (2014).

[54] H. Zhu, Y. Fu, F. Meng, X. Wu, Z. Gong, Q. Ding, M. V Gustafsson, M. T. Trinh, S. Jin, and X.-Y. Zhu, Nat. Mater. **14**, 636 (2015).

[55] Q. Zhang, S. T. Ha, X. Liu, T. C. Sum, and Q. Xiong, Nano Lett. **14**, 5995 (2014).

[56] G. Grancini and G. Grancini, Photoniques 24 (2019).

[57] K. Park, J. W. Lee, J. D. Kim, N. S. Han, D. M. Jang, S. Jeong, J. Park, and J. K. Song, J. Phys. Chem. Lett. **7**, 3703 (2016).

[58] R. Su, C. Diederichs, J. Wang, T. C. H. Liew, J. Zhao, S. Liu, W. Xu, Z. Chen, Q. Xiong, A.

Fieramosca, L. De Marco, M. Passoni, L. Polimeno, A. Rizzo, B. L. T. Rosa, G. Cruciani, L. Dominici, M. De Giorgi, G. Gigli, L. C. Andreani, D. Gerace, D. Ballarini, and D. Sanvitto, Nano Lett. **17**, 3982 (2017).

[59] Q. Shang, S. Zhang, Z. Liu, J. Chen, P. Yang, C. Li, W. Li, Y. Zhang, Q. Xiong, X. Liu, and Q. Zhang, Nano Lett. **18**, 3335 (2018).

[60] S. Zhang, Q. Shang, W. Du, J. Shi, Z. Wu, Y. Mi, J. Chen, F. Liu, Y. Li, M. Liu, Q. Zhang, and X. Liu, Adv. Opt. Mater. **6**, 1 (2018).

[61] X. Wang, M. Shoaib, X. Wang, X. Zhang, M. He, Z. Luo, W. Zheng, H. Li, T. Yang, X. Zhu, L. Ma, and A. Pan, ACS Nano **12**, 6170 (2018).

[62] T. J. S. Evans, A. Schlaus, Y. Fu, X. Zhong, T. L. Atallah, M. S. Spencer, L. E. Brus, S. Jin, and X. Y. Zhu, Adv. Opt. Mater. **6**, 1 (2018).

[63] P. Bouteyre, H. S. Nguyen, J. S. Lauret, G. Trippé-Allard, G. Delport, F. Lédée, H. Diab, A. Belarouci, C. Seassal, D. Garrot, F. Bretenaker, and E. Deleporte, ACS Photonics **6**, 1804 (2019).

[64] E. B. Kim, M. S. Akhtar, H. S. Shin, S. Ameen, and M. K. Nazeeruddin, J. Photochem. Photobiol. C Photochem. Rev. **48**, 100405 (2021).

[65] Y. Pan, Y. Zhang, W. Kang, N. Deng, Z. Yan, W. Sun, X. Kang, and J. Ni, Mater. Adv. **1**, (2022).

[66] T. Ishihara, J. Lumin. **60**–**61**, 269 (1994).

[67] A. Fieramosca, L. De Marco, M. Passoni, L. Polimeno, A. Rizzo, B. L. T. Rosa, G. Cruciani, L. Dominici, M. De Giorgi, G. Gigli, L. C. Andreani, D. Gerace, D. Ballarini, and D. Sanvitto, ACS Photonics **5**, 4179 (2018).

[68] X. Hong, T. Ishihara, and A. V Nurmikko, Phys. Rev. B **45**, 6961 (1992).

[69] K. Gauthron, J.-S. Lauret, L. Doyennette, G. Lanty, A. Al Choueiry, S. J. Zhang, A. Brehier, L. Largeau, O. Mauguin, J. Bloch, and E. Deleporte, Opt. Express **18**, 5912 (2010).

[70] S. Zhang, P. Audebert, Y. Wei, A. Al Choueiry, G. Lanty, A. Bréhier, L. Galmiche, G. Clavier, C. Boissière, J. S. Lauret, and E. Deleporte, Materials (Basel). **3**, 3385 (2010).

[71] K. Abdel-Baki, F. Boitier, H. Diab, G. Lanty, K. Jemli, F. Lédée, D. Garrot, E. Deleporte, and J. S. Lauret, J. Appl. Phys. **119**, 1 (2016).

[72] M. Shimizu and T. Ishihara, Appl. Phys. Lett. **80**, 2836 (2002).

[73] A. Brehier, R. Parashkov, J. S. Lauret, and E. Deleporte, Appl. Phys. Lett. **89**, 23 (2006).

[74] G. Lanty, J. S. Lauret, E. Deleporte, S. Bouchoule, and X. Lafosse, Appl. Phys. Lett. **93**, 8 (2008).

[75] G. Lanty, A. Bréhier, R. Parashkov, J.-S. Lauret, and E. Deleporte, New J. Phys. **10**, 65007 (2008).

[76] K. Pradeesh, J. J. Baumberg, and G. V. Prakash, Opt. Express **17**, 22171 (2009).

[77] G. Lanty, J. S. Lauret, E. Deleporte, S. Bouchoule, and X. Lafosse, J. Lumin. **129**, 1985 (2009).

[78] Y. Wei, J. S. Lauret, L. Galmiche, P. Audebert, and E. Deleporte, Opt. Express **20**, 10399 (2012).

[79] Z. Han, H.-S. Nguyen, F. Boitier, Y. Wei, K. Abdel-Baki, J.-S. Lauret, J. Bloch, S. Bouchoule, and E. Deleporte, Opt. Lett. **37**, 5061 (2012).

[80] H. S. Nguyen, Z. Han, K. Abdel-Baki, X. Lafosse, A. Amo, J. S. Lauret, E. Deleporte, S. Bouchoule, and J. Bloch, Appl. Phys. Lett. **104**, 1 (2014).

[81] S. Bouchoule, K. Abdel-Baki, J. Bloch, Z. Han, E. Deleporte, H.-S. Nguyen, F. Réveret, and J.-S. Lauret, Appl. Phys. Express **6**, 106701 (2013).

[82] F. Lédée, G. Trippé-Allard, H. Diab, P. Audebert, D. Garrot, J. S. Lauret, and E. Deleporte, CrystEngComm **19**, 2598 (2017).

[83] A. Fieramosca, L. Polimeno, V. Ardizzone, L. De Marco, M. Pugliese, V. Maiorano, M. De Giorgi, L. Dominici, G. Gigli, D. Gerace, D. Ballarini, and D. Sanvitto, Sci. Adv. **5**, (2019).

[84] P. Bermel, C. Luo, L. Zeng, L. C. Kimerling, and J. D. Joannopoulos, Opt. Express **15**, 16986 (2007).

[85] D. Zhou and R. Biswas, J. Appl. Phys. **103**, 93102 (2008).

[86] T. N. Oder, K. H. Kim, J. Y. Lin, and H. X. Jiang, Appl. Phys. Lett. **84**, 466 (2004).

[87] J. J. Wierer, A. David, and M. M. Megens, Nat. Photonics **3**, 163 (2009).

[88] A. A. Erchak, D. J. Ripin, S. Fan, P. Rakich, J. D. Joannopoulos, E. P. Ippen, G. S. Petrich, and L. A. Kolodziejski, Appl. Phys. Lett. **78**, 563 (2001).

[89] S. L. Portalupi, M. Galli, C. Reardon, T. F. Krauss, L. O'Faolain, L. C. Andreani, and D. Gerace, Opt. Express **18**, 16064 (2010).

[90] M. Imada, S. Noda, A. Chutinan, T. Tokuda, M. Murata, and G. Sasaki, Appl. Phys. Lett. **75**, 316 (1999).

[91] V. Liu and S. Fan, Comput. Phys. Commun. **183**, 2233 (2012).

[92] C. W. Hsu, B. Zhen, A. D. Stone, J. D. Joannopoulos, and M. Soljačić, Nat. Rev. Mater. **1**, 16048 (2016).

[93] H. Friedrich and D. Wintgen, Phys. Rev. A **32**, 3231 (1985).

[94] L. Lu, Q. Le-Van, L. Ferrier, E. Drouard, C. Seassal, and H. S. Nguyen, Photonics Res. **8**, A91 (2020).

[95] B. Zhen, C. W. Hsu, L. Lu, A. D. Stone, and M. Soljačić, Phys. Rev. Lett. **113**, 1 (2014).

[96] N. Pourdavoud, S. Wang, A. Mayer, T. Hu, Y. Chen, A. Marianovich, W. Kowalsky, R. Heiderhoff, H. C. Scheer, and T. Riedl, Adv. Mater. **29**, 1605003 (2017).

[97] K. Chen, S. Schünemann, S. Song, and H. Tüysüz, Chem. Soc. Rev. **47**, 7045 (2018).

[98] Z. Y. Cheng, Z. Wang, R. B. Xing, Y. C. Han, and J. Lin, Chem. Phys. Lett. **376**, 481 (2003).

[99] M. E. Calvo, J. Mater. Chem. A **5**, 20561 (2017).

[100] A. Mayer, M. Buchmüller, S. Wang, C. Steinberg, M. Papenheim, H.-C. Scheer, N. Pourdavoud, T. Haeger, and T. Riedl, J. Vac. Sci. Technol. B, Nanotechnol. Microelectron. Mater. Process. Meas. Phenom. **35**, 06G803 (2017).

[101] S. Chen, K. Roh, J. Lee, W. K. Chong, Y. Lu, N. Mathews, T. C. Sum, and A. Nurmikko, ACS Nano **10**, 3959 (2016).

[102] A. L. Yablonskii, E. A. Muljarov, N. A. Gippius, S. G. Tikhodeev, T. Fujita, and T. Ishihara, J. Phys. Soc. Japan **70**, 1137 (2001).

[103] S. Schünemann, K. Chen, S. Brittman, E. Garnett, and H. Tüysüz, ACS Appl. Mater. Interfaces **8**, 25489 (2016).

[104] H. Wang, R. Haroldson, B. Balachandran, A. Zakhidov, S. Sohal, J. Y. Chan, A. Zakhidov, and W. Hu, ACS Nano **10**, 10921 (2016).

[105] M. E. Kamminga, H.-H. Fang, M. A. Loi, G. H. ten Brink, G. R. Blake, T. T. M. Palstra, and J. E. ten Elshof, ACS Appl. Mater. Interfaces **10**, 12878 (2018).

[106] J. Feng, X. Yan, Y. Zhang, X. Wang, Y. Wu, B. Su, H. Fu, and L. Jiang, Adv. Mater. **28**, 3732 (2016).

[107] N. Zhang, W. Sun, S. P. Rodrigues, K. Wang, Z. Gu, S. Wang, W. Cai, S. Xiao, and Q. Song, Adv. Mater. **29**, (2017).

[108] P. Brenner, M. Stulz, D. Kapp, T. Abzieher, U. W. Paetzold, A. Quintilla, I. A. Howard, H. Kalt, and U. Lemmer, Appl. Phys. Lett. **109**, (2016).

[109] C. T. O. Wong, E. H. Sargent, B. R. Sutherland, S. Hoogland, and M. M. Adachi, ACS Nano **8**, 10947 (2014).

[110] S. Schünemann, S. Brittman, K. Chen, E. C. Garnett, and H. Tüysüz, ACS Photonics **4**, 2522 (2017).

[111] Y. Wei, P. Audebert, L. Galmiche, J. S. Lauret, and E. Deleporte, Materials (Basel). **7**, 4789 (2014).

[112] D. B. Mitzi, M. T. Prikas, and K. Chondroudis, Chem. Mater. **11**, 542 (1999).

[113] K. A. Baki, Ultrafast Spectroscopy of 2D Hybrid Perovskites, Ecole normale superieure de Cachan - ENS Cachan, 2014.

[114] Z. Wang, Z. Zhang, L. Xie, S. Wang, C. Yang, and C. Fang, **2101822**, (2022).

[115] H. Ding, Advanced Photonic Crystal Assisted Thin Film Solar Cells : From Order to Pseudo-Disorder, 2016.

[116] J. Liu, P. Kleimann, G. Laffite, C. Jamois, and R. Orobtchouk, Appl. Phys. Lett. **106**, 0 (2015).

[117] F. BERRY, Nanostructuration et Cristaux Photo- Niques à Base de Pérovskites Hybrides Pour Applications Photovoltaïques, 2020.

[118] P. Scarfato, N. Schiavone, G. Rossi, and L. Incarnato, Polymers (Basel). **11**, (2019).

[119] E. P. Plueddemann, *Silane Coupling Agents* (Springer New York, NY, 2013).

[120] D. G. Lidzey, D. D. C. Bradley, T. Virgili, A. Armitage, M. S. Skolnick, and S. Walker, Phys. Rev. Lett. **82**, 3316 (1999).

[121] J. D. Plumhof, T. Stöferle, L. Mai, U. Scherf, and R. F. Mahrt, Nat. Mater. **13**, 247 (2014).

[122] V. M. Agranovich, M. Litinskaia, and D. G. Lidzey, Phys. Rev. B **67**, 85311 (2003).

[123] G. Lerario, D. Ballarini, A. Fieramosca, A. Cannavale, A. Genco, F. Mangione, S. Gambino, L. Dominici, M. De Giorgi, G. Gigli, and D. Sanvitto, Light Sci. Appl. **6**, e16212 (2017).

[124] O. Jamadi, F. Reveret, P. Disseix, F. Medard, J. Leymarie, A. Moreau, D. Solnyshkov, C. Deparis, M. Leroux, E. Cambril, S. Bouchoule, J. Zuniga-Perez, and G. Malpuech, Light Sci. Appl. **7**, 82 (2018).

[125] H. Franke, C. Sturm, R. Schmidt-Grund, G. Wagner, and M. Grundmann, New J. Phys. **14**, 13037 (2012).

[126] Y. Wang, T. Hu, W. Xie, L. Sun, L. Zhang, J. Wang, J. Gu, L. Wu, J. Wang, X. Shen, and Z. Chen, Phys. Rev. B - Condens. Matter Mater. Phys. **91**, 1 (2015).

[127] M. Sun, I. G. Savenko, H. Flayac, and T. C. H. Liew, Sci. Rep. **7**, 45243 (2017).

[128] D. V Karpov and I. G. Savenko, New J. Phys. **20**, 13037 (2018).

[129] Y. Zheng, S. Feng, and S. J. Yang, Phys. Rev. A **97**, 1 (2018).

[130] J. Hou, X.-W. Luo, K. Sun, T. Bersano, V. Gokhroo, S. Mossman, P. Engels, and C. Zhang, Phys. Rev. Lett. **120**, 120401 (2018).

[131] J. J. Baumberg, P. G. Savvidis, R. M. Stevenson, A. I. Tartakovskii, M. S. Skolnick, D. M. Whittaker, and J. S. Roberts, Phys. Rev. B **62**, R16247 (2000).

[132] L. Lu, Q. Le-Van, L. Ferrier, E. Drouard, C. Seassal, and H. S. Nguyen, Photonics Res. **8**, A91 (2020).

[133] I. A. M. Al-Ani, K. As'Ham, L. Huang, A. E. Miroshnichenko, W. Lei, and H. T. Hattori, Adv. Opt. Mater. **10**, 2101120 (2022).

[134] J. Von Neumann and E. Wigner, Z. Phys **30**, 465 (1929).

[135] S. I. Azzam and A. V Kildishev, Adv. Opt. Mater. **9**, 2001469 (2021).

[136] A. Kodigala, T. Lepetit, Q. Gu, B. Bahari, Y. Fainman, and B. Kanté, Nature **541**, 196 (2017).

[137] J. Jin, X. Yin, L. Ni, M. Soljačić, B. Zhen, and C. Peng, Nature **574**, 501 (2019).

[138] M. Wu, S. T. Ha, S. Shendre, E. G. Durmusoglu, W.-K. Koh, D. R. Abujetas, J. A. Sánchez-Gil, R. Paniagua-Domínguez, H. V. Demir, and A. I. Kuznetsov, Nano Lett. **20**, 6005 (2020).

[139] C. Huang, C. Zhang, S. Xiao, Y. Wang, Y. Fan, Y. Liu, N. Zhang, G. Qu, H. Ji, J. Han, L. Ge, Y. Kivshar, and Q. Song, Science (80-.). **367**, 1018 (2020).

[140] M.-S. Hwang, H.-C. Lee, K.-H. Kim, K.-Y. Jeong, S.-H. Kwon, K. Koshelev, Y. Kivshar, and H.-G. Park, Nat. Commun. **12**, 4135 (2021).

[141] S. Romano, G. Zito, S. Torino, G. Calafiore, E. Penzo, G. Coppola, S. Cabrini, I. Rendina, and V. Mocella, Photon. Res. **6**, 726 (2018).

[142] S. D. Krasikov, A. A. Bogdanov, and I. V Iorsh, Phys. Rev. B **97**, 224309 (2018).

[143] M. Minkov, D. Gerace, and S. Fan, Optica **6**, 1039 (2019).

[144] V. A. Zakharov and A. N. Poddubny, Phys. Rev. A **101**, 43848 (2020).

[145] J. Wang, M. Clementi, M. Minkov, A. Barone, J.-F. Carlin, N. Grandjean, D. Gerace, S. Fan, M. Galli, and R. Houdré, Optica **7**, 1126 (2020).

[146] H. M. Doeleman, F. Monticone, W. den Hollander, A. Alù, and A. F. Koenderink, Nat. Photonics **12**, 397 (2018).

[147] Y. Zhang, A. Chen, W. Liu, C. W. Hsu, B. Wang, F. Guan, X. Liu, L. Shi, L. Lu, and J. Zi, Phys. Rev. Lett. **120**, 186103 (2018).

[148] B. Wang, W. Liu, M. Zhao, J. Wang, Y. Zhang, A. Chen, F. Guan, X. Liu, L. Shi, and J. Zi, Nat. Photonics **14**, 623 (2020).

[149] X. Yin, J. Jin, M. Soljačić, C. Peng, and B. Zhen, (2019).

[150] W. Ye, Y. Gao, and J. Liu, Phys. Rev. Lett. **124**, 153904 (2020).

[151] T. Yoda and M. Notomi, Phys. Rev. Lett. **125**, 53902 (2020).

[152] K. L. Koshelev, S. K. Sychev, Z. F. Sadrieva, A. A. Bogdanov, and I. V Iorsh, Phys. Rev. B **98**, 161113 (2018).

[153] P. Xie, Z. Liang, T. Jia, D. Li, Y. Chen, P. Chang, H. Zhang, and W. Wang, Phys. Rev. B **104**, 125446 (2021).

[154] V. Ardizzone, F. Riminucci, S. Zanotti, A. Gianfrate, D. G. Suarez-Forero, F. Todisco, M. De Giorgi, D. Trypogeorgos, G. Gigli, H. S. Nguyen, K. Baldwin, L. Pfeiffer, D. Ballarini, D. Gerace, and D. Sanvitto, Nature **605**, 447 (2022).

[155] V. Ardizzone, L. De Marco, M. De Giorgi, L. Dominici, D. Ballarini, and D. Sanvitto, Nanophotonics (2019).

[156] S. G. Lee and R. Magnusson, Phys. Rev. B **99**, 1 (2019).

[157] L. C. Andreani and D. Gerace, Phys. Rev. B **73**, 235114 (2006).

[158] M. Minkov, I. A. D. Williamson, L. C. Andreani, D. Gerace, B. Lou, A. Y. Song, T. W. Hughes, and S. Fan, ACS Photonics **7**, 1729 (2020).

[159] N. H. M. Dang, D. Gerace, E. Drouard, G. Trippé-Allard, F. Lédée, R. Mazurczyk, E. Deleporte, C. Seassal, and H. S. Nguyen, Nano Lett. (2020).

[160] M. Galli, D. Bajoni, M. Belotti, F. Paleari, M. Patrini, G. Guizzetti, D. Gerace, M. Agio, L. C. Andreani, D. Peyrade, and Y. Chen, IEEE J. Sel. Areas Commun. **23**, 1402 (2005).

[161] M. W. McCutcheon, G. W. Rieger, I. W. Cheung, J. F. Young, D. Dalacu, S. Frédérick, P. J. Poole, G. C. Aers, and R. L. Williams, Appl. Phys. Lett. **87**, 221110 (2005).

[162] B. Schaefer, E. Collett, R. Smyth, D. Barrett, and B. Fraher, Am. J. Phys. **75**, 163 (2007).

[163] D. P. Biss, K. S. Youngworth, and T. G. Brown, Appl. Opt. **45**, 470 (2006).

[164] R. Chen, K. Agarwal, C. J. R. Sheppard, and X. Chen, Opt. Lett. **38**, 3111 (2013).

[165] K. S. Youngworth and T. G. Brown, Opt. Express **7**, 77 (2000).

[166] R. Dorn, S. Quabis, and G. Leuchs, Phys. Rev. Lett. **91**, 233901 (2003).

[167] T. Bauer, S. Orlov, U. Peschel, P. Banzer, and G. Leuchs, Nat. Photonics **8**, 23 (2014).

[168] Y. Kozawa and S. Sato, Opt. Express **18**, 10828 (2010).

[169] C. Min, Z. Shen, J. Shen, Y. Zhang, H. Fang, G. Yuan, L. Du, S. Zhu, T. Lei, and X. Yuan, Nat. Commun. **4**, 2891 (2013).

[170] Y. Zhao and J. Wang, Opt. Lett. **40**, 4843 (2015).

[171] G. Milione, T. A. Nguyen, J. Leach, D. A. Nolan, and R. R. Alfano, Opt. Lett. **40**, 4887 (2015).

[172] F. Cardano, E. Karimi, S. Slussarenko, L. Marrucci, C. de Lisio, and E. Santamato, Appl. Opt.

51, C1 (2012).

[173] A. Fieramosca, L. De Marco, M. Passoni, L. Polimeno, A. Rizzo, B. L. T. Rosa, G. Cruciani, L. Dominici, M. De Giorgi, G. Gigli, L. C. Andreani, D. Gerace, D. Ballarini, and D. Sanvitto, ACS Photonics **5**, 4179 (2018).

[174] T. Gao, P. S. Eldridge, T. C. H. Liew, S. I. Tsintzos, G. Stavrinidis, G. Deligeorgis, Z. Hatzopoulos, and P. G. Savvidis, Phys. Rev. B **85**, 235102 (2012).

[175] D. Ballarini, M. De Giorgi, E. Cancellieri, R. Houdré, E. Giacobino, R. Cingolani, A. Bramati, G. Gigli, and D. Sanvitto, Nat. Commun. **4**, 1778 (2013).

[176] A. Amo, S. Pigeon, D. Sanvitto, V. G. Sala, R. Hivet, I. Carusotto, F. Pisanello, G. Leménager, R. Houdré, E. Giacobino, C. Ciuti, and A. Bramati, Science (80-.). **332**, 1167 (2011).

[177] H. S. Nguyen, D. Vishnevsky, C. Sturm, D. Tanese, D. Solnyshkov, E. Galopin, A. Lemaître, I. Sagnes, A. Amo, G. Malpuech, and J. Bloch, Phys. Rev. Lett. **110**, 236601 (2013).

[178] A. Amo, J. Lefrère, S. Pigeon, C. Adrados, C. Ciuti, I. Carusotto, R. Houdré, E. Giacobino, and A. Bramati, Nat. Phys. **5**, 805 (2009).

[179] H. S. Nguyen, D. Gerace, I. Carusotto, D. Sanvitto, E. Galopin, A. Lemaître, I. Sagnes, J. Bloch, and A. Amo, Phys. Rev. Lett. **114**, 36402 (2015).

[180] G. Lerario, D. Ballarini, A. Fieramosca, A. Cannavale, A. Genco, F. Mangione, S. Gambino, L. Dominici, M. De Giorgi, G. Gigli, and D. Sanvitto, Light Sci. Appl. **6**, e16212 (2017).

[181] D. Liran, I. Rosenberg, K. West, L. Pfeiffer, and R. Rapaport, ACS Photonics **5**, 4249 (2018).

[182] T. Chervy, P. Knüppel, H. Abbaspour, M. Lupatini, S. Fält, W. Wegscheider, M. Kroner, and A. Imamoğlu, Phys. Rev. X **10**, 11040 (2020).

[183] E. Wertz, L. Ferrier, D. D. Solnyshkov, R. Johne, D. Sanvitto, A. Lemaâtre, I. Sagnes, R. Grousson, A. V. Kavokin, P. Senellart, G. Malpuech, and J. Bloch, Nat. Phys. **6**, 860 (2010).

[184] M. Steger, G. Liu, B. Nelsen, C. Gautham, D. W. Snoke, R. Balili, L. Pfeiffer, and K. West, Phys. Rev. B - Condens. Matter Mater. Phys. **88**, 15 (2013).

[185] T. Freixanet, B. Sermage, A. Tiberj, R. Planel, T. Freixanet, B. Sermage, A. Tiberj, and R. P. In-plane, Phys. Rev. B **61**, 7233 (2000).

[186] W. Langbein, I. Shelykh, D. Solnyshkov, G. Malpuech, Y. Rubo, and A. Kavokin, Phys. Rev. B **75**, 1 (2007).

[187] D. G. Suárez-Forero, V. Ardizzone, S. F. Covre da Silva, M. Reindl, A. Fieramosca, L. Polimeno, M. De Giorgi, L. Dominici, L. N. Pfeiffer, G. Gigli, D. Ballarini, F. Laussy, A. Rastelli, and D. Sanvitto, Light Sci. Appl. **9**, (2020).

[188] P. M. Walker, L. Tinkler, M. Durska, D. M. Whittaker, I. J. Luxmoore, B. Royall, D. N. Krizhanovskii, M. S. Skolnick, I. Farrer, and D. A. Ritchie, Appl. Phys. Lett. **102**, 1 (2013).

[189] F. Marsault, H. S. Nguyen, D. Tanese, A. Lemaître, E. Galopin, I. Sagnes, A. Amo, and J. Bloch, Appl. Phys. Lett. **107**, (2015).

[190] J. Ciers, J. G. Roch, J.-F. Carlin, G. Jacopin, R. Butté, and N. Grandjean, Phys. Rev. Appl. **7**, 34019 (2017).

[191] S. Hou, M. Khatoniar, K. Ding, Y. Qu, A. Napolov, V. M. Menon, and S. R. Forrest, Adv. Mater. **32**, 1 (2020).

[192] C. Zhang, C. L. Zou, Y. Yan, R. Hao, F. W. Sun, Z. F. Han, Y. S. Zhao, and J. Yao, J. Am. Chem. Soc. **133**, 7276 (2011).

[193] A. Trichet, L. Sun, G. Pavlovic, N. A. Gippius, G. Malpuech, W. Xie, Z. Chen, M. Richard, and L. S. Dang, Phys. Rev. B **83**, 41302 (2011).

[194] S. Neutzner, F. Thouin, D. Cortecchia, A. Petrozza, C. Silva, and A. R. Srimath Kandada, Phys. Rev. Mater. **2**, 64605 (2018).

[195] D. B. Straus, S. Hurtado Parra, N. Iotov, J. Gebhardt, A. M. Rappe, J. E. Subotnik, J. M. Kikkawa, and C. R. Kagan, J. Am. Chem. Soc. **138**, 13798 (2016).

[196] A. R. Srimath Kandada, H. Li, E. R. Bittner, and C. Silva-Acuña, J. Phys. Chem. C **126**, 5378 (2022).

[197] V. Savona and C. Piermarocchi, Phys. Stat. Sol. **164**, 45 (1997).

LIST OF PUBLICATIONS

1. N. H. M. Dang, D. Gerace, E. Drouard, G. Trippé-Allard, F. Lédée, R. Mazurczyk, E. Deleporte, C. Seassal, H. S. Nguyen.
   "Tailoring dispersion of room-temperature exciton-polaritons with perovskite-based subwavelength metasurfaces", ***Nano Lett.*** 20 (3), 2113-2119 (2020)

2. N. H. M. Dang, S. Zanotti, C. Chevalier, G. Trippé-Allard, E. Deleporte, M. Amara, V. Ardizzone, D. Sanvitto, L. C. Andreani, C. Seassal, D. Gerace, H. S. Nguyen
   "Realization of Polaritonic Topological Charge at Room Temperature Using Polariton Bound States in the Continuum from Perovskite Metasurface", ***Adv. Opt. Mater.*** 10, 2102386 (2022)

3. L. Ferrier, P. Bouteyre, A. Pick, S. Cueff, N. H. M. Dang, C. Diederichs, A. Belarouci, T. Benyattou, J. Zhao, R. Su, J. Xing, Q. Xiong, H. S. Nguyen
   "*Unveiling the Enhancement of Spontaneous Emission at Exceptional Points*", ***Phys. Rev. Lett.*** 129, 083602 (2022)

4. N. H. M. Dang, P. Bouteyre, G. Trippé-Allard, C. Chevalier, E. Deleporte, E. Drouard, C. Seassal, and H. S. Nguyen
   "*Nanoimprinted exciton-polaritons metasurfaces: cost-effective, large-scale, high homogeneity, and room temperature operation*", ***Opt. Mater. Express*** 14 (6), 1655-1669 (2024)

5. N. H. M. Dang, S. Zanotti, E. Drouard, C. Chevalier, G. Trippé-Allard, E. Deleporte, C. Seassal, D. Gerace, H. S. Nguyen

   "Long-range ballistic propagation of 80%-excitonic-fraction polaritons in a perovskite metasurface at room temperature", (2024), arXiv:2406.01271

RESUME EN FRANCAIS

INTRODUCTION

Les appareils numériques (téléphones, ordinateurs) sont devenus un élément indispensable de notre vie quotidienne. Ces dernières années, les besoins en dispositifs de traitement du signal se sont fortement accélérés parallèlement à l'explosion des innovations dans les technologies numériques telles qu'internet, l'intelligence artificielle et l'apprentissage automatique, la blockchain, la cybersécurité, etc. Cela conduit à l'envolée de la consommation d'énergie et augmente les impacts sur l'environnement. Pour faire face à ces problèmes, notre civilisation cherche maintenant sa prochaine révolution technologique avec des percées dans l'amélioration des performances, la réduction de la taille et la consommation d'énergie des dispositifs numériques. Cependant, la technologie utilisée - la microélectronique basée sur la technologie du silicium - le cœur de la production, est confrontée à des défis pour entrer dans cette révolution. Cela est dû à l'accélération de la complexité des dispositifs et au fait que l'évolution de la technologie des semi-conducteurs atteint les limites moléculaires.

Dans ce contexte, les dispositifs photoniques, qui utilisent des photons comme supports d'information à la place des électrons, sont apparus comme une solution pour résoudre le dilemme de la haute vitesse et de la faible consommation de leurs homologues électroniques. En effet, le monde est aujourd'hui connecté par un réseau internet véhiculant des signaux optiques dans des câbles de fibre optique. Néanmoins, l'interaction entre les photons, c'est-à-dire la non-linéarité photonique, est négligeable par rapport à l'interaction de Coulomb entre les électrons, ce qui limite les dispositifs photoniques pour le traitement proprement dit de l'information. En fait, les dispositifs numériques reposent toujours sur des composants électroniques (transistors, portes et commutateurs) pour traiter l'information. Cela nécessite une conversion aller-retour entre le signal optique et le signal électronique à l'interface fibre

optique-routeur, ce qui entraîne des pertes de données et une consommation d'énergie élevée.

Récemment, les excitons-polaritons sont apparus comme une plateforme prometteuse, combinant la force des systèmes photoniques et électroniques pour les futurs dispositifs numériques. Il s'agit de quasi-particules hybrides mi-matière, mi-lumière résultant du régime de couplage fort entre les excitations électroniques dans les semi-conducteurs, c'est-à-dire les excitons, et les photons confinés dans les cavités optiques. Grâce à leur nature hybride, ces quasi-particules présentent de faibles pertes, une vitesse de propagation élevée sur de longues distances à travers leur part photonique, et en même temps une forte non-linéarité héritée de leur part excitonique. Bien que de nombreux dispositifs polaritoniques tels que des mémoires, des transistors, des portes et des diodes polaritoniques aient été démontrés expérimentalement par différents groupes, ces dispositifs en sont encore au stade de la recherche en laboratoire. En effet, cette plateforme fascinante présente deux inconvénients majeurs : i) la plupart de ses développements ont été réalisés avec des semi-conducteurs à base de GaAs qui nécessitent un fonctionnement à température cryogénique pour les excitons, ainsi qu'une méthode de croissance coûteuse, ii) le principal schéma de confinement optique est une cavité verticale épaisse comportant de nombreuses couches, et n'est pas compatible avec la technologie CMOS mature développée pour la micro-électronique.

Dans cette thèse, nous nous attaquons aux deux principaux inconvénients des dispositifs polaritoniques conventionnels en proposant une nouvelle plateforme polarionique que nous appelons métasurface excitonique. Celle-ci consiste à nanostructurer un film mince semi-conducteur en métasurface résonante sub-longueur d'onde. Du côté des matériaux, la pérovskite hybride a été choisie en raison de ses excellentes caractéristiques excitoniques à température ambiante et de sa fabrication peu coûteuse. Du côté photonique, en exploitant la physique de la métasurface périodique, il est possible d'adapter de nouvelles propriétés pour les modes photoniques telles que la vitesse de groupe photonique à la demande et l'ingénierie des pertes,

conduisant ainsi à de nouvelles fonctionnalités pour les dispositifs polaritoniques une fois que le régime de couplage fort de ces photons avec les excitons de la pérovskite est établi.

CHAPITRE 1. INTRODUCTION DES POLARITONS EXCITONIQUES DANS LA PEROVSKITE HALOGENEE

Le chapitre 1 présente d'abord les concepts généraux des excitons dans les semi-conducteurs et le régime de couplage fort entre les excitons et les photons confinés pour former des quasi-particules exciton-polariton. Dans la deuxième partie du chapitre, nous discutons de l'émergence de la perovskite halogénée comme matériau excitonique à température ambiante pour étudier la physique du couplage fort. Nous présentons ensuite les concepts essentiels des résonances photoniques de Bloch dans un réseau sub-longueur d'onde tels que l'ingénierie de la bande interdite et l'état lié dans le continuum (Bound State in the Continuum, BIC). Enfin, nous introduisons l'approche de la métasurface excitonique pour explorer les excitons-polaritons dans une couche de pérovskite structurée.

Du côté des matériaux, des travaux pionniers sur les polaritons excitoniques ont été réalisés avec des puits quantiques à base de GaAs et de CdTe [6]. Bien que ces matériaux, en particulier le GaAs, restent les matériaux excitoniques les plus utilisés pour étudier la physique polaritonique, leur fonctionnement est limité aux températures cryogéniques en raison de la modeste énergie de liaison excitonique de quelques meV [7]. Dans le but de réaliser des dispositifs polaritoniques adaptés à des applications pratiques, la recherche s'est orientée vers les excitons à température ambiante. Dans ce contexte, les perovskites 2D sont considérées comme l'un des candidats les plus attrayants pour la démonstration du couplage fort à température ambiante. Leurs excitons possèdent des énergies de liaison allant jusqu'à des centaines de meV, des forces d'oscillation exceptionnelles et des non-linéarités élevées. En outre, les pérovskites 2D sont traitées en solution, ce qui permet de les modeler en différentes

structures, soit par infiltration dans des réseaux périodiques, soit par impression thermique à l'aide de modèles nanostructurés. En raison de ses excellentes propriétés et de sa facilité de fabrication, nous avons choisi une pérovskite 2D en couches appelée PEPI comme matériau excitonique dans le travail de cette thèse.

Pour le schéma de confinement photonique, la plupart des travaux sont basés sur la microcavité verticale planaire [6,12,27–34, 35] qui peut être considérée comme l'exemple type d'exciton-polaritons. Cependant, l'approche de la microcavité planaire et ses dérivés présentent plusieurs inconvénients : i) l'empilement est très épais et il est très difficile de fabriquer des dispositifs à injection électrique, ii) l'approche multicouche n'est pas compatible avec la technologie CMOS, iii) l'ingénierie des propriétés polaritoniques par microstructuration ne concerne que l'échelle supra-longueur d'onde, ce qui signifie que l'adaptation des propriétés polaritoniques à l'échelle sub-longueur d'onde est pratiquement inexplorée.

Dans notre travail, nous proposons des métasurfaces excitoniques à motifs périodiques comme une nouvelle plateforme pour étudier la physique des excitons-polaritons. Contrairement à la conception traditionnelle de la microcavité, l'approche de la métasurface offre une grande flexibilité pour l'adaptation des propriétés polaritoniques (vitesse de groupe, facteur de qualité des modes localisés, modèle d'émission, etc.) et peut être appliqué à une large gamme de matériaux excitoniques. Le matériau excitonique (ici utilisé PEPI) est directement modelé dans un cristal photonique à l'échelle sub-longueur d'onde d'un réseau de nano-piliers (voir Figure A1). Ainsi, le matériau actif lui-même est l'hôte du confinement photonique. En conséquence, notre approche originale permet d'étudier un régime polaritonique inexploré généré sur la base de comportements collectifs d'éléments actifs sub-longueur d'onde. Nous appelons la plateforme d'un tel ensemble de nano-piliers excitoniques "métasurface excitonique".

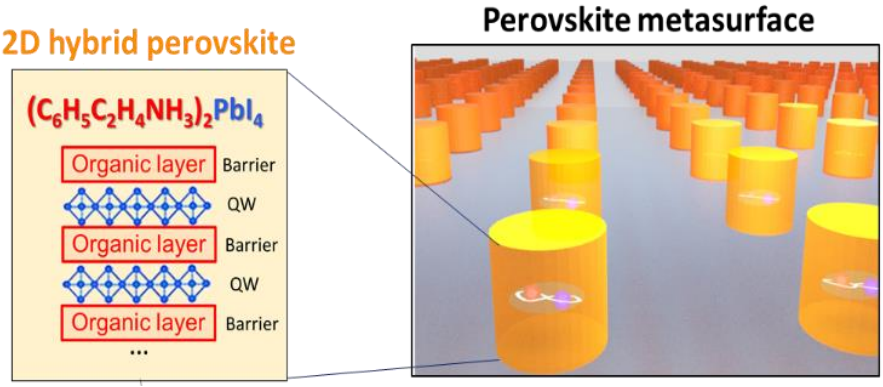

Figure A1. Illustration des métasurfaces excitatrices de pérovskite étudiées dans cette thèse.

CHAPITRE 2. FABRICATION D'UNE MÉTASURFACE DE PÉROVSKITE

Le chapitre 2 présente nos différents procédés de fabrication pour le dépôt de films minces de pérovskite et la structuration de la couche de pérovskite en métasurface. En particulier, deux méthodes de structuration de la pérovskite sont développées : l'infiltration d'une solution de pérovskite dans un substrat pré-modelé, et la structuration directe d'une couche de pérovskite par nanoimpression thermique (Figure A2).

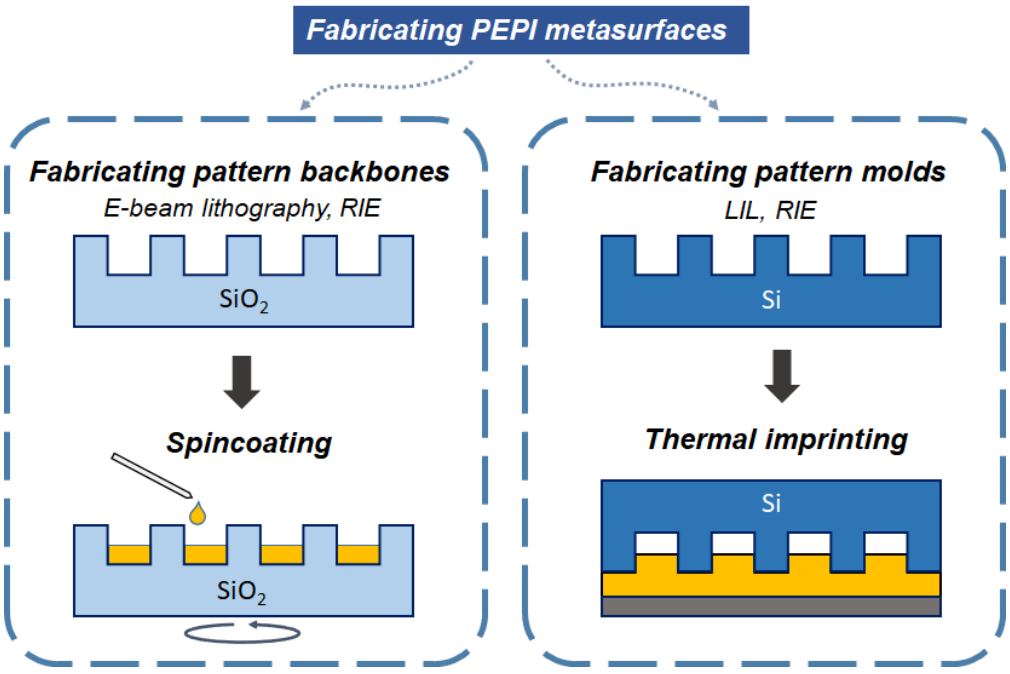

Figure A2. Schémas de fabrication de métasurfaces PEPI par deux méthodes : infiltration et impression thermique.

Nous avons effectué plusieurs caractérisations, notamment la morphologie/qualité de la cristallisation (MEB, XRD), les propriétés optiques (photoluminescence, absorption) et la stabilité (durée de vie), afin de quantifier et d'évaluer les structures fabriquées.

Notre première approche pour structurer le PEPI a été de l'infiltrer à l'intérieur de squelettes pré-structurés via un simple enduction à la tournette (spin-coating). Des caractérisations MEB et optiques ont été réalisées et ont confirmé la formation du réseau de piliers PEPI (Figure A3). Cette approche présente cependant une limitation due au faible contrôle de l'infiltration, ce qui affecte l'homogénéité à petite échelle. Cependant, cette méthode d'infiltration est très flexible, facile à réaliser, et convient à notre objectif d'étudier les dispersions de polaritons de différentes conceptions. Les métasurfaces PEPI fabriquées par la méthode d'infiltration ont été étudiées plus en détail afin de démontrer l'ingénierie de la dispersion des excitons-polaritons. Ces résultats seront discutés dans les chapitres suivants (3 et 4).

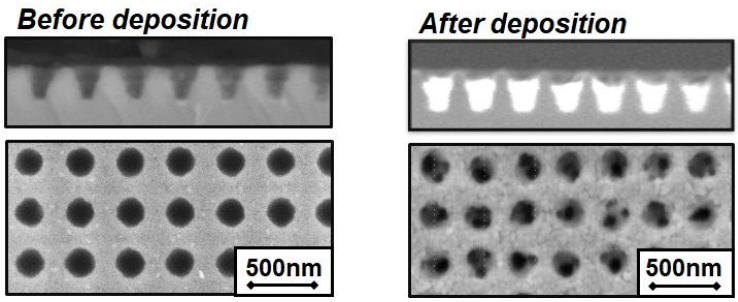

Figure A3. Image MEB et image MEB en coupe de la structure SiO_2 (fabriquée par lithographie interférentielle) avant et après le dépôt PEPI.

Pour améliorer l'homogénéité de la surface, nous avons développé le procédé d'impression thermique pour la fabrication de métasurfaces PEPI. Les propriétés de la métasurface imprimée ont été évaluées par MEB, AFM et caractérisation optique. Des métasurfaces PEPI à réseau 2D ont été fabriquées, présentant des surfaces homogènes sur quelques mm à grande échelle. De telles métasurfaces de haute qualité, à faible coût et de grande surface sont très prometteuses pour la fabrication de dispositifs. Dans cette thèse, des

métasurfaces imprimées PEPI ont été conçues et fabriquées de manière à étudier la propagation balistique d'exciton-polaritons. L'étude de la propagation des excitons-polaritons sera présentée au chapitre 5.

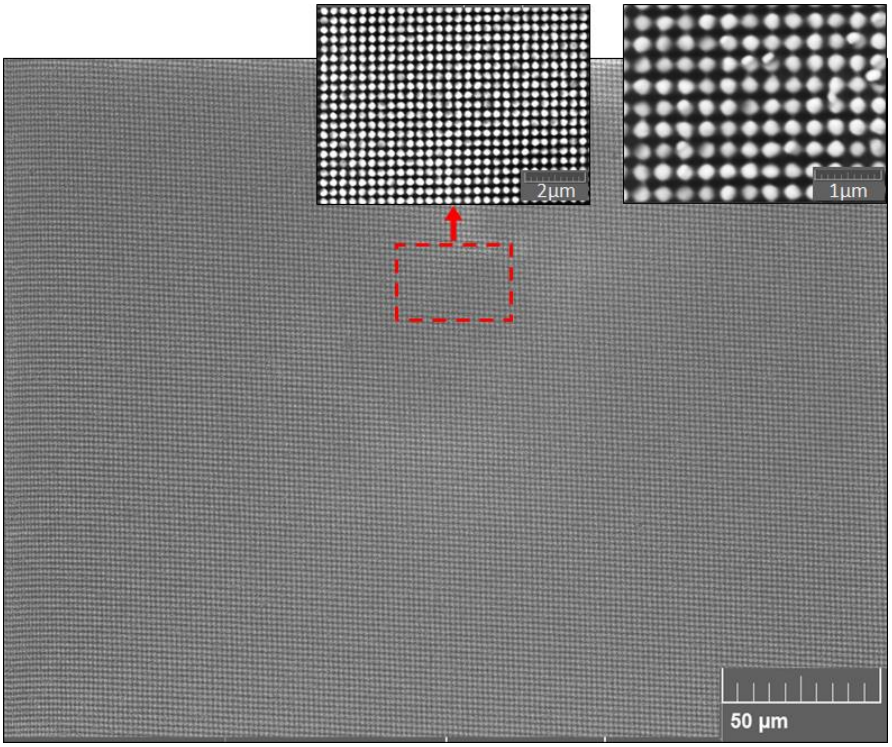

Figure A4. Image MEB de la couche PEPI imprimée. La zone mesurée a une dimension d'environ 300 µm x 200 µm.

CHAPITRE 3. ADAPTATION DE LA DISPERSION DES POLARITONS D'EXICTON AVEC UNE MÉTASURFACE DE PÉROVSKITE

Le chapitre 3 traite de l'ingénierie de la structure de bande des polaritons à température ambiante à l'aide d'une métasurface de pérovskite. En utilisant le concept des résonances de Bloch dans un cristal photonique planaire 2D, nous prédisons et démontrons expérimentalement une adaptation à la demande de la structure de bande énergie-vecteur d'onde des polaritons (c'est-à-dire la partie réelle de la dispersion des polaritons). Comme preuve de concept, le régime de couplage fort à température ambiante dans les métasurfaces à base de pérovskite est observé expérimentalement avec une énergie de séparation de Rabi remarquable d'environ 200 meV. Les résultats des mesures de réflectivité résolue en fonction de l'angle (ARR) et de

photoluminescence résolue en fonction de l'angle (ARPL) montrent que la dispersion des polaritons partage la même forme que celle des modes photoniques non couplés lorsqu'ils sortent de la région d'anticroisement. Cela conduit à des modes polaritoniques qui peuvent être conçus pour obtenir des caractéristiques linéaires, de lumière lente, ou même multi-vallées en ajustant les paramètres du réseau de la métasurface. Tous nos résultats expérimentaux sont en bon accord avec la simulation numérique et le modèle analytique (figure A5).

Des polaritons linéaires ont été démontrés présentant une vitesse de groupe élevée, jusqu'à 126 μm/ps. Ce régime de vitesse élevée est parfaitement adapté à l'étude de la propagation balistique des polaritons pour la transmission d'informations et le déclenchement de signaux entre dispositifs polaritoniques [125]. Nous avons également montré la formation de polaritons aux caractéristiques contraires, les polaritons à lumière lente dont la vitesse de groupe s'approche de zéro à k=0. Un tel régime de lumière lente, présentant une forte densité d'états, serait bien adapté pour étudier les effets non linéaires des polaritons, ainsi que pour déclencher la condensation de Bose-Einstein des polaritons. Enfin, nous avons démontré une dispersion polaritonique rare en forme de W, ayant deux vallées correspondant à la disparition de la vitesse de groupe à $|k_x| \approx 5\ \mu m^{-1}$. Cette dispersion polaritonique à plusieurs vallées pourrait être la brique de base de la « vallée-tronique » à base de polaritons [127,128].

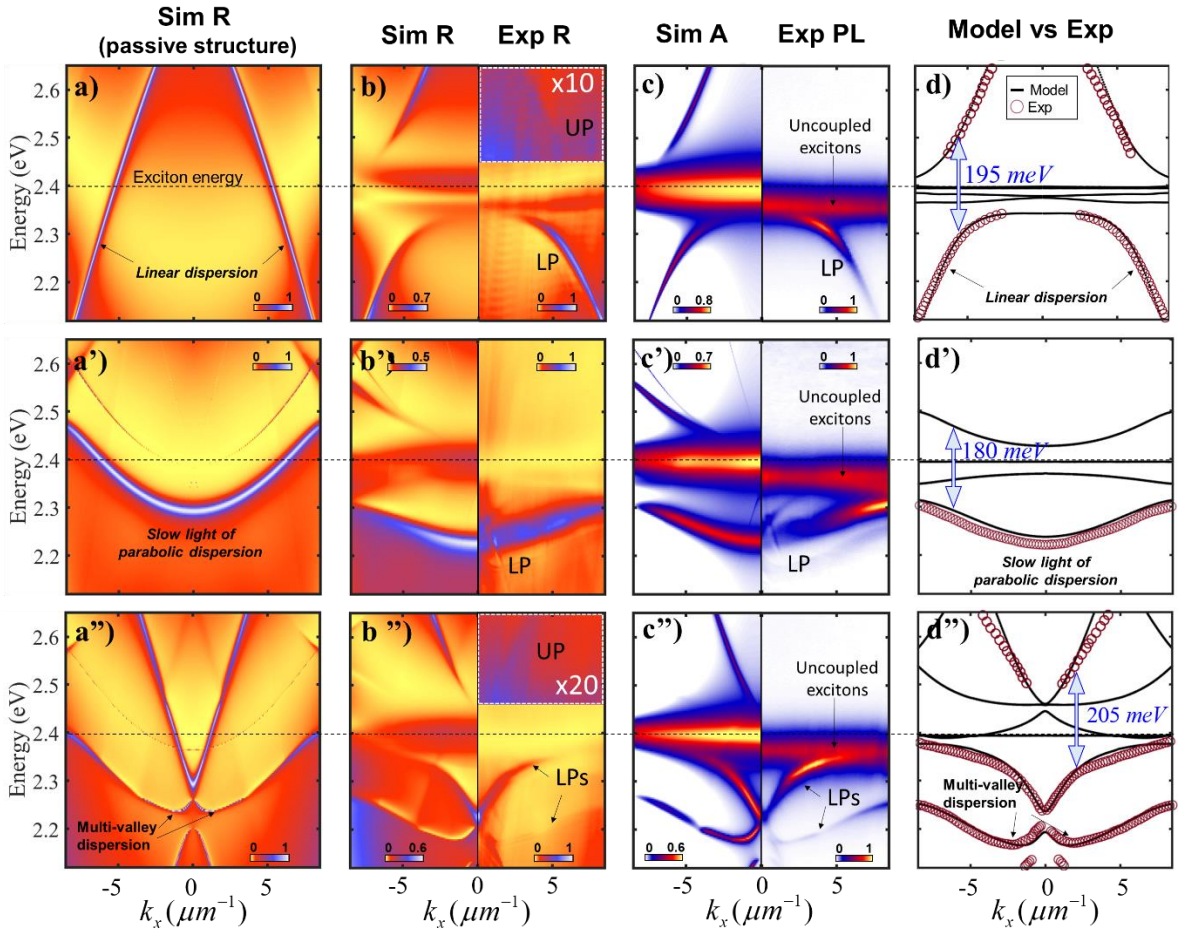

Figure A5. Observation de polaritons présentant : une dispersion linéaire (a-d), une dispersion à lumière lente (a'-d'), une dispersion multi-vallées (a"-d"). (a,a',a") Simulations numériques de l'ARR pour les structures passives. (b,b',b") Résultats expérimentaux (panneau de droite) et simulations numériques (panneau de gauche) des spectres ARR pour les structures actives. (c,c',c") Résultats expérimentaux de la réponse ARPL (panneau de droite) comparés aux simulations numériques de l'absorption à résolution angulaire par RCWA (panneau de gauche) pour les structures actives. (d,d',d") Solution numérique des dispersions de polaritons de cristaux photoniques à partir d'un modèle quantique d'interaction rayonnement-matière, comparée aux résultats expérimentaux extraits des mesures ARR. La ligne pointillée noire représente l'énergie de la résonance excitonique du PEPI.

CHAPITRE 4. ÉTAT LIÉ EXCITON-POLARITON DANS LE CONTINUUM

Les états liés dans le continuum (BIC) sont des états localisés particuliers qui ne peuvent pas rayonner bien qu'ils se trouvent dans un continuum d'ondes qui se propagent. Très récemment, le régime de couplage fort entre les BICs photoniques et les résonances excitoniques a été suggéré théoriquement [132,133,152,153], avec deux démonstrations expérimentales [45,154]. Le résultat d'un tel couplage est la formation de polariton-BICs (pol-BICs) : des excitations hybrides qui sont complètement découplées du continuum radiatif. Cependant, la plupart de ces démonstrations sont réalisées à des températures cryogéniques.

Dans ce chapitre, nous avons conçu des pertes de polariton (c'est-à-dire la partie imaginaire de la dispersion énergie-moment polaritonique) dans la métasurface de pérovskite PEPI afin d'étudier les polariton-BICs à température ambiante.

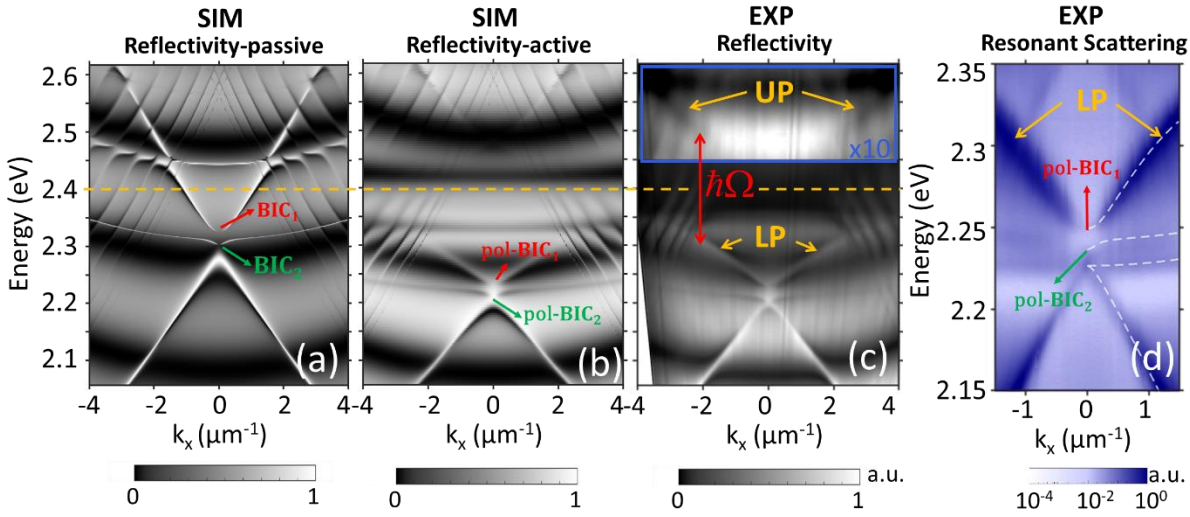

Figure A6. (a) Simulations numériques des spectres ARR calculés pour la structure passive, (b) même simulation pour la structure active ; ici aussi, la ligne pointillée indique la résonance excitonique nue du PEPI. (c) Résultat expérimental de l'ARR de la métasurface PEPI. La séparation de Rabi mesurée ħΩ≈ 200 meV. (d) Résultat expérimental de la diffusion résonante résolue en angle de la métasurface PEPI, zoomée au voisinage des deux pol-BICs. Les lignes pointillées sont des guides pour l'œil pour distinguer les 4 modes polaritoniques.

La formation d'un BIC à polarisation à température ambiante, résultant du régime de couplage fort entre les excitons de la pérovskite et le BIC photonique, est démontrée expérimentalement. Ce pol-BIC, révélé par des mesures de réflectivité, de diffusion résonnante et de photoluminescence, présente un découplage complet du continuum radiatif dans la direction verticale, qui est associé à un rayonnement de champ lointain localement nul dans l'espace des moments (voir Figure A6).

Notre pol-BIC présente une nature quasi-BIC, ayant un facteur de qualité radiatif infini hérité de la composante photonique, mais un facteur non radiatif fini (>1000) hérité de la composante excitonique. La durée de vie radiative infinie du pol-BIC conduit à une augmentation du facteur de qualité total.

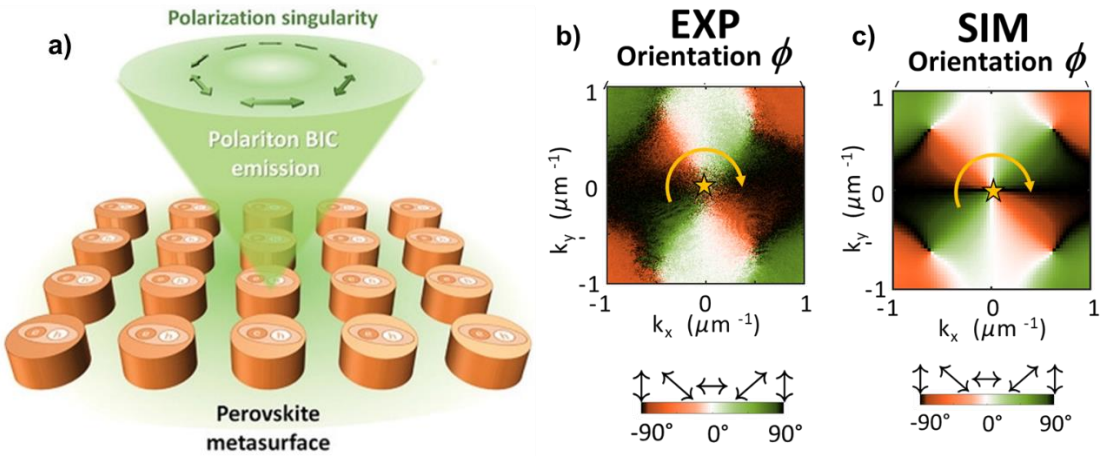

Figure A7. (a) Schéma du pol-BIC dans une métasurface de pérovskite. (b) Résultat expérimental de l'orientation de polarisation φ correspondant au pol-BIC. (c) Simulation de l'orientation de polarisation φ correspondant au pol-BIC.

Enfin, nous avons étudié la nature topologique des pol-BICs. Il s'agit de la première observation de la charge topologique des BICs polaritons. Il est intéressant de noter que cet état polaritonique particulier hérite pleinement de la nature topologique d'un BIC photonique et présente un motif de vortex de polarisation dans l'émission en champ lointain. Nos résultats suggèrent que la métasurface excitonique est une plateforme prometteuse pour révéler et

exploiter les effets des polaritons (tels que la non-linéarité, ou l'interaction avec un champ magnétique) avec l'ingénierie des singularités de polarisation. Une application directe de ce travail sera l'élaboration d'un faisceau laser à vortex de polarisation en atteignant le régime de condensation de Bose-Einstein.

CHAPITRE 5. PROPAGATION BALISTIQUE EXCITON-POLARITON DANS UNE MÉTASURFACE DE PÉROVSKITE

L'étude de la propagation des polaritons est la clé du développement de dispositifs de transmission de signaux polaritons à haute vitesse et efficacité. Dans le chapitre 5, nous nous concentrons sur l'étude de la propagation des polaritons dans une grande métasurface homogène de pérovskite obtenue par la technique d'impression thermique.

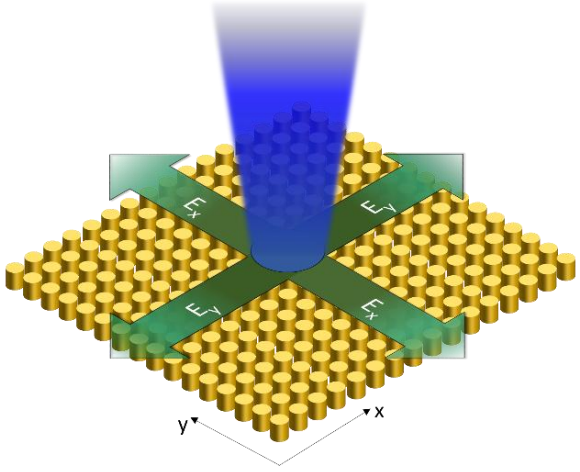

Figure A8. Représentation schématique de la propagation des polaritons à l'énergie choisie. Il consiste en deux flux unidimensionnels le long de x et y de la même vitesse de groupe v_g=30µm/ps mais de polarisations différentes (flèches vertes). Le faisceau bleu indique la lumière d'excitation.

Dans notre métasurface de pérovskite 2D, la propagation du polariton consiste en deux flux unidimensionnels de vitesse de groupe uniforme le long des directions x et y et de polarisations orthogonales (voir la figure A8). Un tel scénario de propagation est démontré expérimentalement en visualisant l'image du champ lointain dans l'espace réel. Nous avons observé que les vecteurs de vitesse des polaritons ne suivent qu'une seule direction (c'est-à-dire x) dans chaque polarisation (c'est-à-dire Ey). Évidemment, en changeant la polarisation entre

Ey et Ex, nous pouvons choisir d'avoir une propagation le long de la direction x ou de la direction y. Sous excitation non résonnante, nous avons détecté un signal PL unidimensionnel de polaritons à 50% de fraction excitonique à plus de 80 µm du point de pompage et la décroissance exponentielle du signal PL affiche une longueur de propagation de 21 µm (Figure A9).

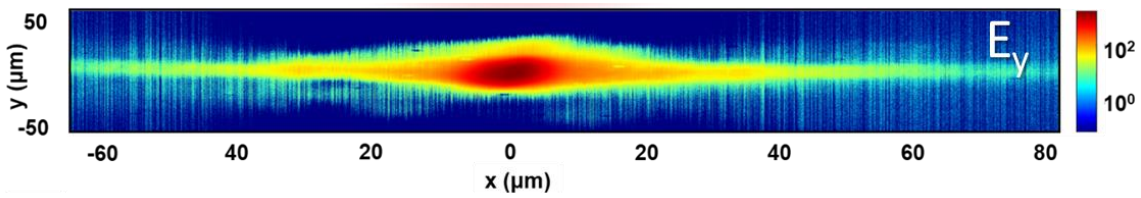

Figure A9. Image de photoluminescence à résolution spatiale des états polaritoniques filtrée à 543nm, avec sélection de la polarisation Ey.

Plus intéressant encore, nous avons étudié et rapporté la nature balistique de la propagation du polariton. La propagation est suivie dans l'espace des vecteurs d'onde pour sonder une éventuelle rétrodiffusion. A 100 µm de l'excitation, seuls les états polaritoniques à vitesse de groupe positive (négative) sont observés.

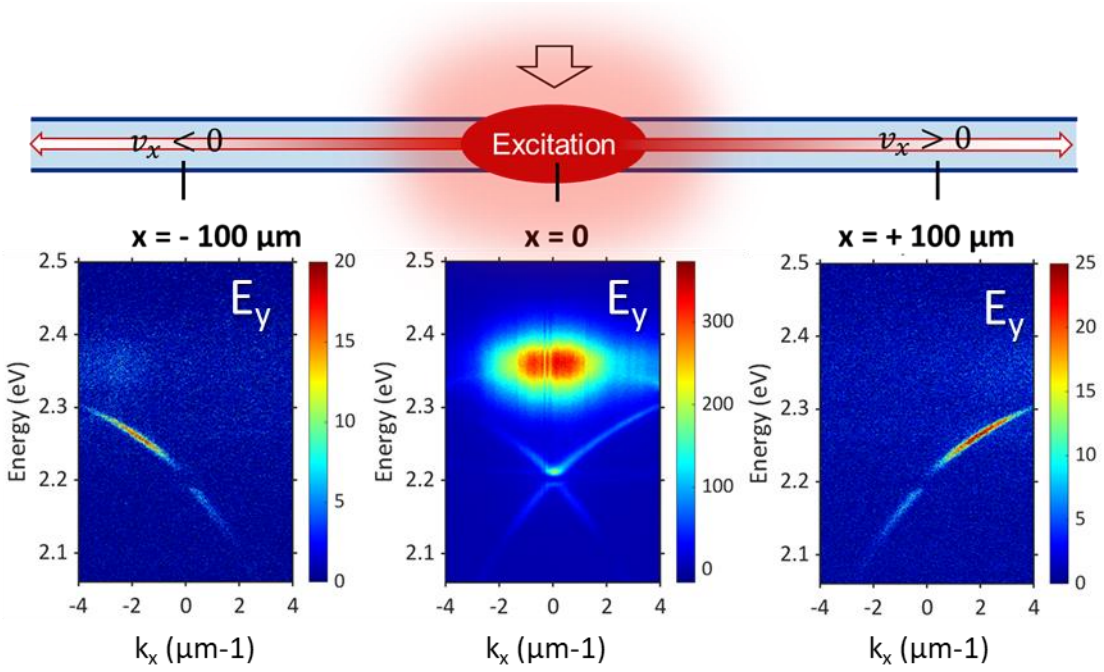

Figure 5.9. Mesures ARPL filtrées spatialement à trois positions différentes le long de l'axe x de la propagation s : x = + 100 µm, x = - 100 µm et x = 0 (spot de pompage)

Cette observation démontre clairement que les polaritons se sont propagés de manière balistique sur les deux côtés de l'axe x sans aucun signe de rétrodiffusion. De manière impressionnante, la propagation est observée même avec une fraction excitonique aussi élevée que 75%. De tels polaritons à fraction excitonique élevée se propageant sur une centaine de micromètres n'ont jamais été rapportés auparavant, surtout à température ambiante. Ce résultat ouvre la voie à la réalisation de dispositifs de communication polaritoniques.